



McKenzie, David J. (2010) *The dynamics of tethers and space-webs*. PhD thesis, University of Glasgow.

<http://theses.gla.ac.uk/1483/>

Copyright and moral rights for this thesis are retained by the author

A copy can be downloaded for personal non-commercial research or study, without prior permission or charge

This thesis cannot be reproduced or quoted extensively from without first obtaining permission in writing from the Author

The content must not be changed in any way or sold commercially in any format or medium without the formal permission of the Author

When referring to this work, full bibliographic details including the author, title, awarding institution and date of the thesis must be given



Ph.D. Thesis:
The Dynamics of Tethers and Space-webs

David J. McKenzie, BEng

Submitted in fulfilment of the requirements for the Degree of Doctor of Philosophy

Departments of Mechanical and Aeronautical Engineering,
Faculty of Engineering,
University of Glasgow, G12 8QQ, Scotland, UK

January 2010

©David McKenzie, 2003-2010

Contents

Abstract	15
Acknowledgements	16
1 Introduction	19
1.1 Overview of thesis	21
2 Literature review	23
2.1 Early pioneers	23
2.2 Tether fundamentals	25
2.2.1 Fundamental tether concepts	26
2.2.2 Non-rotating tethers	26
2.2.3 Momentum exchange	27
2.2.4 Motorized momentum exchange tethers	29
2.2.5 Staging with momentum exchange	30
2.2.6 Deploying and recovery of tethers	31
2.2.7 Capture and rendezvous of tethers	33
2.2.8 WSB trajectories	33
2.3 Tether derived structures	35

2.3.1	Deployed space structures	35
2.3.2	Space-webs	36
3	Tether modelling	38
3.1	Constructing the equations of motion of a system	38
3.1.1	Validating code modules	39
3.2	Centre of mass modelling	40
3.2.1	Mass points & body selection	40
3.2.2	Centre of mass calculations	41
3.2.3	Positions of mass points	43
3.3	Constructing Lagrange's equations	48
3.3.1	Energy modelling	49
3.3.2	Choosing generalised coordinate systems	50
3.4	Non-conservative forces	51
3.5	Rotation systems	52
3.5.1	Rotation summary	53
3.5.2	YZ Rotations	55
3.5.3	ZY Rotations	56
3.5.4	Comparing the equations – position equations	59
3.5.5	Comparing the equations – kinetic energies	59
3.5.6	Comparing the equations – potential energies	60
3.5.7	YZ rotation in inertial axes	61
3.5.8	Singularities in the rotational systems	61
3.5.9	Practical uses of the different equations	62

3.6	Numerical integration techniques	62
4	Dynamics of tethers with inclination	64
4.1	Addition of inclination to tether model	65
4.1.1	5 degree of freedom model	66
4.2	Constructing the equations of motion	67
4.2.1	Rotations in the local coordinate system	68
4.2.2	Lagrange's equations	71
4.2.3	Lagrange's equations – local system	71
4.2.4	Lagrange's equations – global system	75
4.2.5	Non-conservative forces	77
4.3	Analysis of tether on an inclined orbit	80
4.3.0.1	Behaviour of R, θ and ι with time	81
4.3.0.2	Behaviour of α with time	81
4.3.0.3	Behaviour of $\dot{\alpha}$ with time	82
4.3.0.4	Behaviour of α with ι	82
4.3.0.5	Behaviour of $\psi, \dot{\psi}, \ddot{\psi}$	83
4.3.0.6	Behaviour of $\alpha, \dot{\alpha}, \ddot{\alpha}$	83
4.3.0.7	Behaviour of ΔV with time	84
4.3.0.8	Behaviour of tension with time	84
4.3.0.9	Behaviour of stress with time	84
4.3.1	Analysis of tension and stress in tether	85
4.4	Tether release aiming	86
4.4.1	Tether error analysis	88

4.4.2	Lunar capture	90
4.5	A demonstration Lunar mission with a tether launch	91
4.5.1	Spacecraft sizing	91
4.5.2	Analysis	93
4.6	Conclusions	94
4.7	Inclination plots	98
5	Dynamics of tethers with length deployment	108
5.1	Deployment and recovery with the MMET	108
5.2	Addition of length as a generalised coordinate	109
5.3	Constructing the equations of motion	110
5.4	Non-conservative forces	115
5.4.1	Tether braking	116
5.5	Analysis of length deployment of tether	117
5.5.1	Discussion of results for deployment	118
5.6	Refining the equations of motion	120
5.7	Recovery of tethers	123
5.7.1	Recovery profile	124
5.7.2	The equations of motion for recovery	125
5.7.3	Solving the equations of motion for recovery	126
5.8	Deployment and recovery on an elliptical orbit	128
5.9	Centre of mass movement	130
5.10	Conclusions	131
5.11	Figures	132

5.11.1	Linear kinetic energy	143
6	Dynamics of space-webs	144
6.1	Introduction	144
6.2	Modelling methodology	146
6.3	Web meshing	146
6.3.1	Web structure	146
6.3.2	Dividing the web	147
6.3.3	Web divisions	148
6.4	Equations of motion	149
6.4.1	Centre of mass modelling	149
6.4.2	Rotations	150
6.4.3	Position equations	152
6.5	Energy modelling	153
6.5.1	Virtual work terms	154
6.5.2	Simplifying Assumptions	155
6.5.3	Robot Position Modelling	156
6.6	Space-web dynamics	157
6.6.1	Dynamical simulation	157
6.7	Investigating the stability of the space-web	158
6.7.1	Mass of the web	158
6.7.2	Robot mass	159
6.7.3	Web asymmetry	160
6.7.4	Robot crawl velocity	162

6.8	Statistical investigation into stability	162
6.8.1	Masses of the web and satellite	163
6.8.2	Masses of the web and robot	164
6.8.3	Mass of the web and angular velocity	165
6.8.4	Mass of the robot and angular velocity	167
6.9	Conclusions and recommendations	168
6.9.1	Conclusions	168
6.9.2	Recommendations	168
7	Conclusions	169
7.1	Tether rotations	169
7.2	Tethers with inclination	169
7.3	Deployment and recovery of tethers	170
7.4	Space-webs	170
7.5	Further study	171
8	Bibliography	172
	Glossary	183
A	Equations of motion with inclination	184
B	Space-webs – additional graphics	188
B.1	Case 1 – CoM plots of stability while increasing web mass	188
B.2	Case 1 – CoM plots of stability while increasing robot mass	190
B.3	CoM plots of stability while changing robot paths	191

B.4 Case 1 – CoM plots of stability while decreasing robot velocity . . .	192
C Space-webs – additional data	195
D Material strengths	200
E Motor properties	202

List of Figures

1.1	Diagram of the MMET.	20
2.1	Tether length increment ΔL , from [Cosmo and Lorenzini, 1997, p175]	27
3.1	Symmetrical dumbbell tether	41
3.2	Symmetrical dumbbell tether on a circular orbit (solid). After payload release, the facility system path at apogee (dash) and payload at perigee (dots)	42
3.3	Asymmetrical dumbbell in inertial axes	44
3.4	Local coordinate construction	45
3.5	Local coordinate construction after rotation through angle ψ about the facility mass	45
3.6	Local coordinate construction after translation from the facility to the CoM	46
3.7	Local coordinate construction after translation from the CoM to the inertial coordinate system	46
3.8	Local coordinate construction after rotation through θ about the inertial coordinate system	47

3.9	Rotation sequence for YZ rotation: Rotating α about Y-axis then ψ about Z-axis. α is shown as a negative rotation here for ease of visualisation.	57
3.10	Rotation sequence for ZY rotation.. Rotating ψ about Z-axis then α about Y-axis. α is shown as a negative rotation here for ease of visualisation.	58
4.1	Ephemeris of Lunar orbital inclination [JPL, 2008]	65
4.2	Rotation sequence for YZ rotation with inclination. α is shown as a negative rotation here for ease of visualisation.	69
4.3	Rotation sequence for YZ rotation with inclination. α and ι are shown as negative rotations here for ease of visualisation.	70
4.4	Eclipse checking function (not to scale)	79
4.5	Sample plot of the Eclipse function in Mathematica	79
4.6	Diagram showing an example of the WSB trajectory, from ESA Bulletin 103: [Biesbroek and Janin, 2000]	87
4.7	Change in apogee of the payload after release from the tether system after one half of an orbit compared to small changes of system parameters	95
4.8	Change in apogee and inclination of the payload after release from the tether system after one half of an orbit compared to small changes of system parameters	96
4.9	The orbital debris environment from LEO to GEO, from [Wikipedia, 2008]	97
4.10	Plots of R , θ and ι vs. time for the five cases.	99
4.11	Plots of α vs. time for the five cases.	100

4.12	Plots of $\dot{\alpha}$ vs. time for the five cases.	101
4.13	Plots of α vs. ι for the five cases.	102
4.14	Phase plots of ψ for the five cases.	103
4.15	Phase plots of α for the five cases.	104
4.16	Plots of ΔV vs. time for the five cases.	105
4.17	Plots of Tension vs. time for the five cases.	106
4.18	Plots of Stress vs. time for the five cases.	107
5.1	Discretised tether diagram with $n = 5$ mass points	112
5.2	Initial MMET Spin-up	132
5.3	Initial MMET Spin-up	133
5.4	Initial MMET Spin-up	133
5.5	Initial MMET Spin-up, discretized tether mass model	134
5.6	Initial MMET Spin-up, discretized tether mass model	135
5.7	Initial MMET Spin-up, discretized tether mass model	136
5.8	MMET reel in, first phase	136
5.9	MMET reel in, first phase	137
5.10	MMET reel in, first phase	138
5.11	MMET reel in, second phase	138
5.12	MMET reel in, second phase	139
5.13	MMET reel in, second phase	140
5.14	MMET deployment with elliptical orbit	140
5.15	MMET recovery with elliptical orbit	141
5.16	MMET deployment, centre of mass movements	141

5.17	MMET recovery, centre of mass movements	142
5.18	MMET recovery, position and acceleration of centre of mass	142
6.1	Concept rendering of the space-web with spiderbots on the surface. .	145
6.2	0 divisions	148
6.3	1 division	148
6.4	2 divisions	148
6.5	3 sub-spans – 0 divs	148
6.6	3 sub-spans – 1 div	148
6.7	3 sub-spans – 2 divs	148
6.8	4 sub-spans – 1 div	148
6.9	5 sub-spans – 2 divs	148
6.10	6 sub-spans – 3 divs	148
6.11	Simplified space-web layout with s sub-spans	149
6.12	Midpoint location	150
6.13	Space-web diagram with 3 sub-spans shown in inertial space. Note: the local axes are in the Y-Z plane.	152
6.14	Contours of CoM movement while varying web and satellite mass . .	164
6.15	Contours of CoM movement while varying web and robot mass . . .	165
6.16	Contours of CoM movement while varying web mass and $\frac{\partial\psi}{\partial t}$. . .	166
6.17	Contours of CoM movement while varying robot mass and $\frac{\partial\psi}{\partial t}$. . .	167
B.1	$mWeb = 27\text{ kg}$	188
B.2	$mWeb = 33.75\text{ kg}$	188
B.3	$mWeb = 37.8\text{ kg}$	189

B.4	$mWeb = 40.5\text{ kg}$	189
B.5	$mWeb = 44.82\text{ kg}$	189
B.6	$mWeb = 47.25\text{ kg}$	189
B.7	$mWeb = 54\text{ kg}$	189
B.8	$mWeb = 67.5\text{ kg}$	189
B.9	$Mrobot = 1\text{ kg}$	190
B.10	$Mrobot = 10\text{ kg}$	190
B.11	$Mrobot = 15\text{ kg}$	190
B.12	$Mrobot = 16\text{ kg}$	190
B.13	$Mrobot = 20\text{ kg}$	190
B.14	$Mrobot = 100\text{ kg}$	190
B.15	Case 1	191
B.16	Case 2	191
B.17	Case 3	191
B.18	Case 4	191
B.19	Case 5	191
B.20	Case 6	191
B.21	$V_{robot} = 10.0\text{ m/s}$	192
B.22	$V_{robot} = 2.0\text{ m/s}$	192
B.23	$V_{robot} = 1.0\text{ m/s}$	192
B.24	$V_{robot} = 0.2\text{ m/s}$	192
B.25	$V_{robot} = 0.1\text{ m/s}$	192
B.26	Case 1 – 3 robots moving symmetrically round the web perimeter	193
B.27	Case 6 – 1 robot moving asymmetrically along first sub-span	194

List of Tables

3.1 Order of rotations in 3D and 2D	55
4.1 Reference table with figure and corresponding rotation	68
4.2 Initial conditions for the inclination numerical solutions.	80
4.3 Initial conditions for the inclination numerical solutions.	98
C.1 Influence of web mass on maximum CoM	196
C.2 Influence of symmetrical robot movement on maximum CoM	196
C.3 Influence of simulation time (effectively robot speed across web) on maximum CoM	196
C.4 Influence of robot mass on maximum CoM	197
C.5 Statistical investigation into stability	198
C.6 Results of the statistical investigation into stability	199
D.1 Properties of selected materials	201
E.1 Properties of GE Motor 5BC49JB1115	202

Abstract

The thesis ‘The dynamics of tethers and space-webs’ investigates the motion of the Motorized Momentum Exchange Tether (MMET) on an inclined orbit, and while deploying and retracting symmetric payloads. The MMET system is used as a basis for examining the stability of space-webs using a triangular structure of tethers while rotating. The motion of small robots is introduced as they move on the space-web, and their motions are found to influence the behaviour of the structure. Several methods of limiting the destabilising influences of the robots are considered, and are found to stabilise the web in most circumstances.

A structured method for describing the rotations of a tether system is outlined, and different rotational systems are compared. This lays the foundation for the further chapters examining MMET dynamics on an inclined orbit and while deploying and recovering the payloads. Lagrange’s equations are generated for the three cases, and are solved using standard numerical integration techniques. To emphasise the practical uses of the MMET system, several missions are analysed by using the system as a re-usable launcher for micro-satellite payloads.

Acknowledgements

I would like to thank the EPSRC for providing a doctoral training grant, enabling the research for this thesis.

I would like to thank the staff at the University of Glasgow for their thoughts and discussions. In particular, Dr Max Vasile for his sharp insights, Dr David Forehand for discussions on many interesting problems and Dr Donald Ballance and Dr Ian Watson for an introduction into teaching. Needless to say, I am also thankful for the hard work of all the administrative staff, in particular Marilyn Dunlop and Jane Livingston.

I would like to thank Prof. Matthew Cartmell for the chance to study such an interesting problem, for his kindness and patience, for his supervision, and for enthusing me with the joys of research.

I would like to thank Colin McInnes for encouraging me to study space systems engineering. The love of space research, fostered under his guidance, played a big part in my decision to undertake a Ph.D..

I would like to thank Chris Draper for the long and interesting conversations we had while sharing an office, and for his enthusiasm in general.

I would like to thank the staff at ESA ACT for the opportunity to study space-web dynamics.

I would like to thank my friends at pausegaming.com, for the camaraderie.

I would like to thank my families for their support. My dad and mum for encour-

aging my talents in mathematics, engineering and LEGO from a very early age right through to the final chapter of this thesis.

I would like to thank my very good friends: Raj, Aaron, Ailsa, Dougie, George, Rhys, and of course, Pob. Our small party seems to have gained a few members and lost a few, but we seem to have weathered the Storm: good friends are as valuable as gold.

I would like to thank Joanna, for her kindness and encouragement, for her love and support, and for a thousand things too big and small to mention.

Declaration of Authorship

The author hereby declares that this thesis is a result of the work carried out in the Department of Mechanical Engineering at the University of Glasgow during the period between October 2003 and January 2010. This thesis is an original contribution by the author unless otherwise indicated.

David McKenzie

January 2010

Chapter 1

Introduction

The field of space research is perhaps unique, in that many novel, different and interesting concepts are commonly developed from a seed of an idea to a satellite in a relatively short space of time. Additionally, mankind has been active in space for a very short time, but has made astounding progresses in understanding in both technical and social fields as a direct result of this.

The cost of these endeavours has been equally astounding, with many nations contributing significant fractions of their GDP towards developing and maintaining a space presence. Equally, all nations with a space presence continually re-assess their capability – politicians want developments faster, accountants want everything done cheaper, scientists want to do better – as a direct result, novel ideas can flourish.

The Motorized Momentum Exchange Tether (MMET) is one of these ideas, with the potential to provide cheaper on-orbit launch costs and a lighter mass when compared to conventional rocket technologies.

A diagram of the MMET is shown in Figure 1.1. A payload mass is connected to a large central facility mass with a high strength tether. A symmetrical mass is attached to the opposite side of the facility and these two tethers and payloads

form the payload arm. A further two tethers are joined to the facility to increase the inertia of facility, these are called the stator arm, and are similar in design to the payload arm.

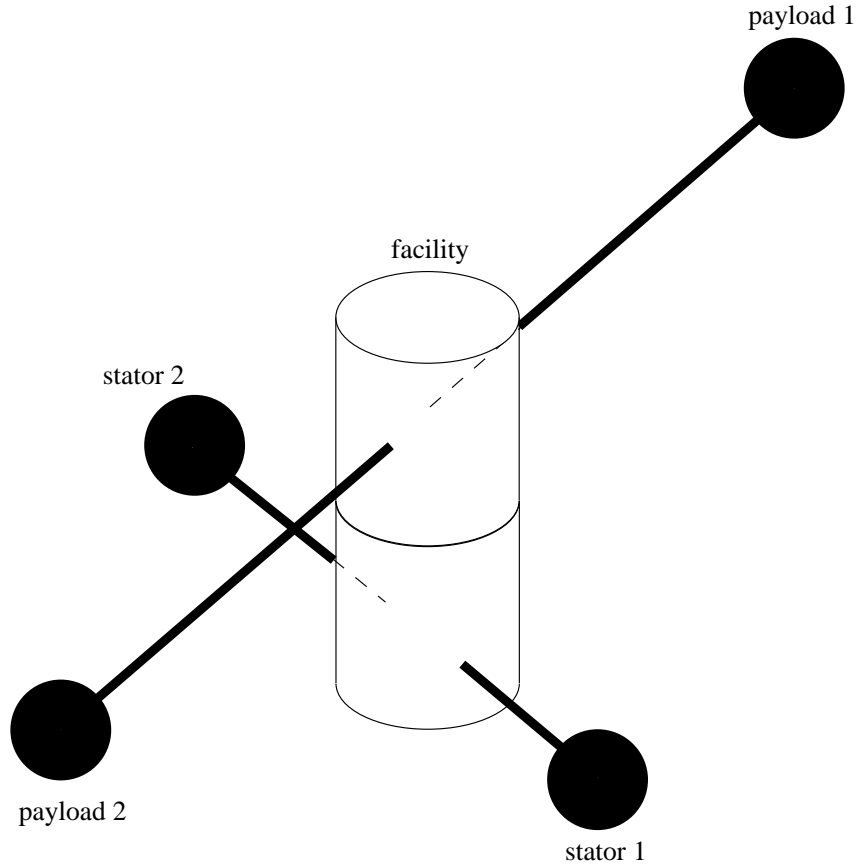


Figure 1.1: Diagram of the MMET.

As with all alternative ideas, the MMET is best suited to a particular mission profile. With the MMET, its strongest advantage is that it is reusable, and may be employed to launch satellites and payloads as long as the tether is intact.

Unfortunately, the MMET does have drawbacks, the four tethers are susceptible to severing from orbital debris, a symmetrical release strategy is required for each payload release and the risk of interference between the payload and stator arms is high. Additionally, the maximum orbital velocity the payload can achieve is limited by the strength of the tethers.

With these in mind, a large body of research into the performance of the MMET, momentum exchange tethers, dumbbell tethers, and tethers in general has revealed

that there are definite advantages in employing these as a tool to enhance or enable many satellite missions. As with all tools, space- or Earth-based alike, it is imperative to use the right tool for the right job.

The research into momentum exchange tethers has been focussed on constructing mathematical models and analysing these models to determine the performance and stability, to avoid any potential weaknesses and to gain a better insight into the fundamental properties of the tether systems. Hardware testing is employed wherever practical (and funds allow!) to validate these models.

Several techniques are available to build these mathematical models. These include Newtonian based techniques, using forces and accelerations, and energy based techniques using Lagrangian formulations.

This thesis will develop a mathematical model of the MMET using a Lagrangian based approach to further analyse the performance of the system in two key areas: on an inclined orbit, and while deploying and recovering the tether.

A new structure – the space-web – is proposed and analysed, composed of a net overlaid on a backbone of a rotating tether system. This can be employed as a base on which to build large space structures such as solar sails and interferometers.

1.1 Overview of thesis

Chapter 2 critically reviews the current literature and gives an overview of the wide range of tether systems.

Chapter 3 introduces the rotational methods that underpin the rotational tether system and rotational systems are examined and compared. A method of constructing Lagrange's equations for a rotating tether is outlined and the tether system is mathematically constructed from its individual components.

Chapter 4 contains an analysis of the MMET dynamics on an inclined orbit, with

in-plane and out-of-plane motions. A demonstration of the tether’s capabilities is shown with an exemplar mission using a Weak Stability Boundary (WSB) trajectory from Medium Earth Orbit (MEO) to the Moon.

Chapter 5 studies the MMET while deploying and recovering the payload and tethers. A mathematical model of the MMET system undergoing deployment is derived, and the stability of the system is assessed using the movement of the centre of mass.

Chapter 6 uses the fundamental tether models to construct a space-web – a structure in space that may be used as a platform to assemble and deploy large space structures.

Chapter 2

Literature review

The field of tether research is broad, and spans many branches of engineering, physics and mathematics. Tethers may be broadly split into three categories: momentum exchange tethers, electrodynamic tethers and structures built using tethers. The notable events in tether history will be critically evaluated.

While this is not an exhaustive review of tethers, as provided in [Cartmell and McKenzie, 2008] or [Cosmo and Lorenzini, 1997], it is intended to cover critically the pertinent topics relevant to this thesis.

2.1 Early pioneers

In 1895, the father of astronautics, Konstantin Eduardovich Tsiolkovsky visited the World's Fair in Paris. Seeing the Eiffel Tower, he imagined a vast structure stretching from the tower to a celestial castle in geostationary orbit above the Earth. From this idea of a tower, fundamentally a compressive structure described in [Tsiolkovski, 1959], the idea of a space elevator was born. Yuri Artsutanov, Tsiolkovsky's student, discussed lowering a structure *from* orbit *to* the ground in [Artsutanov, 1960].

Unfortunately, the good work in the USSR was not immediately available in the West, and it was a number of years before the idea of large-scale tethers and space elevators was published in English. A brief, but informative, article published by [Isaacs et al., 1966] appeared in *Science*, and provided the impetus for academics in the UK and the Americas to study this new idea.

In one of the first articles in *Acta Astronautica*, [Pearson, 1975] identifies the main problems (materials limits, vibrational modes and stability), and solves a great many of them from first principles¹, introducing tapered tethers and taper ratios. Much of the terminology still used derives from that source, for example, characteristic height of materials².

Hans Moravec metaphorically severs the link between the space elevator and the Earth, postulating the tether as a momentum exchange device in [Moravec, 1977], calling it the Skyhook³. This giant spoke rotates, touching down once and interfacing with the surface periodically. He identifies Mars as an ideal candidate for the Skyhook, and provides a good grounding for the specific materials and optimal layouts that are expanded in further research.

Several works of fiction have been inspired by these early pioneers, including Clarke's 'The Fountains of Paradise'. [Clarke, 1979] brings a social aspect to the space elevator research that is often overlooked, and is worth mentioning as the source in which many young researchers first discover the field. Indeed, Clarke remarked in his final interview, see [Das, 2008], that the space elevator will be built 'about 10 years after everyone stops laughing'!

¹On the state-of-the-art analogue computer in 1975, out-powered by several orders of magnitude by today's mobile phones!

²Pearson defines the characteristic height as 'the height to which a constant-diameter tower of the material could be built in a uniform one-g field without exceeding the stress limit of the material at the base'.

³Moravec acknowledges in that paper that the Skyhook idea originated with John McCarthy of Stanford.

2.2 Tether fundamentals

The foundation textbook, ‘Dynamics of Space Tether Systems’ by Beletsky and Levin [Beletsky and Levin, 1993], rigorously introduces the dynamics of tethers, in a progressive and pragmatic manner.

The book discusses the fundamental topics in tether research, such as material density, strength, and orbital location, at a level accessible for a newcomer to tethers. The book then develops equations of motion for a massless and massive flexible tether with variations, covering perturbations and other environmental effects. The dynamics are examined in terms of stability and oscillatory behaviour, based on a Newtonian derivation. ElectroDynamic (ED) tethers, libration and rotation, deployment and retrieval, and Lunar anchored and satellite ring systems serve to complete the coverage of the book. A very useful set of references is also provided, up to the publication year of 1993.

A chapter of the textbook by McInnes and Cartmell [McInnes and Cartmell, 2006] on the dynamics of propellantless propulsion systems covers both solar sails and tethers, each sharing the common goal of overcoming the constraints of using a reaction mass. This reviews missions involving tethers to date, then moves on to summarise the performance expectations of hanging, librating, and spinning tethers, setting them in the context of results extant in the literature.

Carroll’s paper (see [Carroll, 1986]) gives an excellent background to the many different types of tether mission proposed and flown, including the Gemini 12 mission that pioneered the technique of gravity gradient stabilisation with the Agena vehicle. This paper outlines the various roles of tethers, from the space elevator, librating tethers, rotating tethers and momentum exchange tethers.

2.2.1 Fundamental tether concepts

There are a few fundamental concepts that limit the tether, its performance and the missions it may usefully provide.

Rotating tethers (when compared to gravity gradient stabilised tethers) are a logical progression, and extend the usefulness of the tether system. Tether oscillations and other nonlinear dynamics cause concern, and the ever-present possibility of severing the tether due to space debris is only going to worsen with better access to space. Spinning the tether up to rotational speed is a notable problem; in the vacuum of space, there is nothing to provide a base to rotate *against*.

A tether differs from a rocket engine, a mass-based propulsion technique, in that mass is not ejected. This enables tethers to sever the link between payload and fuel. However tethers suffer from a few notable drawbacks: the tether line is vulnerable to debris damage, tethers are limited by their fundamental material properties, and rotating tethers must maximise their velocity increment.

Tethers can broadly be split into two categories: the rotating and non-rotating tether. The rotating tether (see Section 2.2.3) is primarily concerned with imparting a large velocity increment. The non-rotating tether has a variety of uses, with large sections of the literature devoted to control and stabilisation of the tether, as is covered in the next section.

2.2.2 Non-rotating tethers

Tethers may provide stabilisation, control or damping to a structure or constellation in space. Active stabilisation of the tether is usefully demonstrated by ED tethers in a highly readable report, [Hoyt, 2002]. Pendulum librations, transverse wave oscillations, and skip-rope modes are all investigated and control laws proposed in the form of feedback algorithms.

As Figure 2.1 (taken from [Cosmo and Lorenzini, 1997, p175]) illustrates, the rotating tether provides a large advantage over the non-rotating tether in terms of the velocity increment to the payload. A frequently cited result is that the apogee gains $7L$ in height from a hanging tether of length L , less than $14L$ from a swinging tether and more than $14L$ from a rotating tether.

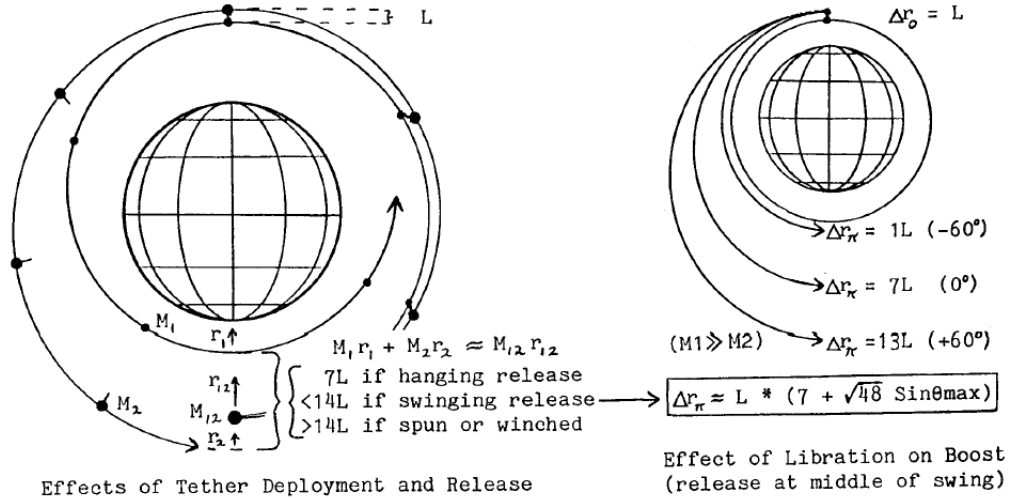


Figure 2.1: Tether length increment ΔL , from [Cosmo and Lorenzini, 1997, p175]

2.2.3 Momentum exchange

Momentum exchange is, in general, the main method in which a tether can impart a useful velocity increment to the payload.

Dumbbell tethers are essentially a coupled pendulum system, and have been well covered in the literature in the past, (e.g. with Hugen's clocks, see [Bennett et al., 2002]). More recently, [Xu et al., 2005] finds that the harmonically excited parametric pendulum can be simplified to the Mathieu equation, opening up this area to a new branch of analysis.

Cartmell investigates parametric excitation of the MMET system, finding that the motor torque may be minimised while guaranteeing a monotonic spin-up of the system. This is achieved by a harmonic modulation of a portion of the payload masses, and by manipulation of the radius of gyration of the additional lumped

masses. Alternatively, given a constant motor torque, the response of the tether may be actively chosen by selecting a bifurcation path.

Misra and Modi, in [Misra and Modi, 1992], provide an excellent Lagrangian formulation for the three-dimensional motion of n -body tethered systems using a multiple-pendulum model as the basis for the equations. The equations of motion are valid for large motion and variable lengths, however, the tethers are massless and straight. This links the n -body pendulum equations and tethered bodies, and provides an excellent template for rigid body motion with many linked tethers.

Moravec published the idea of the momentum exchange device in [Moravec, 1977], defining the Lunavator⁴ as a momentum exchange device that touches the surface of the moon and picks up, or drops, a payload.

The deployment characteristics of a tether system are investigated in [Modi and Misra, 1979], with a thorough and in-depth discussion on the derivation of Lagrange's equations of motion for a rotating tether with vibrations. The equations of motion for a three-mass system (two end masses and a massive⁵ tether) are identified as coupled and nonlinear. They study the tether close to the atmosphere, and conclude that the out-of-plane motion decays provided the tether is outside Earth's atmosphere.

Modi and Misra continue their academic partnership, and report on controlling the tether in [Modi et al., 1982], control of tethers used in Space Shuttle-based tethers in [Modi et al., 1992] and tethered elevators in [Modi et al., 1993].

Perhaps with the Shuttle retiring in 2010, the Shuttle will be proposed less frequently as an end-mass for the tether, as in [Kyroudis and Conway, 1988] and [Pascal et al., 1999], instead replaced by the upper stage of an Ares rocket. It is interesting to note that Pascal mentions ‘crawlers’ – moving payloads along the tether as

⁴The Lunavator works best on planetary bodies with no atmosphere, where there is no atmosphere to drag against the tether, and on Mars, where the combination of favourable rotation and relatively weak gravity suits the system. However, the name Martivator is clumsy, and has not caught on.

⁵Massive in the sense of a body with a non-zero mass, not massive as in very large.

an alternative to full deployment. A variation of this moving mass system used to control tethers may also be used to control space-webs, as will be discussed later in this thesis.

2.2.4 Motorized momentum exchange tethers

To rotate the tether to launch velocity, it is necessary to provide a means of rotation. On Earth, this is provided *by* the Earth, however on orbit, one must bring the counter-rotation device along with the launch device – in a similar manner to a helicopter’s tail boom.

[Eiden and Cartmell, 2003] briefly summarises the possible role of a European roadmap for non-conductive tethers, nominally based on momentum exchange, and also for conductive tethers in which electrodynamics, alongside momentum exchange, provide propulsion. In the case of the former class small and large payload de-orbit are seen as near term goals, with free flying tethered platforms and artificial gravity systems in the mid-term, followed eventually by spinning tethers providing interplanetary propulsion. Gravity gradient stabilisation is an important underpinning phenomenon when considering spacecraft stability, and this is particularly the case for long momentum exchange tethers. In [Cartmell et al., 2003], dumbbell models are considered for momentum exchange tethers, and offshoots and developments of this work have shown conclusively that hanging, librating, and spinning tether motions are intimately connected to this fundamental phenomenon, as reported in [Ziegler and Cartmell, 2001]. Ziegler shows in [Ziegler and Cartmell, 2001] that the rotating MMET outperforms a librating tether by two orders of magnitude in boosting the apogee of a payload.

An in-depth treatment of the rigid body dynamics of tethers in space is given by [Ziegler, 2003]. In this work the dumbbell tether is modelled at various levels of accuracy, and approximate analytical solutions are obtained by means of the method

of multiple scales⁶ for periodic solutions. Comprehensive dynamical systems analyses are summarised for different configurations and models, and global stability criteria for a rigid body dumbbell tether, in both passive and motorised forms, are defined and investigated.

The method of multiple scales is described further in [Cartmell et al., 2003] in a review article with several examples. With respect to tethers, the method of derivation is covered in great depth. An analytical solution to the MMET system is derived using the multiple scales method in [Cartmell et al., 2006], where the equations describe a forced and parametrically excited Duffing oscillator.

Sorensen has authored two interesting papers ([Sorensen, 2003] and [Sorensen, 2001]) detailing a method of using Momentum eXchange/Electrodynamic Reboost (MXER) tethers powered by ED tethers to provide interplanetary travel through hyperbolic escape from Earth's gravity. The second details a boost station that sequentially raises the payload's orbit through repeated rendezvous and momentum exchanges. Of additional note are the appendices detailing analysis techniques and mathematical derivations that can be used in tether facility design.

With any rotating system, the possibility of rotational instability arises. [Valverde and van der Heijden, 2008] find that a magnetic buckling of a welded rod is found to be described by a surprisingly degenerate bifurcation. This has serious implications for using ED tethers as well as static (conducting and non-conducting) deployed tethers for rotational launch systems.

[van der Heijden, 1995] covers the effects of bearing clearance driving a nonlinearly coupled driven oscillator in rotordynamics, with close parallels to the MMET system. Partial mode-locking then leads to quasi-periodic motion of the rotors, and perturbations of the system lead to more complicated motions.

⁶The multiple scales method was popularised in [Nayfeh and Mook, 1979].

2.2.5 Staging with momentum exchange

As the fundamental material limits of tethers limit the useful ΔV that may be imparted, novel techniques such as staging tethers are explored.

A short and digestible article by Forward and Hoyt in Scientific American (see [Forward and Hoyt, 1999]) first showed the ingenious concept behind the use of multiple, staged tethers to increase velocity without the necessity of extreme design, for Earth-Moon payload transfer. [Forward, 1991] continues this work by pairing the Lunavator with a Low Earth Orbit (LEO) tether.

The concept of staging is expanded further in [McInnes and Cartmell, 2006] and [Cartmell et al., 2004].

Following up from the ground-tests of a momentum exchange tether performed on ice, [Cartmell et al., 2003] takes this a stage further, and rigorously examines the release and de-spin of payloads.

Large-scale electrodynamic and momentum transfer between planets was studied in the NASA MXER program, by Forward, Hoyt, Sorensen and others. Initial concept design work in [Sorensen, 2001] outlined a massive tether system to send 20 – 80 tonnes to Lunar or Mars orbit, with a tether length of up to 100 km. Sorensen finds that hyperbolic injection is possible in [Sorensen, 2003], and this opens up the MXER system to send payloads to Mars. It must be stated that the necessary velocity to launch a payload to Mars is not attainable with current materials⁷, to do so would require a significant increase in the specific strength of the tether.

2.2.6 Deploying and recovery of tethers

Further work on using tether based transfers was reported by [Lorenzini et al., 2000] in their landmark paper in which staged tethers in resonant orbits are proposed

⁷The ΔV for LEO to LMO (Low Mars Orbit) is approximately 6.1 km/s and the maximum characteristic velocity of a single strand tether is approximately 2.7 km/s. See Appendix D, Table D.1 for current material properties.

as being more mass efficient than single tether systems⁸. Lorenzini et al. briefly refer to tether orbit raising results cited by [Carroll, 1986] for radial separation as a function of tether length, and conclude that spinning staged tethers could provide an ideal transfer rate of five transfers per year. The transfer rate of a staged system is determined by the periodic realignment of the apsidal lines of the two stages, whereas in the case of a single tether it is dependent on the time required for re-boosting the stage.

Continuing with the theme of propulsion of a small payload tethered to a large mass in the form of a space station or large Shuttle, [Pascal et al., 1999] investigated the laws of deployment and retrieval by means of a three dimensional rigid body model of a dumbbell tether in both circular and elliptical orbits, expanded in [Pascal et al., 2001]. Several laws are proposed and analytical solutions for small planar and non-planar motions of the tether are given, showing that equilibrium tension can be stated as a function of instantaneous tether length and corresponding axial acceleration, for which control laws can be stipulated. It is shown that deployment is generally stable whereas retrieval is not. Various laws are examined for deployments and retrievals, and also for crawler configurations in which the end payload moves out along a pre-deployed tether and how this can mitigate the inherent instability of retrieval.

The next conceptual step to take when considering deployment is to include some form of flexibility within the tether, and an interesting study of this was published by [Danilin et al., 1999], in which the elastic tether model of [No and Cochran Jr., 1995] is used but with different variables and derivation. The objective of this paper was to consider deployment of a completely flexible tether from a rigid rotating space vehicle under the influence of a central gravitational field. The tether is modelled using a Newtonian derivation as a series of discrete masses interconnected by massless elements and with internal viscous damping. The authors make the very

⁸They propose using a facility to payload mass ratio of 1 : 3 using current materials.

important point that tether element forces cannot be compressive, so conditions within the numerical solution algorithm have to be set up to accommodate the consequential folding effects. Two numerical examples are summarised; one for a swinging terrestrial cable with an end mass, which starts from a horizontal initial condition, mainly as a verification of the model in those conditions; and the other for plane motion of a space vehicle deploying a relatively short 3 km tether, with elemental spacing of 100 m . The deployment is linear and conditions are set up to apply smooth braking of the tether to a halt at the end of the deployment.

2.2.7 Capture and rendezvous of tethers

An implicit assumption with tether staging is that the payload will, at some point, have to rendezvous with a second system. [Lorenzini, 2004] provides an in-depth treatment of a spinning tether loop with an extended time opportunity for error-tolerant payload capture within high ΔV propulsion to GTO and Earth escape orbit. The configuration is such that the ends of the loop are furthest away from the centre of mass, where the loop is at its narrowest. The concept is simple in principle. The satellite contains a harpoon which shoots through the loop and hooks onto the loop to capture the satellite. This makes it tolerant of large longitudinal position errors and reasonable lateral errors as well as some out-of-plane error. The capture is soft, and so caters for some velocity mismatch.

[Williams et al., 2003] outlines a ‘momentum-enhanced gravity-assist’ technique to capture a payload on a previously hyperbolic orbit into planetary orbit. This is feasible in theory, however requires accurate control and a large tether deployment rate, which may limit the practical usefulness of the technique.

A subsequent paper, [Williams et al., 2005], systematically describes the problems in payload capture (spatial and temporal matching, post-capture dynamics and failure concerns), and designs a suitable rendezvous and control system involving a

crawler to successfully capture a payload.

2.2.8 WSB trajectories

Perhaps one of the most interesting concepts in trajectory analysis, at least as far as the tether is concerned, is the Weak Stability Boundary (WSB) trajectory proposed by [Belbruno, 1987]. This technique allows the majority of the ΔV for an Earth-Moon mission to be concentrated in the first burn, with a relatively minor capture burn at the end of trajectory.

If this is compared to the ΔV requirement of the Hohmann two-burn technique⁹, it becomes clear that a tether-based launcher system could provide a more efficient route to the Moon. A thoroughly good overview of the WSB method is given in [Ross, 2004, p112], where it is stated that the fuel required is lowered by about 20%. As is common with large research groups, there are many valuable papers on WSB transfers and the Interplanetary Transport Network from the CalTech researchers that are listed in Ross' thesis.

A practical example of the WSB method is explained clearly in [Koon et al., 1999], giving an example of a trajectory similar to the Hiten Lunar probe. The WSB trajectory¹⁰ has since been used to successfully launch NASA's Genesis mission to study the solar wind (see [Lo and Ross, 2001]).

The WSB trajectories are an umbrella for a multitude of possible routes, in contrast to the simplicity of the Hohmann or bi-elliptic trajectories. A useful geometric method of finding such a WSB trajectory is outlined in [Gómez et al., 1993], taking the destination as the Earth-Sun L1 point. Once this point is reached, the pathways are open to a great many places in the Solar system.

⁹Hohmann's seminal book on 'The Attainability of Heavenly Bodies' may be found in its original form [Hohmann, 1925] (in German) or translated to English in [Hohmann, 1960]

¹⁰ The WSB trajectory is hard to visualise and perhaps 2D plots of the spacecraft's path in inertial and rotating space are difficult to extrapolate mentally to 3D space. Thankfully Lo has made videos of the spacecraft path on his website: <http://www.gg.caltech.edu/~mw1/communications/communications2.htm>

A method of using a MMET with a WSB trajectory is outlined in [McKenzie and Cartmell, 2004]. A small satellite MMET system, under 1000 kg , is able to launch a 10 kg micro-satellite from MEO to Lunar capture orbit in around 100 days. This system may be recovered and re-launched every month until the useful life of the satellite is reached. This relies on a very small safety factor of 1.3 in the main tethers, and does not account for the additional stator arm in the MMET, however this shows that the current state of technology is almost ready to sustain an orbital tether launch system.

2.3 Tether derived structures

In the same way that orbital tethers have evolved from the space elevator, space structures may be constructed from tethers.

2.3.1 Deployed space structures

In 1968, Peter Glaser suggested that a solar collector¹¹ could be placed in geostationary orbit [Glaser, 1968]. Operating in high Earth orbit, this would use microwave power transmission to beam solar power to a very large antenna on Earth where it can be used in place of conventional power sources. The advantages to placing the solar collectors in space are the unobstructed view of the Sun, the fact that it is then unaffected by the day/night cycle, weather, or seasons. For efficient operation, the satellite antenna must be between 1 and 1.5 km in diameter and the ground rectenna around 14 km by 10 km , generating between 5 and 10 GW of power. One option of constructing this huge collector is manufacturing the cells on Earth, and constructing them in space with the aid of robots.

An alternative approach to the on-orbit assembly of such a massive structure would be the use of webs, as in [Kaya et al., 2004a] and [Kaya et al., 2004b]. A large generic

¹¹That is, a satellite for collecting solar power.

net-like structure could firstly be deployed in orbit. Once the net is stabilised, robots could be used to crawl over the net towards specified locations and move solar cells into the desired positions. This enables the construction of such a satellite using robot assistance to be faster and cheaper¹².

Other large space structures have been proposed that would make use of a generic reconfigurable platform. In the case of the orbiting stellar interferometer, [DeCou, 1989] showed that planar deformation of a spinning system comprising three collimating telescopes at the corners of an equilateral triangle made up from three interconnecting tethers would be inevitable due to the inertia of the tethers. Clearly inertia-less tethers will not deform centripetally and will, instead, merely stretch into straight lines due to the tension created along their length by the corner masses as the whole system rotates. Perhaps the addition of a control system would make this particular structure a more realisable option.

This directly led to the successful deployment of the Inflatable Antenna Experiment (IAE), and led a tranche of successfully deployed structures in space, including the ESA Cluster mission as detailed in [Andión and Pascual, 2001].

Studies have previously shown that robots may be deployed in this way to reconfigure the net structure [Kaya et al., 2004a], [Nakano et al., 2005]. A international collaboration from the University of Glasgow, KTH Royal Institute of Technology in Sweden and the ESA plans to test the concept on a sounding rocket in 2010, as reported in a [University of Glasgow Press Release, 2009].

2.3.2 Space-webs

If the generic satellite is to be used as an element of infrastructure, it is desirable to start studying the dynamics and deployment of such a structure. A type of

¹²To a degree, the question of whether a method of power generation is ‘better’ is largely a political decision.

satellite, called ‘Furoshiki’¹³ is outlined in [Nakasuka et al., 2001], with an overview of the concept, a simulation of a membrane satellite and an evaluation of the control strategy needed to stabilise such a satellite.

Further work on the deployment of a square membrane is examined in [Tibert and Gärdsback, 2006], where a membrane is attached to four daughter satellites and deployed while the satellite is both free and rotating. It is shown that the free deployment without damping is not possible, however a torque can be applied to the central hub to stabilise the deployment.

Once the membrane is deployed, robots such as reported in [Kaya et al., 2004a] may be tasked to assemble or reconfigure the structure.

A multi-tethered structure containing n masses is investigated in [Pizarro-Chong and Misra, 2008], for an open hub, closed hub (wheel) and double pyramid formations. A system of Lagrange’s equations of motion is constructed and the stability of the three configurations were tested in a variety of configurations – parallel and perpendicular to the orbital plane and with and without an initial spin-rate. The dual-pyramid formation was found to be the stable in most tests, with all configurations benefiting from a rotating platform.

A similar analysis in [Wong and Misra, 2008], involving a multi-tethered structure near the Sun-Earth L2 point, examines the planar dynamics of the satellite. Lagrange’s equations are used to model the system, with a linear feedback controller to control the tether lengths and angular displacements of the system. The end masses were successfully controlled, yielding a spiral pattern which allows the satellite to be used as an optical interferometer.

¹³After the traditional Japanese wrapping cloth.

Chapter 3

Tether modelling

The steps to construct a mathematical model of a tether orbiting a planet are outlined in this chapter. Starting with a simple model of a point mass orbiting a massive body, each stage builds on the last and progressively a detailed (and more importantly, validated) model will be outlined.

3.1 Constructing the equations of motion of a system

A method to describe a system in terms of Ordinary Differential Equations (ODE) is outlined below. For each mass point of the system:

- the position of each mass point is described in local coordinate space
- the Centre of Mass (CoM) of the system is found
- the position is translated and rotated¹ into inertial coordinate space, using matrix and vector operations

¹The centre of mass effectively links the two coordinate systems by providing a common point of reference between the two.

then, for the system as a unit:

- the Lagrangian is found by expressing the total energy of the system
- generalised coordinates are chosen to suit the system.
- velocities of each mass point are derived
- Lagrange's equations are constructed
- Lagrange's equations may be numerically integrated using suitable initial conditions

The remainder of this chapter will fully outline the steps needed to construct and validate a general system of equations, focussing specifically on constructing a planar dumbbell tether on a circular equatorial Earth-centred orbit.

3.1.1 Validating code modules

It is essential as part of the scientific method to set up an experiment, or in this case a numerically solved mathematical model, that is both repeatable and verifiable. To this end, a method of setting up equations describing each component's position using repeatable and testable modules is introduced here.

It is of fundamental importance, when building a mathematical model, to ensure that the model is verified and validated insofar as practically possible. As such, a method of constructing a system of validated modules is introduced to verify that, for example, a module to rotate a vector about an axis does this accurately and repeatably. Therefore, for each component of the system, a testable module is produced and the system as a whole is much easier to validate as the sum of its parts.

In MathematicaTM, modules of code may be configured and tested such that a

one-line testable routine may be evaluated. Assigning:

$$\text{XRotation}[\theta] = \begin{bmatrix} 1 & 0 & 0 \\ 0 & \cos(\theta) & -\sin(\theta) \\ 0 & \sin(\theta) & \cos(\theta) \end{bmatrix} \quad (3.1)$$

it is then possible to separate and logically evaluate the right and left hand sides of Equation 3.1 to see if they are identically equal. If the right hand side is identically equal to the left hand side, the code is validated, if not, the code fails validation.

In this way, it is possible to establish a repeatable and valid technique for constructing the equations of motion of the system.

3.2 Centre of mass modelling

3.2.1 Mass points & body selection

It is essential when using the Lagrangian method that the movement of the bodies concerned are described accurately. The modelling tasks can be broadly separated into expressions concerning:

- bodies containing mass which contribute to the kinetic and potential energies
- external or internal conservative forces that may contribute to the energy sum (e.g. spring energies)
- external or internal forces that may contribute to the non-conservative right-hand-side terms in Lagrange's equations

As such, the principles of system modelling will be demonstrated using a simple example of the coplanar dumbbell tether in circular Earth orbit, shown in Figure 3.1.

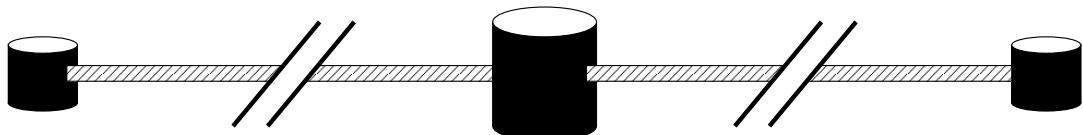


Figure 3.1: Symmetrical dumbbell tether

Central to the system, the facility mass houses the entire structure of the system; the power generation, communications equipment, etc.. This is expected to form the majority of the mass of the system.

The two payloads are the *raison d'être* of the momentum exchange tether system. They are assumed to have mass and are rigidly connected to the facility by the tethers and are usually a significantly smaller fraction of the system mass.

The two tethers are assumed to be massless. This is usually a significant assumption to make because the fractional mass of a 100 km tether is non-trivial. In this case, it is a reasonable assumption to demonstrate the principles of tether modelling without making the mathematics overly arduous.

The tethers hold the payloads rigidly and symmetrically in plane about the facility mass, ensuring that the tethers are colinear about one common axis through the centre.

The other body of note is, of course, the Earth which acts indirectly on this system providing the gravitational potential energy.

3.2.2 Centre of mass calculations

The centre of mass can have a considerable effect on the motion of this system. Consider an asymmetrical payload release, for example, when only one payload is released instead of both, as normally occurs. The centre of mass would undergo an instantaneous step-change and, consequently, the orbit of the system would change.

Assuming the dumbbell is in a circular orbit aligned along the vertical (gravity gradient) direction, if the uppermost payload is released the excess kinetic energy

of the orbit will cause the payload to describe an ellipse with the separation point as the perigee. The remainder of the system² will tend to de-orbit as the potential energy of the system is lower than needed to sustain a circular orbit. This separation point becomes the apogee of the new system's orbit, as shown in Figure 3.2.

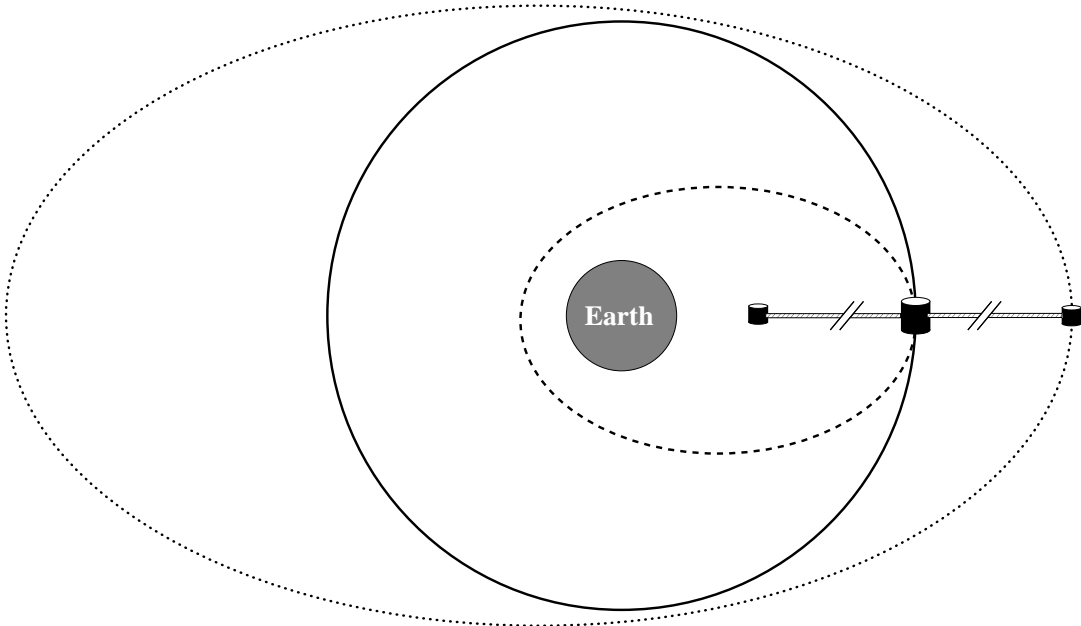


Figure 3.2: Symmetrical dumbbell tether on a circular orbit (solid). After payload release, the facility system path at apogee (dash) and payload at perigee (dots)

In a symmetrical system, the centre of mass is located coincident on the facility. If the system is asymmetrical, then the centre of mass will need to be calculated. This is highly important to the accuracy of the model and in most cases necessary to integrate the equations of motion of the system. Most of the problems encountered when numerically integrating the equations of motion in Mathematica were solved by inserting a mathematical expression that accurately describes the (variable) position of the centre of mass in the positional equations which then feed into Lagrange's equations.

The Centre of Mass (CoM) calculations give the location of the CoM from an arbitrarily chosen point. In this case it is convenient to chose the facility mass as the origin point (and the centre of a local coordinate system) and refer to all other

²That is, the lower section of the system comprising the facility, two tethers and one payload.

points in the tether system relative to the facility location.

This may be alternatively expressed as constructing a local coordinate system $\{X_{\text{local}}, Y_{\text{local}}, Z_{\text{local}}\}$ centred on the facility mass, in this case, aligning the X-axis with the radius vector.

The position of the centre of mass about the facility for n masses each with positions $\{X_i, Y_i, Z_i\}$, in terms of the local $\{X, Y, Z\}$ coordinate system centred on the facility mass is:

$$P_{\text{facility} \rightarrow \text{CoM}} = \left\{ \frac{\sum_{i=1}^n M_i X_i}{\sum_{i=1}^n M_i}, \frac{\sum_{i=1}^n M_i Y_i}{\sum_{i=1}^n M_i}, \frac{\sum_{i=1}^n M_i Z_i}{\sum_{i=1}^n M_i} \right\} \quad (3.2)$$

Once the CoM relative to the facility mass has been found, a vector describing the position of any mass point in the inertial frame of reference³ may be constructed.

This is used in later equations by taking the position *from* the centre of mass *to* the facility mass:

$$P_{\text{CoM} \rightarrow \text{facility}} = -P_{\text{facility} \rightarrow \text{CoM}} \quad (3.3)$$

3.2.3 Positions of mass points

A technique to obtain the location of each mass point relative to the facility is outlined below, using a 2D dumbbell system as an illustrative example.

To assemble the equations of motion, a series of rotations and translations are performed on the initial vectors to transform the local space coordinates into inertial space coordinates. The initial vectors are chosen in synchronisation with the generalised coordinates and the rotation angles.

Figure 3.3 shows the orbital motion, constrained to the inertial X-Y plane and the local X-Y plane, of an asymmetric dumbbell tether. Note that the local X-axis is

³In the Earth centred system.

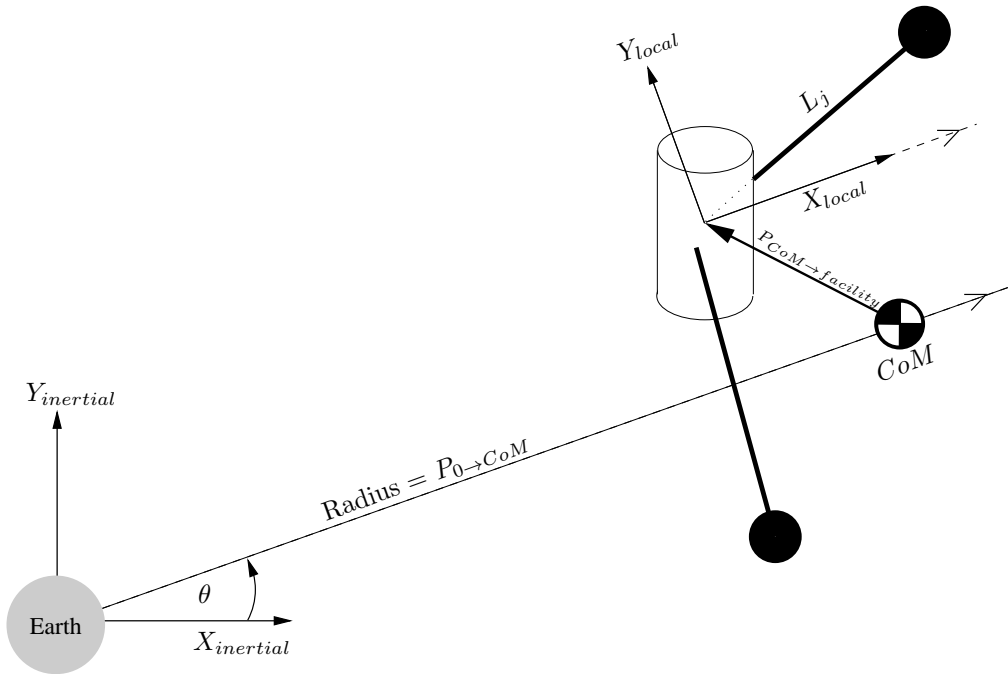


Figure 3.3: Asymmetrical dumbbell in inertial axes

parallel to the radius vector.

The inertial position vector P_{inertial} of each mass point, j , is assembled from the vector sum of the component vectors, taking into account the translation and rotation of each component.

$$P_{j_{\text{inertial}}} = R_{\theta,Z} \cdot \left(P_{0 \rightarrow \text{CoM}} - P_{\text{facility} \rightarrow \text{CoM}} + (R_{\psi_j,Z} \cdot L_j) \right) \quad (3.4)$$

Where $P_{0 \rightarrow \text{CoM}} = \{R, 0, 0\}$, and represents the vector of the centre of mass from Earth⁴. The rotation matrices and matrix notation $R_{\psi_j,X}$ are explained in Section 3.5.

The five stages in constructing the position of the mass point P_j are shown in Figures 3.4, 3.5, 3.6, 3.7 and 3.8, and the position vectors for an arbitrary mass point are given in Equations 3.5, 3.6, 3.7, 3.8, 3.9 and 3.10.

Figure 3.4 shows the mass point aligned along the X-axis of the local coordinate system, in this case using a payload mass with length L as an illustrative example.

⁴i.e. the Radius vector.

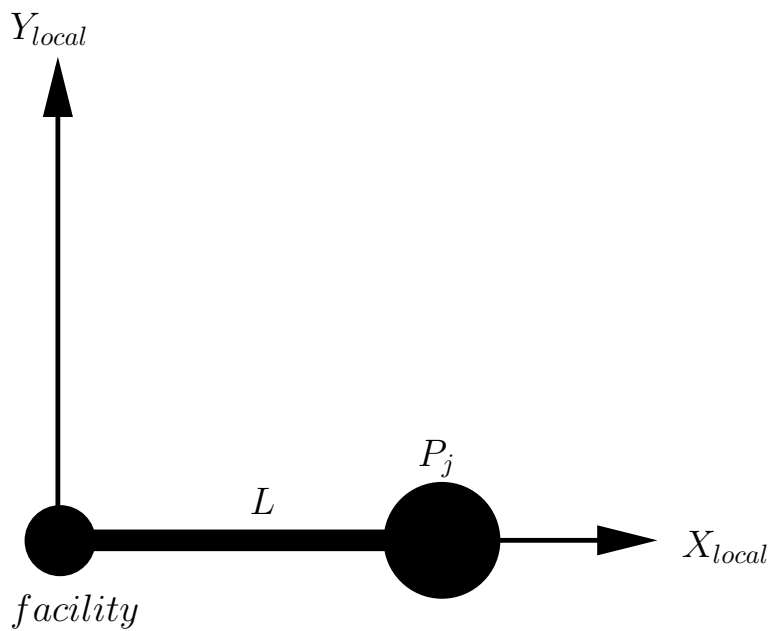


Figure 3.4: Local coordinate construction

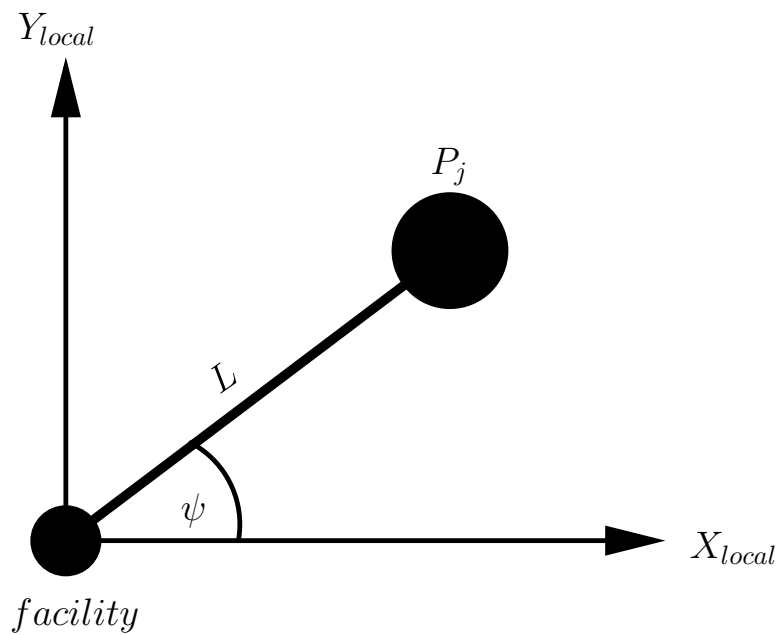


Figure 3.5: Local coordinate construction after rotation through angle ψ about the facility mass

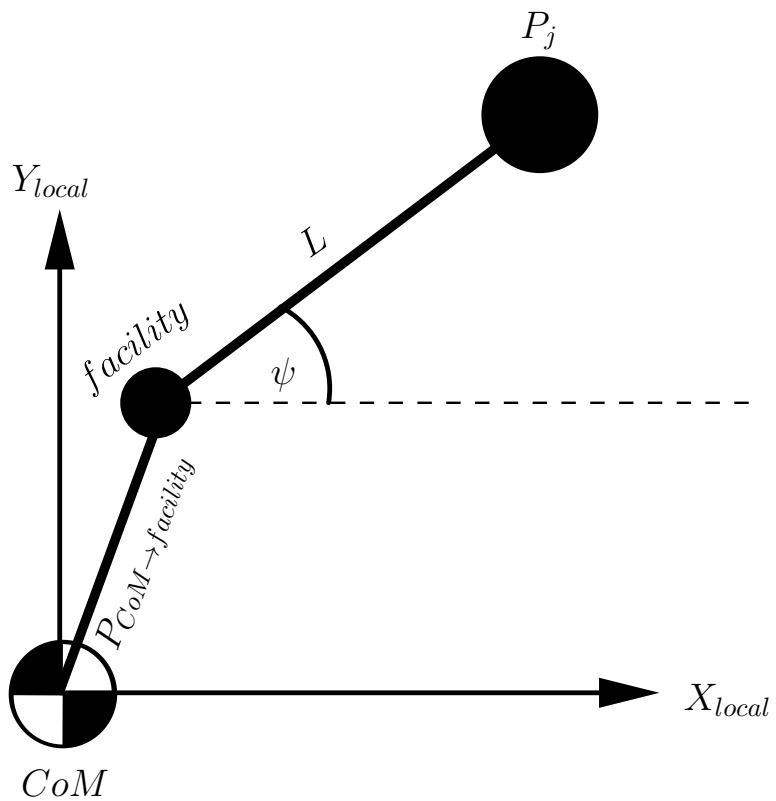


Figure 3.6: Local coordinate construction after translation from the facility to the CoM

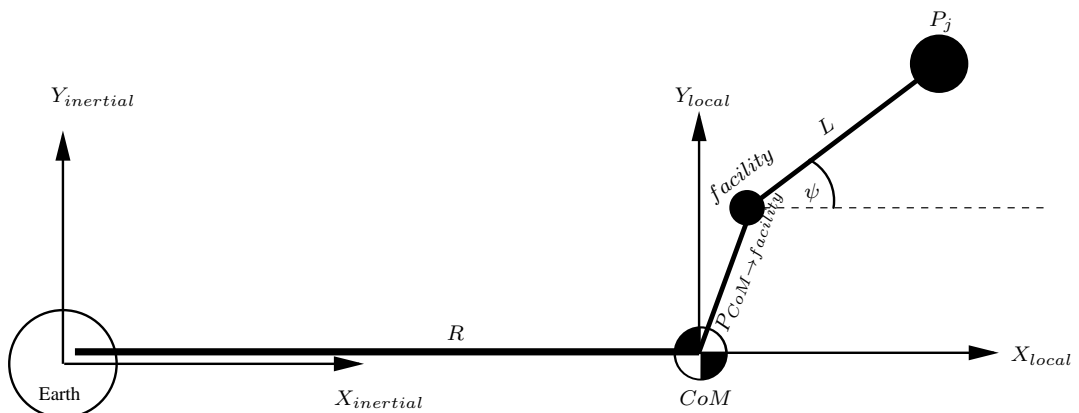


Figure 3.7: Local coordinate construction after translation from the CoM to the inertial coordinate system

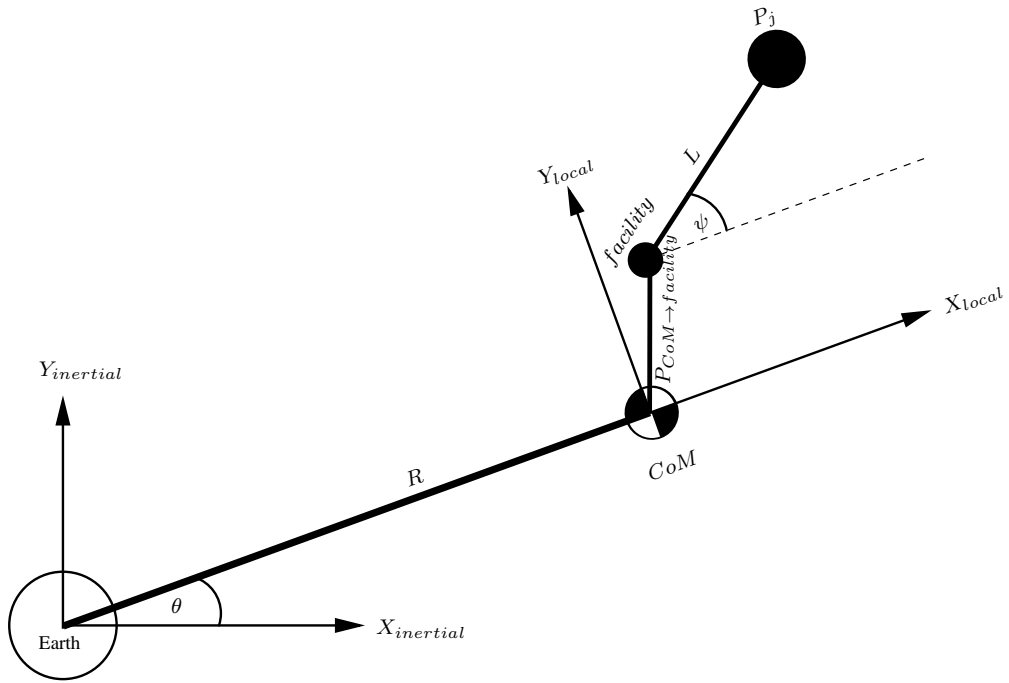


Figure 3.8: Local coordinate construction after rotation through θ about the inertial coordinate system

Rotating this through an angle of ψ about the facility as shown in Figure 3.5. This is translated to align the origin with the centre of mass as shown in Figure 3.6. A further translation is performed through the inertial X-axis about a distance R , giving the origin as the inertial coordinate system, as shown in Figure 3.7. Finally, the inertial coordinate system is rotated about the origin around an angle θ as shown in Figure 3.8.

The vectors of each are shown below:

$$P_1 = \begin{pmatrix} L \\ 0 \\ 0 \end{pmatrix} \quad (3.5)$$

$$P_2 = R_{\psi, Z} \cdot P_1 = \begin{pmatrix} L \cos(\psi) \\ L \sin(\psi) \\ 0 \end{pmatrix} \quad (3.6)$$

$$P_3 = P_2 - P_{\text{CoM} \rightarrow \text{facility}} = \begin{pmatrix} L \cos(\psi) & -\text{CoM}_X \\ L \sin(\psi) & -\text{CoM}_Y \\ & -\text{CoM}_Z \end{pmatrix} \quad (3.7)$$

$$P_4 = P_3 + R = \begin{pmatrix} L \cos(\psi) & -\text{CoM}_X & +R \\ L \sin(\psi) & -\text{CoM}_Y & \\ & & -\text{CoM}_Z \end{pmatrix} \quad (3.8)$$

$$P_5 = R_{\theta, Z} \cdot P_4 = \begin{pmatrix} \cos \theta (L \cos(\psi) - \text{CoM}_X + R) - \sin \theta (L \sin(\psi) - \text{CoM}_Y) \\ \sin \theta (L \cos(\psi) - \text{CoM}_X + R) + \cos \theta (L \sin(\psi) - \text{CoM}_Y) \\ -\text{CoM}_Z \end{pmatrix} \quad (3.9)$$

$$P_5 = R_{\theta, Z} \cdot \left(P_{0 \rightarrow \text{CoM}} - P_{\text{facility} \rightarrow \text{CoM}} + (R_{\psi, Z} \cdot P_1) \right) \quad (3.10)$$

The process is repeated for each mass point under consideration.

3.3 Constructing Lagrange's equations

Lagrangian mechanics is primarily concerned with the trajectory of an object, derived by finding the path which minimises the action, a quantity which is the integral

of the Lagrangian over time. As this is an energy based approach, the process of evaluating the kinetic and potential energy of the system will be outlined and the choice of generalised coordinates will be explained.

3.3.1 Energy modelling

For every mass point in the system with position in the inertial frame, P_j , the following steps are undertaken in order to find the Lagrangian energy expression \mathbb{L} :

1. the respective velocities, V_j are found:

$$V_j = \frac{\partial}{\partial t}(P_j) \quad (3.11)$$

2. the kinetic energies (linear $T_{\text{lin}} = \frac{1}{2}mv^2$ and rotational $T_{\text{rot}} = \frac{1}{2}I\omega^2$) are obtained and summed:

$$T_{\text{lin}} = \sum_{j=1}^n \frac{1}{2}m_j V_j \cdot V_j \quad (3.12)$$

$$T_{\text{rot}} = \sum_{j=1}^n \frac{1}{2}m_j P_{i_{\text{local}}} \cdot P_{j_{\text{local}}} \omega_j \cdot \omega_j \quad (3.13)$$

where the vector of angular velocity, ω_j is the first derivative of the angular position of each point, $\{\phi_j, \alpha_j, \psi_j\}$

3. the potential energies, U , are obtained and summed:

$$U = \sum_{j=1}^n \frac{\mu m_j}{|P_j|} = \sum_{j=1}^n \frac{\mu m_j}{\sqrt{P_j \cdot P_j}} \quad (3.14)$$

where μ is the standard gravitational parameter. For the Earth, the value is $\mu = 3.986 * 10^{14} \text{ m}^3/\text{s}^2$.

4. and the Lagrangian is found:

$$\mathbb{L} = T_{\text{rot}} + T_{\text{lin}} - U \quad (3.15)$$

For each mass point, the Lagrangian energy expression is constructed by considering the total kinetic and potential energies of the system.

$$\frac{d}{dt} \left(\frac{\partial T}{\partial \dot{q}_j} \right) - \frac{\partial T}{\partial q_j} + \frac{\partial U}{\partial q_j} = Q_j \quad (3.16)$$

Lagrange's equations are generated for all the generalised coordinates as specified in Equation 3.16.

The forces are then used to calculate the right hand side of Lagrange's equations, Q_j , through consideration of the virtual work.

Primarily, the main non-conservative force acting on the tether system will be the motor torque. This concept is covered further in Ziegler's Ph.D. thesis [Ziegler, 2003, p43-45].

3.3.2 Choosing generalised coordinate systems

The generalised coordinates used in deriving Lagrange's equations in Section 3.3 are chosen to be independent coordinates. These coordinates need not be orthogonal nor Cartesian, in fact it is limiting to assume they are either, however they must describe an independent degree of freedom of the system.

In the case of the orbital variables R and θ , these are chosen in preference to the inertial variables X_{inertial} and Y_{inertial} to enable periodic analysis over the orbital cycle.

In the local coordinate system, the choice of a generalised coordinate is less straightforward. In a two generalised coordinate system with an in-plane and out-of-plane motion, there are many angles that could be chosen as the generalised coordinate, and this poses a problem over choice of variables. The equations of motion (and therefore the corresponding set of Lagrange's equations) that describe one system of rotations would be different from the others, but the motion would have to be

identical when comparing the many possible rotations systems. This implies that for the motion to be identical⁵ there could be many possible systems of equations that could, when integrated, provide the motion of the system, and that there may be one or more systems of equations that provide a more elegant solution than the rest. Two systems of rotations are investigated in Section 3.5.

The goal in selecting a “good” choice of generalised coordinates is that they are easily interpreted in graphical form, and the equations generated are compact and meaningful to interpret.

3.4 Non-conservative forces

Any non-conservative forces that appear in the system need to be included in the equations of motion in terms of virtual work. These are contained within Ziegler’s Ph.D. Thesis [Ziegler, 2003, p43-45], and will be contextualised here.

The non-conservative force is represented by Q_j and can be evaluated by considering the virtual work done by the motor torque summed over each mass:

$$Q_j = \sum_{\text{mass}} F \cdot \frac{\partial P_{\text{mass}}}{\partial q_j} \quad (3.17)$$

with j representing each of the n chosen generalised co-ordinates and P_{mass} as the position vector of the mass under consideration. F is the non-conservative force.

The 3×3 rotation matrix for a generalised rotation in the tether body axes⁶ (as will be explained in Section 3.5) is multiplied by the length vector to give the position

⁵If the systems were non-identical then, generally speaking, there would either be flaw when choosing the generalised coordinates or a mistake in the equations. The process of simulating the motion of a system should be entirely independent of the means used to arrive at the end result!

⁶Rotations are only provided here for the Y- and Z-axis.

of each mass in the tether body axes :

$$P_{\text{mass}} = R_{\alpha,Y} \cdot R_{\psi,Z} \cdot \begin{pmatrix} L_{\text{mass}} \\ 0 \\ 0 \end{pmatrix} \quad (3.18)$$

The resultant 3×1 vector is differentiated with respect to each of the n chosen generalised co-ordinates to give an $n \times 3$ matrix. The force vector expressed in tether body axes is then found by multiplying the generalised rotation matrix by the force vector:

$$\text{Force} = R_{\gamma,X} \cdot R_{\alpha,Y} \cdot R_{\psi,Z} \cdot \begin{pmatrix} 0 \\ 0 \\ \tau/L_{\text{mass}} \end{pmatrix} \quad (3.19)$$

where τ is the non-conservative force converted into the rotating frame.

The dot product of the 3×1 force vector and the $n \times 3$ matrix then gives an $n \times 1$ vector containing the Q_j terms for the n chosen generalised co-ordinates to be used in the right hand side of the equations of motion.

3.5 Rotation systems

A comparison will now be made between two rotation systems that specify the position of an arbitrary mass point in the local axes system.

As discussed earlier⁷ there are multiple ways to specify the position of the mass. No one system may be termed *the* definite solution, however, one may be preferable to choose if it generates a more easily interpreted system of equations.

⁷See section 3.3.2.

3.5.1 Rotation summary

Three rotation matrices are set up to describe the direction of a single 3D vector about its origin using a series of rotations about the local X-, Y- and Z-axes.

As the three rotations can rotate an arbitrary vector around the origin, the initial vector must be defined. For the rotation systems that follow, a vector aligned with the X-axis in the positive direction starting at the origin has been chosen. The series of rotations are then performed sequentially to give 3 new coordinate axes (two intermediate and one final) for 3 rotations.

The Rotation $R_{\kappa,B}$ is defined here as a rotation matrix acting about the B-axis and rotating about an angle κ .

The new vector is found by rotating the starting vector coordinates by means of three rotation matrices about the local origin. The rotation system will be one of the six permutations from the list of three possible rotations: $R_{\delta,X}$, $R_{\alpha,Y}$ and $R_{\psi,Z}$ given in Equations 3.20, 3.21 and 3.22.

The rotation system that rotates the point first around the X-axis, then the Y-axis, then the Z-axis is termed the XYZ rotation system.

$$R_{\delta,X} = \begin{bmatrix} 1 & 0 & 0 \\ 0 & \cos(\delta) & -\sin(\delta) \\ 0 & \sin(\delta) & \cos(\delta) \end{bmatrix} \quad (3.20)$$

$$R_{\alpha,Y} = \begin{bmatrix} \cos(\alpha) & 0 & \sin(\alpha) \\ 0 & 1 & 0 \\ -\sin(\alpha) & 0 & \cos(\alpha) \end{bmatrix} \quad (3.21)$$

$$R_{\psi,Z} = \begin{bmatrix} \cos(\psi) & -\sin(\psi) & 0 \\ \sin(\psi) & \cos(\psi) & 0 \\ 0 & 0 & 1 \end{bmatrix} \quad (3.22)$$

The order of matrix multiplication is important; for the XYZ rotation sequence, the vector multiplication is evaluated sequentially from the right hand side:

$$\begin{aligned} & R_{\psi,Z} \cdot R_{\alpha,Y} \cdot R_{\delta,X} \cdot P_{\text{orig.}} \\ &= R_{\psi,Z} \cdot \left(R_{\alpha,Y} \cdot \left(R_{\delta,X} \cdot P_{\text{orig.}} \right) \right) \end{aligned}$$

Note well, this differs from the ZYX rotation system in the order of rotations. The ZYX rotation system first rotates the vector by the Z-axis, then the Y-axis, then the X-axis.

$$\begin{aligned} & R_{\delta,X} \cdot R_{\alpha,Y} \cdot R_{\psi,Z} \cdot P_{\text{orig.}} \\ &= R_{\delta,X} \cdot \left(R_{\alpha,Y} \cdot \left(R_{\psi,Z} \cdot P_{\text{orig.}} \right) \right) \end{aligned}$$

When looking at the matrix rotation equation, this may seem counter-intuitive to label the rotational sequence from right to left⁸. However, it reflects the sequence of rotations, even if it is backwards from a point of view of reading the matrix multiplication subscripts.

Using the three rotations given here in the three axes, there are 6 possible combinations of defining a rotational sequence, as shown in Table 3.1. These describe the sequence of rotations when rotating a point around the origin in 3D and the three possible rotations in 2D that may be derived from the 3D rotation.

The 2D rotations are not unique to a single 3D rotation. For example there are three XY rotations that may be made in 2D that correspond to **XZY**, **XZY** or **ZXY** rotations in 3D space.

Two of these sequences will be investigated using a simple 2D rotation with the

⁸Indeed, this is a rather arbitrary decision, but it could be argued that this follows the arbitrary direction of text in-keeping with the custom of languages of the Western hemisphere. In choosing the nomenclature, it makes sense to make XYZ define the rotational sequence rather than the order in which the matrices are multiplied purely because most non-specialists would grasp the concept of order of rotations before learning three-dimensional matrix algebra!

Order of rotation in ...					
3D			2D		
$R_{\delta,-}$	$R_{\alpha,-}$	$R_{\psi,-}$	1	2	3
X	Y	Z	XY	XZ	YZ
X	Z	Y	XZ	XY	ZY
Y	X	Z	YX	YZ	XZ
Y	Z	X	YZ	YX	ZX
Z	X	Y	ZX	ZY	XY
Z	Y	X	ZY	ZX	YX

Table 3.1: Order of rotations in 3D and 2D

sequence of rotations about the YZ- and ZY- axes, in Section 3.5.2 and Section 3.5.3 respectively.

3.5.2 YZ Rotations

The YZ series of rotations⁹ rotates a point lying on the X-axis around first the Y-axis, then the Z-axis. The X-axis rotation is not included in this system for ease of visualisation.

Rotating the original vector $P_{\text{orig.}} = \{L, 0, 0\}^T$, shown in Figure 3.9a about the Y-axis through an angle of α gives the following, as shown in Figure 3.9b:

$$P_{\text{inter-YZ}} = R_{\alpha,Y} \cdot P_{\text{orig.}} = \begin{pmatrix} L \cos(\alpha) \\ 0 \\ -L \sin(\alpha) \end{pmatrix} \quad (3.23)$$

Rotating this intermediate stage around the Z-axis through an angle of ψ gives the

⁹Or to be specific the XYZ series of rotations in 3D space when the X rotation is zero.

following, as shown in Figures 3.9c and 3.9d:

$$P_{\text{final-YZ}} = R_{\psi, Z} \cdot P_{\text{inter-YZ}} = \begin{pmatrix} L \cos(\alpha) \cos(\psi) \\ L \cos(\alpha) \sin(\psi) \\ -L \sin(\alpha) \end{pmatrix} \quad (3.24)$$

A diagram of the complete rotation sequence is shown in Figure 3.9e.

The out-of-plane angle given by the YZ series of rotations is the angle α . However, the in-plane angle **is not** the angle ψ . The in-plane angle lies in the plane normal to the Z_{YZ} plane, and intersects the XZ plane.

The in-plane angle (given by the $X_Y - X_{YZ}$ plane) is projected onto the XY-inertial plane to give the angle ψ .

3.5.3 ZY Rotations

The ZY system of rotations is generated by rotating the starting vector aligned with the X-axis around first the Z-axis, then the Y-axis. This can be thought of as the ZYX series of rotations with a zero X-axis rotation – therefore giving only a ZY rotation.

Rotating the original vector $P_{\text{orig.}} = \{L, 0, 0\}^T$, shown in Figure 3.10a about the Z-axis through an angle of ψ gives the following, as shown in Figure 3.10b:

$$P_{\text{inter-ZY}} = R_{\psi, Z} \cdot P_{\text{orig.}} = \begin{pmatrix} L \cos(\psi) \\ L \sin(\psi) \\ 0 \end{pmatrix} \quad (3.25)$$

Rotating this intermediate stage around the Y-axis through an angle of α gives

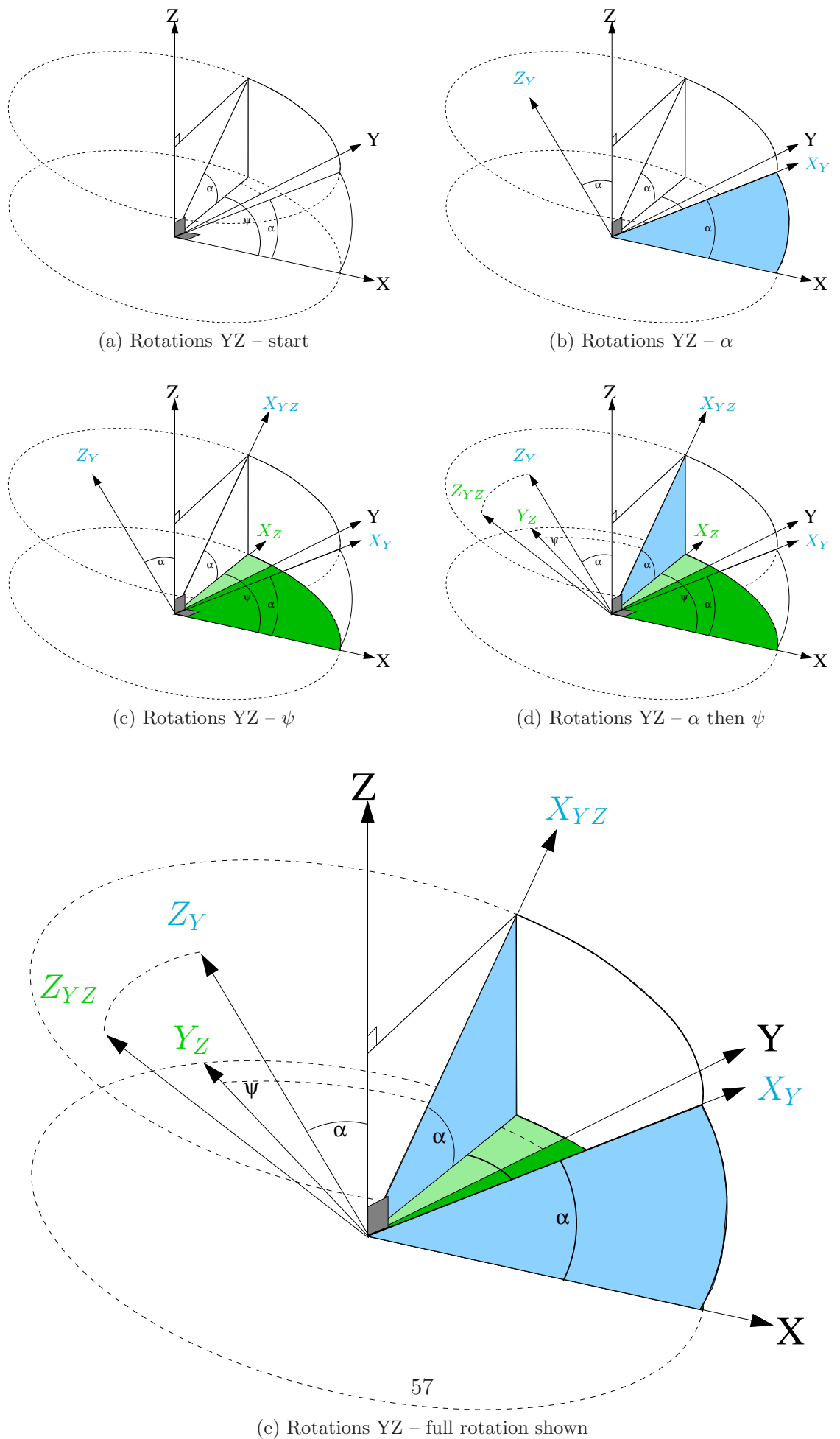


Figure 3.9: Rotation sequence for YZ rotation: Rotating α about Y-axis then ψ about Z-axis. α is shown as a negative rotation here for ease of visualisation.

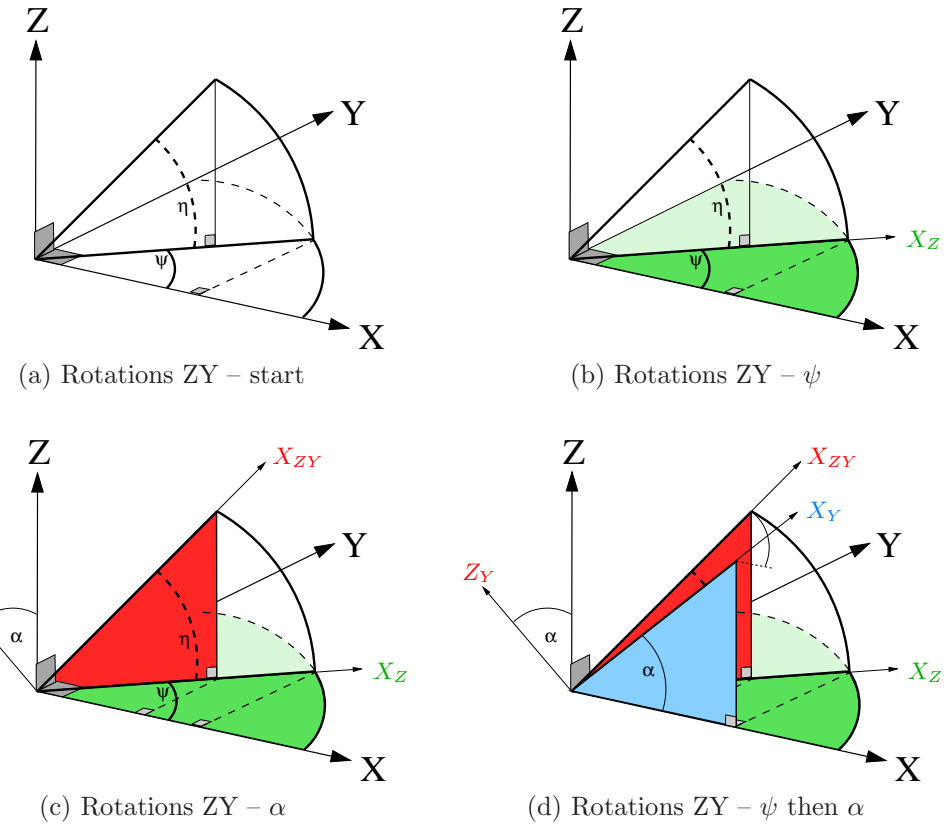


Figure 3.10: Rotation sequence for ZY rotation.. Rotating ψ about Z-axis then α about Y-axis. α is shown as a negative rotation here for ease of visualisation.

the following, as shown in Figures 3.10c and 3.10d:

$$P_{\text{final-ZY}} = R_{\alpha, Y} \cdot P_{\text{inter-ZY}} = \begin{pmatrix} L \cos(\psi) \cos(\alpha) \\ L \sin(\psi) \\ -L \cos(\psi) \sin(\alpha) \end{pmatrix} \quad (3.26)$$

A diagram of the complete rotation sequence is shown in Figure 3.10d.

Conversely to the YZ series of rotations, the out-of-plane angle given by the ZY series of rotations **is not** the angle α . However, the in-plane angle **is** now the angle ψ . The out-of-plane angle is given by the angle in the $X_{ZY} - X_Z$ plane between the fully rotated vector and the $X_0 - Y_0$ inertial plane.

The out-of-plane angle (given by the $X_{ZY} - X_Z$ plane) is projected onto the XY-inertial plane to give the angle α .

The out-of-plane angle, η , may be found by simple trigonometry as follows:

$$\sin \eta = \frac{Z_{P_{\text{final-ZY}}}}{L} \quad (3.27)$$

$$\eta = \sin^{-1}(-\cos(\psi) \sin(\alpha)) \quad (3.28)$$

3.5.4 Comparing the equations – position equations

In each of the rotation sets, the x-coordinate is identical. The sets differ in the y- and z-coordinate sets as follows:

YZ y-coord: $L \cos(\alpha) \sin(\psi)$ from Equation 3.24

ZY y-coord: $L \sin(\psi)$ from Equation 3.26

The y-coordinates differ by a factor of $\cos(\alpha)$ between the YZ and ZY systems.

YZ z-coord: $-L \sin(\alpha)$ from Equation 3.24

ZY z-coord: $-L \cos(\psi) \sin(\alpha)$ from Equation 3.26

The z-coordinates differ by a factor of $\cos(\psi)$ between the YZ and ZY systems.

The two sets of 3D rotations are different because of the commutative rules of matrix multiplication, in general when multiplying two rotation matrices A and B the matrix product AB will be different from BA.

3.5.5 Comparing the equations – kinetic energies

Comparing the differences in the kinetic energies of the spinning systems in a local coordinate system:

$$\text{YZ } E_k = \frac{m}{2} L^2 \left(\dot{\alpha}^2 + \cos(\alpha)^2 \dot{\psi}^2 \right)$$

$$\text{ZY } E_k = \frac{m}{2} L^2 \left(\dot{\psi}^2 + \cos(\psi)^2 \dot{\alpha}^2 \right)$$

Clearly, the two are similar – the difference essentially being the substitution of one angle for the other between the two sets of equations.

3.5.6 Comparing the equations – potential energies

Comparing the differences in the potential energies of the spinning systems in an inertial coordinate system is a stage more complicated, as the local coordinate system must be translated from the local centre to the inertial centre to incorporate the full inertial terms.

The potential energy term for each mass point j

$$E_p = \frac{\mu m_j}{\sqrt{p_j \cdot p_j}}$$

depends strongly on the magnitude of distance, given by $\sqrt{p_j \cdot p_j}$. This evaluates to the following for YZ and ZY rotations¹⁰

$$\text{YZ: } p_j = \{R + L \cos(\alpha) \cos(\psi), L \cos(\alpha) \sin(\psi), -L \sin(\alpha)\}$$

$$\text{ZY: } p_j = \{R + L \cos(\alpha) \cos(\psi), L \sin(\psi), -L \cos(\psi) \sin(\alpha)\}$$

Therefore

$$\text{YZ: } \sqrt{p_j \cdot p_j} = L^2 + R^2 + 2 L R \cos(\alpha) \cos(\psi)$$

$$\text{ZY: } \sqrt{p_j \cdot p_j} = L^2 + R^2 + 2 L R \cos(\alpha) \cos(\psi)$$

For the potential energy term:

$$\text{YZ } E_p = \frac{\mu m_j}{\sqrt{L^2 + R^2 + 2 L R \cos(\alpha) \cos(\psi)}}$$

$$\text{ZY } E_p = \frac{\mu m_j}{\sqrt{L^2 + R^2 + 2 L R \cos(\alpha) \cos(\psi)}}$$

That is, the potential energy expression of the two sets of equations YZ and ZY are identical for an inertially planar system.

When the orbital rotation θ is introduced to the potential energy equations, the result will be identical to the expression above, as the inertial rotation through $R_{\theta,Z}$ is a rotation about one axes only, unlike the dual system of rotations outlined above.

The expression for potential energy will change significantly when rotated through

¹⁰With a simple offset from the origin by R, representing the orbital radius.

around the orbit in 3D when the orbital parameter ι is included.

3.5.7 YZ rotation in inertial axes

The full rotation sequence in inertial axes, for a rotation of an initial vector through a Y-axis rotation, then a Z-axis rotation, translations in CoM and radius vector, then a final rotation about the Z-axis is as follows:

$$P_{\text{final}} = R_{\theta, \text{Z}} \cdot (P_{0 \rightarrow \text{CoM}} - P_{\text{facility} \rightarrow \text{CoM}} + (R_{\psi, \text{Z}} \cdot R_{\alpha, \text{Y}} \cdot P_1)) \quad (3.29)$$

3.5.8 Singularities in the rotational systems

The main disadvantage in using the method of rotational matrices is they have singularities or ‘gimbal lock’ points where there is a lack of a unique output when a rotation is performed that aligns it with the rotational axis.

In the case of YZ rotation, an initial rotation of 90° about the Y-axis would align the original vector with the Z-axis. A second rotation about the Z-axis would be redundant as the vector would not change value.

In the case of ZY rotation, an initial rotation of 90° about the Z-axis would align the original vector with the Y-axis. A second rotation about the Y-axis would be redundant as the vector would not change value.

In general, any rotation through 90° , 270° (or any multiples thereof) so that the original vector aligns itself with the new axes of rotation will produce a singularity.

The equations of motion usually can not be numerically integrated with the initial condition as a singularity; the lack of uniqueness of the solution violates the method of using the Lagrangian to solve the equations of motion.

3.5.9 Practical uses of the different equations

The two sets of equations above may find different applications, depending on the desired investigative outcome required.

If a system of equations is needed to solve a solution space near an axis, then naturally, the system of equations should be chosen to avoid a singularity. As the choice of system of equations is entirely arbitrary, the problem of singularities has been avoided here.

Quaternions were considered as an alternative to the three-angle rotation system above - they confer several advantages such as the ability to multiply the rotations in one polynomial and they are not prone to gimbal lock. However, one of the main disadvantages of quaternions is that it is very difficult to extract physical meaning from the individual components without a significant degree of post-processing. For this reason, it was decided to remain with the three-angle rotation method.

The YZ system of equations is slightly more compact and easier to interpret than the ZY equations, although both give identical results when integrated. The difference in time taken to solve the two sets of equations differs by approximately 5% using a wide range of initial conditions.

3.6 Numerical integration techniques

The equations of motion, once assembled, are integrated with Mathematica¹¹ using the NDSolve subroutine. This is a Jack-of-all-trades solution that effectively deals with the problems of choosing timesteps, any stiffness that may arise and a multitude of other problems that plague the researcher. However, care must be taken to assure that the output of the numerical integrator is representative of real life – validation and sanity-checking at all stages will not ensure poor results are entirely eliminated,

¹¹Specifically, using Mathematica version 5.1

but they will reduce the risk of spurious results.

The generated equations are solved with Mathematica's general purpose solver `NDSolve[...]` with the following parameters:

- **AccuracyGoal** → **Automatic**, **PrecisionGoal** → **Automatic** – controls the number of digits of accuracy, effectively the absolute and relative errors respectively.
- With **PrecisionGoal** → **p** and **AccuracyGoal** → **a**, Mathematica attempts to make the numerical error in a result of size x be less than $10^{-a} + |x|10^{-p}$.
- **WorkingPrecision** → **20** – limits internal computations to 20-digit precision.

From the online Mathematica NDSolve FAQ webpage – [Wolfram, 2007]:

“For initial value problems, NDSolve uses an Adams Predictor-Corrector method for non-stiff differential equations and backward difference formulas (Gear method) for stiff differential equations. It switches between the two methods using heuristics based on the adaptively selected step size. It starts with the non-stiff method under essentially all conditions and checks for the advisability of switching methods every 10 or 20 steps.

The algorithms and the heuristics for switching between algorithms are described in the following references: [Hindmarsh, 1983], [Petzold, 1983] ”

More in-depth information about the NDsolve functions is also available from the Mathematica Journal: [Keiper, 1992].

Chapter 4

Dynamics of tethers with inclination

The simple dumbbell tether model can be expanded to include an inclination component to the orbit.

The process of adding the inclination term will be exemplified with a tether payload delivery to the Moon under a time-varying inclination given by the Saros cycle, which describes the inclination variation of the Moon's orbit around the Earth.

The Saros cycle describes the Moon's orbital inclination cycle, lasting 18 years 11 days and 8 hours, cutting the Sun's ecliptic plane (used as the inertial coordinate plane). This cycle determines, in the short term at least, the Lunar and Earth's eclipse frequencies and locations. This also allows the inclination of the Moon to be accurately predicted from ephemeral data. Figure 4.1 shows the inclination as a function of time over one Saros cycle with data taken from the JPL Horizons website [JPL, 2008].

As shown in Figure 4.1, the Saros cycle varies from a maximum inclination with respect to the geocentric plane of approximately 28.8° to a minimum of 18.0° , which

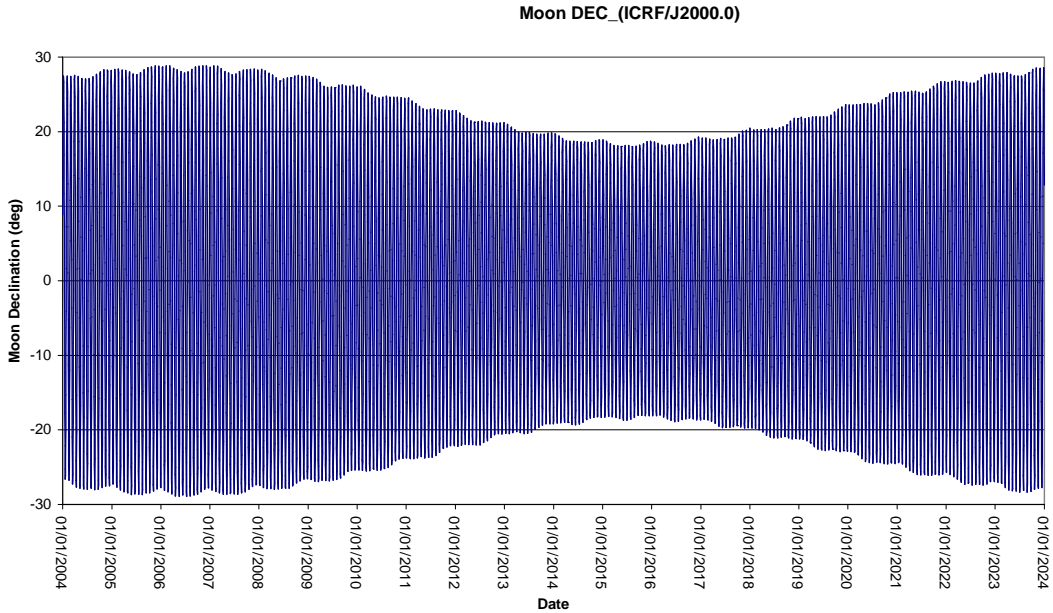


Figure 4.1: Ephemeris of Lunar orbital inclination [JPL, 2008]

poses a problem to the trajectory and mission specialists of a long-term reusable launch system, like the MMET. The position of the Moon changes, which makes it more difficult to launch a Lunar mission, and the cost of the mission will change due to a potentially expensive¹ plane change manoeuvre.

Comparing the Lunar inclination to Earth's tilt of 23.5° , the Moon's inclination with respect to Earth's equatorial plane varies by approximately $\pm 5^\circ$. The ΔV required to perform an inclination change will be small, but the dynamics of the system will depend on the inclination with respect to the inertial plane. In 2008, this is approximately 28° .

4.1 Addition of inclination to tether model

The expansion of the tether model to include an inclination term is relatively straightforward, at least in terms of the model outlined in Section 3.5.7. The inclination term is added with a rotation matrix² $R_{\iota,Y}$ before the final inertial rotation

¹In terms of fuel and therefore cost.

²Rotating around the Y-axis through the inclination angle, ι .

sequence $R_{\theta,Z}$ is performed.

The full rotation sequence in inertial axes, for a rotation of an initial vector through a local Y-axis rotation, then a local Z-axis rotation, translations with the CoM and radius vectors, then two rotations about the (recently created) inertial Y-axis, then the inertial Z-axis is as follows:

$$P_{\text{final}} = R_{\theta,Z} \cdot R_{\iota,Y} \cdot (P_{0 \rightarrow \text{CoM}} - P_{\text{facility} \rightarrow \text{CoM}} + (R_{\psi,Z} \cdot R_{\alpha,Y} \cdot P_1)) \quad (4.1)$$

As in Section 3.3, Lagrange's equations will now be derived for the system including the orbital inclination.

4.1.1 5 degree of freedom model

Five variables of interest are chosen – $\{R, \theta, \iota, \psi, \alpha\}$ – that fulfil all the requirements of generalised coordinates. An analysis will be performed to investigate the effect the inclination variable has on the tether system orbit.

The mathematical model will be constructed to include a symmetrical dumbbell tether with a facility mass at the centre of the system. The important mass points included in the model are the two identical payload masses, M_{payload} , the facility mass, M_{facility} , and the tether masses, M_{tether} , which are concentrated at the centre of each tether.

The orbital system $\{R, \theta, \iota\}$ is conceptually separated from the local rotation system $\{\psi, \alpha\}$. The equations of motion for the orbit are constructed as one concentrated point mass, and the local rotational system is superimposed on this orbit. This allows a significantly simpler representation of the equations, however, this does not allow the orbital motion to be influenced by the local rotations. Overall, this assumption is valid and should give an insight into the broad motions of the MMET on an inclined orbit.

The stator is not included in this model because this would significantly increase the complexity of the system.

4.2 Constructing the equations of motion

The sequence of rotations follows the YZ system of rotations as described earlier in Section 3.5.2.

Manipulating the position vector from the original Equation 4.1, the rotation matrices are collected through the commutative properties of matrices and terms containing the Radius vector, $P_{0 \rightarrow \text{CoM}}$, and the local vector³, P_1 , are separated:

$$P_{\text{final}} = R_{\theta,Z} \cdot R_{\iota,Y} \cdot (P_{0 \rightarrow \text{CoM}} - P_{\text{facility} \rightarrow \text{CoM}} + (R_{\psi,Z} \cdot R_{\alpha,Y} \cdot P_1)) \quad (4.2)$$

$$P_{\text{final}} = R_{\theta,Z} \cdot R_{\iota,Y} \cdot (P_{0 \rightarrow \text{CoM}} - P_{\text{facility} \rightarrow \text{CoM}}) + R_{\theta,Z} \cdot R_{\iota,Y} \cdot R_{\psi,Z} \cdot R_{\alpha,Y} \cdot P_1 \quad (4.3)$$

Taking the assumption that the dumbbell is symmetric about the facility mass:

$$P_{\text{facility} \rightarrow \text{CoM}} = 0 \Rightarrow \begin{pmatrix} \text{CoM}_X \\ \text{CoM}_Y \\ \text{CoM}_Z \end{pmatrix} = \begin{pmatrix} 0 \\ 0 \\ 0 \end{pmatrix}$$

gives the simplified positional equation P_{final} for a single mass point, P_1 in the inertial coordinate system:

$$P_{\text{final}} = R_{\theta,Z} \cdot R_{\iota,Y} \cdot (P_{0 \rightarrow \text{CoM}}) + R_{\theta,Z} \cdot R_{\iota,Y} \cdot R_{\psi,Z} \cdot R_{\alpha,Y} \cdot P_1 \quad (4.4)$$

³The local vector is the position vector between the facility and payload 1.

When evaluated, this becomes:

$$P_{\text{final}} = R \begin{pmatrix} \cos \iota \cos \theta \\ \cos \iota \sin \theta \\ -\sin \iota \end{pmatrix} + L \begin{pmatrix} \cos \alpha(\cos \theta \cos \iota \cos \psi - \sin \theta \sin \psi) - \cos \theta \sin \alpha \sin \iota \\ \cos \alpha(\cos \iota \cos \psi \sin \theta + \cos \theta \sin \psi) - \sin \alpha \sin \theta \sin \iota \\ -\cos \iota \sin \alpha - \cos \alpha \cos \psi \sin \iota \end{pmatrix} \quad (4.5)$$

The purpose of separating the inertial and local systems in Equation 4.5 is that Lagrange's equations are easier to derive and subsequently, the equations of motion are computationally more efficient to solve.

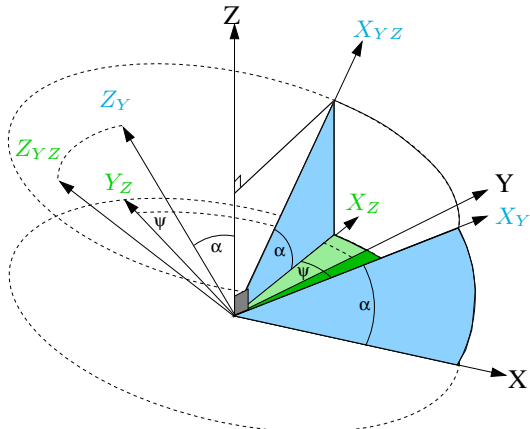
4.2.1 Rotations in the local coordinate system

Figures 4.2a, 4.2b, 4.3a and 4.3b show the sequence of rotations needed to assemble Equation 4.4: $R_{\theta,Z} \cdot R_{\iota,Y} \cdot R_{\psi,Z} \cdot R_{\alpha,Y} \cdot P_1$.

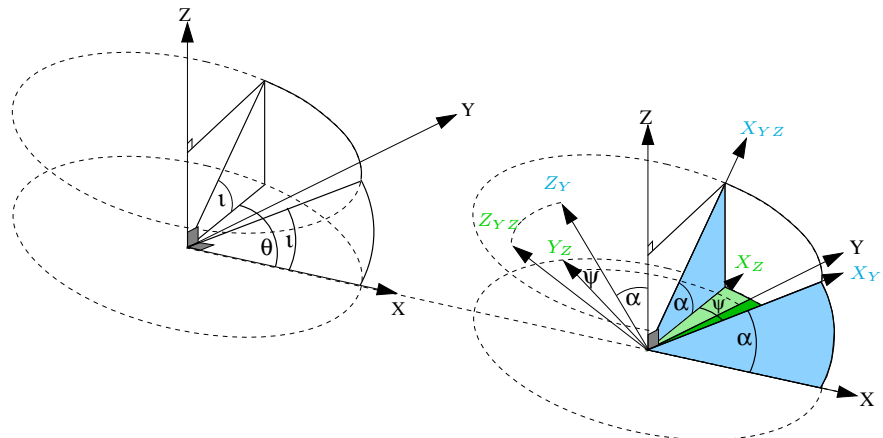
Figures 4.2a and 4.2b show the steps needed to assemble the local coordinate system, with Figure 4.2a duplicating the steps followed to arrive at the YZ rotation sequence followed in Section 3.5.2. This is followed by a translation through $P_{0 \rightarrow \text{CoM}} = \{R, 0, 0\}$ to transfer the local coordinate system to the inertial coordinate system. Figures 4.3a and 4.3b show the tether rotating around the inertial axes system – first through a rotation of ι around the inertial Y-axis, then a rotation of θ around the inertial Z-axis.

Figure	Rotational sequence
Figure 4.2a	$R_{\psi,Z} \cdot R_{\alpha,Y} \cdot P_1$
Figure 4.2b	$R+ R_{\psi,Z} \cdot R_{\alpha,Y} \cdot P_1$
Figure 4.3a	$R_{\iota,Y} \cdot (R+ R_{\psi,Z} \cdot R_{\alpha,Y} \cdot P_1)$
Figure 4.3b	$R_{\theta,Z} \cdot R_{\iota,Y} \cdot (R+ R_{\psi,Z} \cdot R_{\alpha,Y} \cdot P_1)$

Table 4.1: Reference table with figure and corresponding rotation

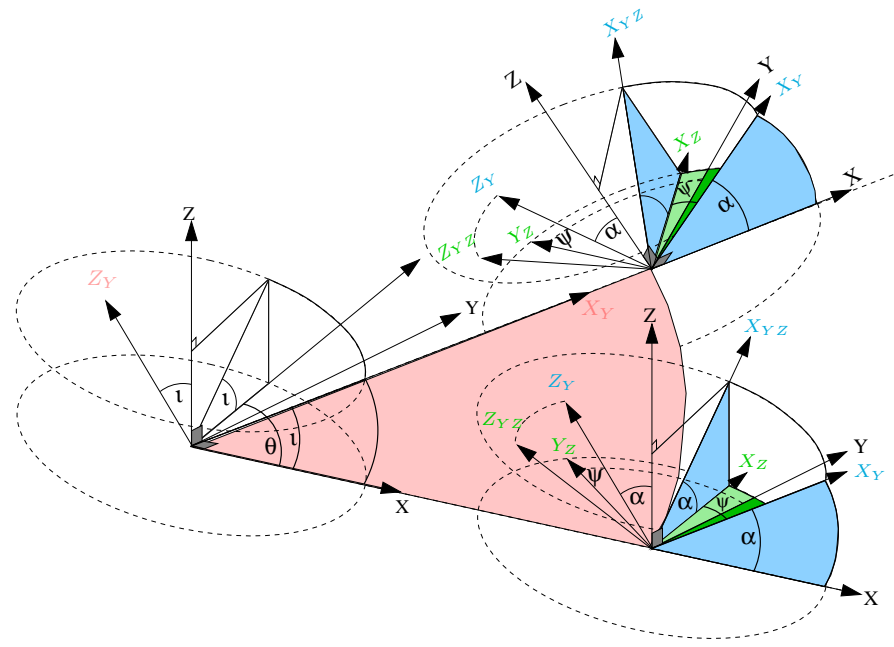


(a) YZ local rotation – $R_{\alpha, Y}$ then $R_{\psi, Z}$

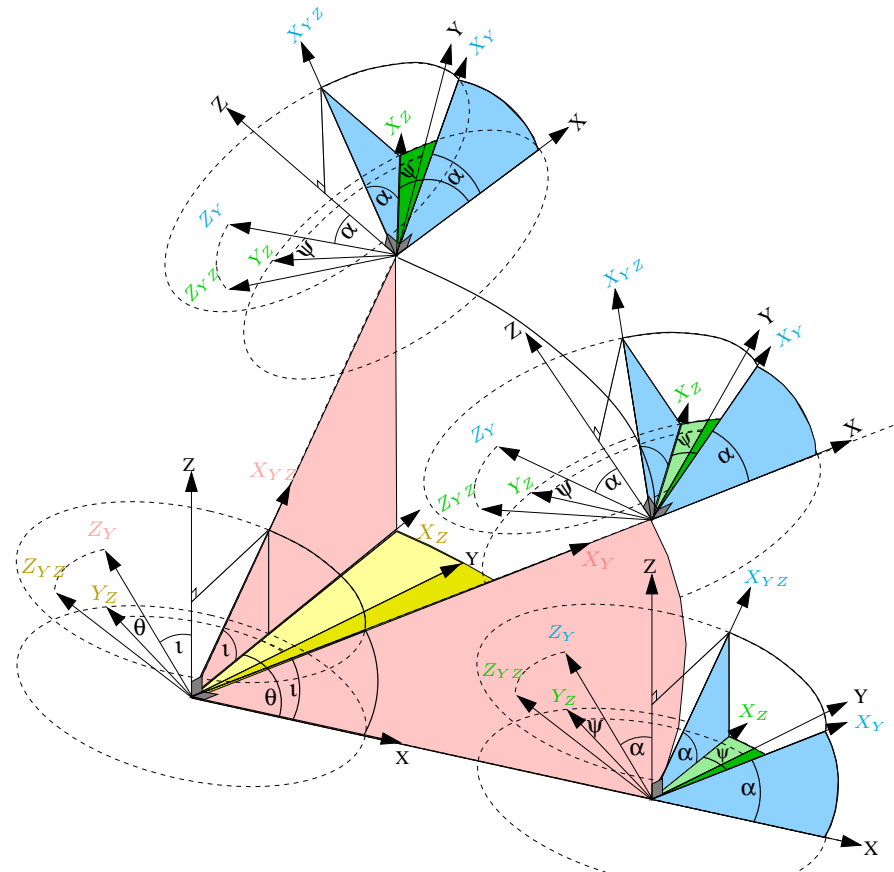


(b) Translation through R along X-axis

Figure 4.2: Rotation sequence for YZ rotation with inclination. α is shown as a negative rotation here for ease of visualisation.



(a) Y inertial rotation through angle ι – $R_{\iota,Y}$



(b) Z inertial rotation through angle θ – $R_{\theta,Z}$

Figure 4.3: Rotation sequence for YZ rotation with inclination. α and ι are shown as negative rotations here for ease of visualisation.

4.2.2 Lagrange's equations

Once the position of the mass points have been defined, the process of constructing the equations of motion will follow that outlined in Section 3.3.

As the equations form two separate groups, this will be examined separately: in Section 4.2.3 for the local system and Section 4.2.4 for the orbital system. The equations are combined and listed in Appendix A.

4.2.3 Lagrange's equations – local system

The mass points, as indicated earlier, are:

- the two payload masses, each a distance L from the facility mass and each with mass M_{payload}
- the two tethers with mass points each a distance $L/2$, halfway along the tether, each with mass M_{tether}
- the facility mass, M_{facility} .

The tether system is symmetrical; the in-plane angles will be defined as ψ and $-\psi$, while the out-of-plane angles will be defined as α and $-\alpha$ respectively.

As previously, the tethers are assumed to be rigid and inextensible to simplify the equations. The stator will not be included to simplify the equations. The masses of the payloads are assumed to be equal and the masses of the tethers are assumed to be equal such that:

$$M_{\text{payload}\ 1} = M_{\text{payload}\ 2} = M_{\text{payload}} \quad \text{and} \quad M_{\text{tether}\ 1} = M_{\text{tether}\ 2} = M_{\text{tether}}$$

The locations of each of the mass points in the inertial plane are therefore:

$$P_{\text{payload } 1} = R \begin{pmatrix} \cos \iota \cos \theta \\ \cos \iota \sin \theta \\ -\sin \iota \end{pmatrix} + L \begin{pmatrix} \cos \alpha(\cos \theta \cos \iota \cos \psi - \sin \theta \sin \psi) - \cos \theta \sin \alpha \sin \iota \\ \cos \alpha(\cos \iota \cos \psi \sin \theta + \cos \theta \sin \psi) - \sin \alpha \sin \theta \sin \iota \\ -\cos \iota \sin \alpha - \cos \alpha \cos \psi \sin \iota \end{pmatrix} \quad (4.6)$$

$$P_{\text{payload } 2} = R \begin{pmatrix} \cos \iota \cos \theta \\ \cos \iota \sin \theta \\ -\sin \iota \end{pmatrix} - L \begin{pmatrix} \cos \alpha(\cos \theta \cos \iota \cos \psi - \sin \theta \sin \psi) - \cos \theta \sin \alpha \sin \iota \\ \cos \alpha(\cos \iota \cos \psi \sin \theta + \cos \theta \sin \psi) - \sin \alpha \sin \theta \sin \iota \\ -\cos \iota \sin \alpha - \cos \alpha \cos \psi \sin \iota \end{pmatrix} \quad (4.7)$$

$$P_{\text{tether } 1} = R \begin{pmatrix} \cos \iota \cos \theta \\ \cos \iota \sin \theta \\ -\sin \iota \end{pmatrix} + \frac{L}{2} \begin{pmatrix} \cos \alpha(\cos \theta \cos \iota \cos \psi - \sin \theta \sin \psi) - \cos \theta \sin \alpha \sin \iota \\ \cos \alpha(\cos \iota \cos \psi \sin \theta + \cos \theta \sin \psi) - \sin \alpha \sin \theta \sin \iota \\ -\cos \iota \sin \alpha - \cos \alpha \cos \psi \sin \iota \end{pmatrix} \quad (4.8)$$

$$P_{\text{tether } 2} = R \begin{pmatrix} \cos \iota \cos \theta \\ \cos \iota \sin \theta \\ -\sin \iota \end{pmatrix} - \frac{L}{2} \begin{pmatrix} \cos \alpha(\cos \theta \cos \iota \cos \psi - \sin \theta \sin \psi) - \cos \theta \sin \alpha \sin \iota \\ \cos \alpha(\cos \iota \cos \psi \sin \theta + \cos \theta \sin \psi) - \sin \alpha \sin \theta \sin \iota \\ -\cos \iota \sin \alpha - \cos \alpha \cos \psi \sin \iota \end{pmatrix} \quad (4.9)$$

$$P_{\text{facility}} = R \begin{pmatrix} \cos \iota \cos \theta \\ \cos \iota \sin \theta \\ -\sin \iota \end{pmatrix} \quad (4.10)$$

The velocities of each of the mass points are then calculated. These are not listed here because of the length of the equations.

The five mass points are used to find the translational kinetic energy, T_{trans} , of the system:

$$\begin{aligned} T_{\text{trans}} = & \frac{M_{\text{payload } 1}}{2} V_{\text{payload } 1} \cdot V_{\text{payload } 1} + \frac{M_{\text{payload } 2}}{2} V_{\text{payload } 2} \cdot V_{\text{payload } 2} \\ & + \frac{M_{\text{tether } 1}}{2} V_{\text{tether } 1} \cdot V_{\text{tether } 1} + \frac{M_{\text{tether } 2}}{2} V_{\text{tether } 2} \cdot V_{\text{tether } 2} \\ & + \frac{1}{2} (M_{\text{payload } 1} + M_{\text{payload } 2} + M_{\text{tether } 1} + M_{\text{tether } 2} + M_{\text{facility}}) V_{\text{CoM}} \cdot V_{\text{CoM}} \end{aligned} \quad (4.11)$$

which evaluates to:

$$\begin{aligned}
T_{\text{trans}} = & \frac{1}{2} \left((\cos^2(\iota) \dot{\theta}^2 + \dot{\iota}^2) R^2 + \dot{R}^2 \right) (M_{\text{Facility}} + 2(M_{\text{payload}} + M_{\text{tether}})) + \\
& \frac{1}{64} L^2 \left(16\dot{\alpha}^2 + 32\dot{\theta} \sin(\iota) \sin(\psi) \dot{\alpha} - 4(-2 \cos(2\psi) \cos^2(\alpha) + \cos(2\alpha) - 3) \dot{\iota}^2 + \right. \\
& 16 \cos^2(\alpha) \dot{\psi}^2 + 16\dot{\theta}\dot{\psi} (2 \cos^2(\alpha) \cos(\iota) - \cos(\psi) \sin(2\alpha) \sin(\iota)) + \\
& \dot{\theta}^2 (-8 \cos^2(\alpha) \cos(2\psi) \sin^2(\iota) + 2 \cos(2\alpha) - 2 \cos(2\iota) + \\
& 3 \cos(2(\iota - \alpha)) + 3 \cos(2(\alpha + \iota)) - 8 \cos(\psi) \sin(2\alpha) \sin(2\iota) + 10) + \\
& \left. 16i \left(\dot{\theta} \sin(\iota) \sin(2\psi) \cos^2(\alpha) + 2 \cos(\psi) \dot{\alpha} + (\cos(\iota) \dot{\theta} + \dot{\psi}) \sin(2\alpha) \sin(\psi) \right) \right) \\
& (4M_{\text{payload}} + M_{\text{tether}}) \quad (4.12)
\end{aligned}$$

The rotational kinetic energy, T_{rot} , of the system is found in a similar way:

$$T_{\text{rot}} = (I_{\text{payload } 1} + I_{\text{payload } 2} + I_{\text{tether } 1} + I_{\text{tether } 2}) \cdot (\omega_{\text{local}} \cdot \omega_{\text{local}}) \quad (4.13)$$

where:

$$\omega_{\text{local}} = \begin{pmatrix} 0 \\ \dot{\alpha} \\ \dot{\psi} \end{pmatrix} \quad I_3 = \begin{pmatrix} 1 & 0 & 0 \\ 0 & 1 & 0 \\ 0 & 0 & 1 \end{pmatrix}$$

$$\begin{aligned}
I_{\text{payload } 1} &= L^2 M_{\text{payload } 1} \cdot I_3 & I_{\text{payload } 2} &= L^2 M_{\text{payload } 2} \cdot I_3 \\
I_{\text{tether } 1} &= \frac{1}{3} L^2 M_{\text{tether } 1} \cdot I_3 & I_{\text{tether } 2} &= \frac{1}{3} L^2 M_{\text{tether } 2} \cdot I_3
\end{aligned}$$

The evaluated sum of the component rotational kinetic energies are:

$$T_{\text{rot}} = \frac{1}{3} L^2 (3M_{\text{payload}} + M_{\text{tether}}) (\dot{\alpha}^2 + \dot{\psi}^2) \quad (4.14)$$

The sum of the potential energies, U , are:

$$U = \sum_{j=1}^n \frac{\mu m_j}{|P_j|} = \sum_{j=1}^n \frac{\mu m_j}{\sqrt{P_j \cdot P_j}} \quad (4.15)$$

where P_j are the magnitude of the mass point locations, given in Equations 4.6 to 4.10.

The full rotational sequence is not needed here, merely the distance between the two points, which leads to a simpler expression of the magnitude of the distance.

Taking Equation 4.2 as the start point, the distance (i.e., the magnitude) is:

$$\left| P_{\text{payload } 1} \right| = \left| R_{\theta, Z} \cdot R_{\iota, Y} \cdot (P_{0 \rightarrow \text{CoM}} + R_{\psi, Z} \cdot R_{\alpha, Y} \cdot P_1) \right| \quad (4.16)$$

$$\left| P_{\text{payload } 1} \right| = \left| R_{\theta, Z} \right| \cdot \left| R_{\iota, Y} \right| \cdot \left| P_{0 \rightarrow \text{CoM}} + R_{\psi, Z} \cdot R_{\alpha, Y} \cdot P_1 \right| \quad (4.17)$$

The magnitude of a purely rotational matrix is, by definition, equal to one:

$$\left| R_{\theta, Z} \right| = 1 \quad (4.18)$$

$$\left| R_{\iota, Y} \right| = 1 \quad (4.19)$$

This simplifies Equation 4.17 to:

$$\left| P_{\text{payload } 1} \right| = \left| P_{0 \rightarrow \text{CoM}} + R_{\psi, Z} \cdot R_{\alpha, Y} \cdot P_1 \right| \quad (4.20)$$

$$\left| P_{\text{payload } 1} \right| = \left| \begin{pmatrix} R \\ 0 \\ 0 \end{pmatrix} + \begin{pmatrix} L \cos \alpha \cos \psi \\ L \cos \alpha \sin \psi \\ -L \sin \alpha \end{pmatrix} \right| \quad (4.21)$$

$$P_{\text{payload } 1} = \sqrt{L^2 + 2 L R \cos \alpha \cos \psi + R^2} \quad (4.22)$$

The evaluated expression for the potential energy is therefore:

$$U = - \left(\frac{\mu M_{\text{facility}}}{R} \right) - \mu \left(\frac{1}{\sqrt{L^2 - L_{\text{med}} + R^2}} + \frac{1}{\sqrt{L^2 + L_{\text{med}} + R^2}} \right) M_{\text{payload}} \\ - 2\mu \left(\frac{1}{\sqrt{L^2 - 2L_{\text{med}} + 4R^2}} + \frac{1}{\sqrt{L^2 + 2L_{\text{med}} + 4R^2}} \right) M_{\text{tether}} \quad (4.23)$$

where:

$$L_{\text{med}} = 2LR \cos \alpha \cos \psi$$

The Lagrangian is then given by $\mathbb{L} = T - U$:

$$\mathbb{L} = T_{\text{trans}} + \frac{L^2 (3M_{\text{payload}} + M_{\text{tether}}) (\dot{\alpha}^2 + \dot{\psi}^2)}{3} \\ + \left(\frac{\mu M_{\text{facility}}}{R} \right) + \mu \left(\frac{1}{\sqrt{L^2 - L_{\text{med}} + R^2}} + \frac{1}{\sqrt{L^2 + L_{\text{med}} + R^2}} \right) M_{\text{payload}} \\ + 2\mu \left(\frac{1}{\sqrt{L^2 - 2L_{\text{med}} + 4R^2}} + \frac{1}{\sqrt{L^2 + 2L_{\text{med}} + 4R^2}} \right) M_{\text{tether}} \quad (4.24)$$

where T_{trans} is given by Equation 4.12.

Lagrange's equations are then generated for two out of the five generalised coordinates, $\{\psi, \alpha\}$ as follows:

$$\frac{d}{dt} \left(\frac{\partial T}{\partial \dot{q}_j} \right) - \frac{\partial T}{\partial q_j} + \frac{\partial U}{\partial q_j} = Q_j \quad (4.25)$$

and are provided in Appendix A along with the non-conservative forcing terms.

4.2.4 Lagrange's equations – global system

The global equations used to construct the motion of the facility around the Earth are now outlined. The mass for the system is summed and used as the total mass

located at the CoM:

$$M_{\text{total}} = 2M_{\text{payload}} + 2M_{\text{tether}} + M_{\text{facility}} \quad (4.26)$$

The locations of the single representative mass point in the inertial plane is therefore:

$$\mathbf{P}_{\text{orbit}} = \begin{pmatrix} R \cos \iota \cos \theta \\ R \cos \iota \sin \theta \\ -R \sin \iota \end{pmatrix} \quad (4.27)$$

The velocities of each of the mass points are then calculated⁴. Equation 4.28 shows the velocity of the system CoM:

$$\mathbf{V}_{\text{orbit}} = \begin{pmatrix} \dot{R} \cos \theta \cos \iota - R (\dot{\theta} \cos \iota \sin \theta + i \cos \theta \sin \iota) \\ R \dot{\theta} \cos \theta \cos \iota + \sin \theta (\dot{R} \cos \iota - R i \sin \iota) \\ -R i \cos \iota - \dot{R} \sin \iota \end{pmatrix} \quad (4.28)$$

The single mass point is used to find the translational kinetic energy, T_{trans} , of the system:

$$T_{\text{trans}} = \frac{M_{\text{total}}}{2} (\mathbf{V}_{\text{orbit}} \cdot \mathbf{V}_{\text{orbit}}) \quad (4.29)$$

$$T_{\text{trans}} = \frac{M_{\text{total}}}{2} \left((\dot{\theta}^2 \cos^2(\iota) + i^2) R^2 + \dot{R}^2 \right) \quad (4.30)$$

The rotational kinetic energy is assumed to be zero:

$$T_{\text{rot}} = 0 \quad (4.31)$$

⁴Note: as the inclination term is given the symbol iota, ι , the first derivative of the inclination term, ι , is i , and not the ninth letter of the Latin alphabet, i.

The expression for potential energy, U , is simply:

$$U = \frac{\mu M_{\text{total}}}{|R.R|} = \frac{\mu M_{\text{total}}}{R} \quad (4.32)$$

as the distance to the CoM is defined as R .

The Lagrangian is then given by $\mathbb{L} = T - U$:

$$\mathbb{L} = \frac{M_{\text{total}}}{2} \left(\left(\dot{\theta}^2 \cos^2(\iota) + \dot{\iota}^2 \right) R^2 + \dot{R}^2 \right) - \frac{\mu M_{\text{total}}}{R} \quad (4.33)$$

Lagrange's equations are then generated for three out of the five generalised coordinates, $\{R, \theta, \iota\}$ as follows:

$$\frac{d}{dt} \left(\frac{\partial T}{\partial \dot{q}_j} \right) - \frac{\partial T}{\partial q_j} + \frac{\partial U}{\partial q_j} = Q_j \quad (4.34)$$

and are provided in Appendix A along with the non-conservative forcing terms.

4.2.5 Non-conservative forces

The MMET system requires that a force be transferred from the motor to the tether arms to ‘spin-up’ the system. The mechanics of spin-up of such a system is non-trivial, especially when flexural⁵ terms and inertial terms are taken into account. The spin-up dynamics of length deployment is covered in Chapter 5.

The tether arms are assumed to be rigid and symmetrical at all times, limiting the payload tethers to a planar disc. The motor torque is assumed to act in the same plane as this disc. The stator arms are neglected.

The motor torque will exert a large power drain, therefore all the power for the motor will be derived from the solar arrays harnessing a free, plentiful and renewable source of energy. The Forcing term in Lagrange's equations must reflect the binary

⁵Flexural terms are not included in the analysis due to the complexities they introduce.

nature of the availability of the power supply. The **Eclipse** function modulates the motor torque to take into account the eclipsing of the Sun by the Earth, reducing the torque to $\tau = 0$ when in darkness and taking the default $\tau = \tau_{\max}$ when in sunlight.

Eclipse is the binary function:

$$\text{Eclipse} = \begin{cases} 1 & \left\{ \begin{array}{l} R^2(1 - \cos^2(\iota) \cos^2(\theta)) \leq R_{\text{Earth}}^2 \left(1 + \frac{R \cos \theta}{R_{\text{Sun}}}\right)^2 \\ \text{AND} \\ \cos \iota \cos \theta > 0 \end{array} \right. \\ 0 & \left\{ \text{otherwise} \right. \end{cases} \quad (4.35)$$

The radius of the Earth's shadow is scaled from R_{Earth} by the factor $\frac{R_{\text{Sun}} + R \cos \theta}{R_{\text{Sun}}}$ as shown in Figure 4.4. The hypotenuse of the Y- and Z-component of the CoM at a time, t , in the orbit path is calculated and checked. If it is less than the shadow distance, then the CoM is in shadow.

$$\begin{aligned} R_{\text{Shadow}} &= R_{\text{Earth}} \left(\frac{R_{\text{Sun}} + R \cos \theta}{R_{\text{Sun}}} \right) \\ R_{\text{Shadow}} &= R_{\text{Earth}} \left(1 + \frac{R \cos \theta}{R_{\text{Sun}}} \right) \end{aligned} \quad (4.36)$$

$$\begin{aligned} Y_{\text{CoM inertial}}^2 + Z_{\text{CoM inertial}}^2 &= (R \cos \iota \sin \theta)^2 + (R \sin \iota)^2 \\ &= R^2 (1 - \cos^2(\iota) \cos^2(\theta)) \end{aligned} \quad (4.37)$$

Hence, the eclipse checking function is calculated as:

$$R^2 (1 - \cos^2(\iota) \cos^2(\theta)) \leq R_{\text{Earth}}^2 \left(1 + \frac{R \cos(\theta)}{R_{\text{Sun}}} \right)^2 \quad (4.38)$$

which gives two eclipses an orbit, therefore an additional constraint is added to

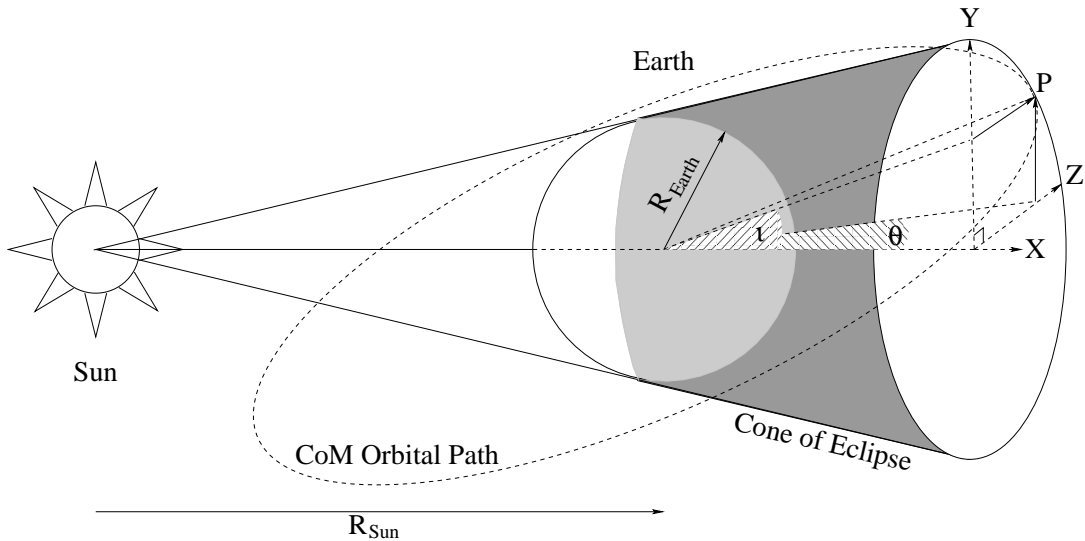


Figure 4.4: Eclipse checking function (not to scale)

ensure that the CoM is eclipsed only once per orbit:

$$\cos \iota \cos \theta > 0 \quad (4.39)$$

A diagram of the distances on-orbit is shown in Figure 4.4 and the Mathematica output for a 29° orbit is shown in Figure 4.5. The Sun is assumed to be a point source and the Earth is assumed to describe a circular orbit around the sun.

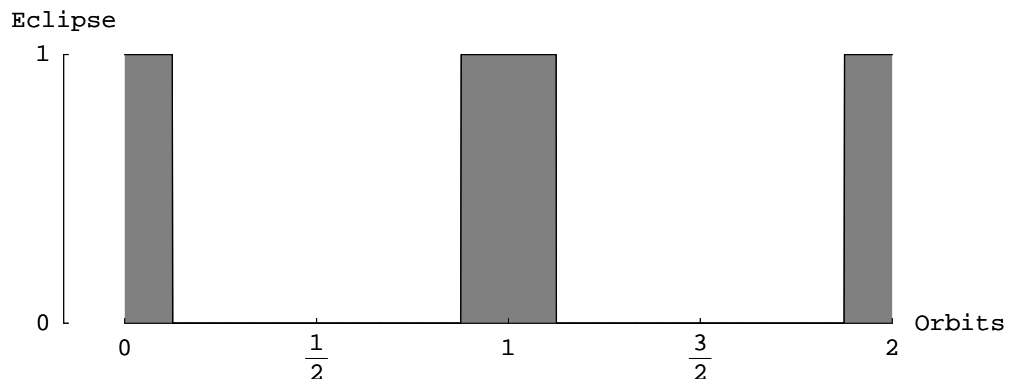


Figure 4.5: Sample plot of the Eclipse function in Mathematica

4.3 Analysis of tether on an inclined orbit

The generated equations are solved with Mathematica's general purpose solver `NDSolve[...]` with the following parameters:

```
AccuracyGoal      -> Automatic
PrecisionGoal     -> Automatic
WorkingPrecision  -> 20
```

To fully understand the interaction between the local and inertial systems, Lagrange's equations are solved with different initial conditions or 'cases'. These are given in Table 4.2.

case	i	$\dot{\psi}$	$\dot{\alpha}$	ι	ψ	α	eccent	τ
I1	0	0	0	0	0	0	0	1000
I2	0	0	0	$29\pi/180$	0	0	0	1000
I3	0	1	0	$29\pi/180$	0	0	0	1000
I4	0	0	0	$29\pi/180$	0	$-29\pi/180$	0	1000
I5	0	1	0	$29\pi/180$	0	$-29\pi/180$	0	1000

Table 4.2: Initial conditions for the inclination numerical solutions.

Case I1 gives a baseline in the inertial plane: no inclination, no out-of-plane spin and no initial in-plane spin. Case I2 introduces inclination, while case I3 has an inclined orbit with a significant initial in-plane spin. Cases I4 and I5 are comparable to cases I2 and I3, with the difference of an out-of-plane spin equal to the inclination (i.e. so the spin-plane is coincidental with the inertial plane).

All five cases have an equal torque level to enable a fair comparison.

The initial conditions⁶ for the other parameters held constant are:

$$L = 1000 \text{ m}, M_{\text{payload}} = 10 \text{ kg}, M_{\text{tether}} = 100 \text{ kg}, M_{\text{facility}} = 500 \text{ kg}, e = 0,$$

$$\dot{R}[0] = 0, \dot{\theta}[0] = 0.00113905 \text{ rad/s}, \theta[0] = 0, R[0] = 7.378 * 10^6 \text{ m}$$

⁶Note: the inclination term is represented by the Greek letter iota – ι – therefore the first derivative with respect to time is iota dot – i – and the second derivative iota dot dot – \ddot{i} . This was defined in order to remove the confusion between i dot and iota dot – \dot{i} .

Figures 4.11 to 4.18 show the solution to the equations of motion for 10 orbits over 63069.5 seconds where:

- Figure 4.11 shows plots of α vs. time
- Figure 4.12 shows plots of $\dot{\alpha}$ vs. time
- Figure 4.13 shows plots of α vs. ι
- Figure 4.14 shows 3D phase plots of ψ
- Figure 4.15 shows 3D phase plots of α
- Figure 4.16 shows plots of ΔV vs. time
- Figure 4.17 shows plots of tension vs. time
- Figure 4.18 shows plots of stress vs. time

4.3.0.1 Behaviour of R , θ and ι with time

The orbital parameters R , θ and ι are shown in Figure 4.10. They are deliberately chosen so that the orbital parameters are independent from the local parameters, as such the MMET does not influence any of these generalised coordinates.

Together, the three generalised coordinates R , θ and ι describe a circular orbit in the inertial plane in case I1 and a circular inclined orbit in cases I2 to I5.

4.3.0.2 Behaviour of α with time

Figures 4.11a to 4.11e demonstrate the α vs. time behaviour of the system. Clearly, the baseline case I1 shows there is no interaction between the inclination and out-of-plane coordinates when both are initially zero.

Comparing Cases I2 and I3 in Figures 4.11b and 4.11c gives an idea of the relative stabilising influence of the in-plane spin velocity, $\dot{\psi}$. It is the gyroscopic action of the in-plane spin that limits the out-of-plane coordinate, α .

The opposite appears to be true when Figures 4.11d and 4.11e – cases I4 and I5

– are compared. The out-of-plane spin angle is set such that the local system is aligned with the inertial plane. When this is accelerated from zero velocity initially, the out-of-plane angle returns to be coplanar with the inclination orbit⁷, with a small nutation of ($0.1 \text{ rad} \approx 6^\circ$). When started from a large initial in-plane velocity in the inertial plane, the opposite is true – it remains spinning in the inertial plane with a small adjustment towards the orbital plane.

4.3.0.3 Behaviour of $\dot{\alpha}$ with time

Figures 4.12a to 4.12e demonstrate the $\dot{\alpha}$ vs. time behaviour of the system. As previously, the baseline case I1 shows there is no interaction between the inclination and out-of-plane coordinates when both are initially zero.

Case I2 and I4 show the angular rate increasing from zero – this is larger than desired for operating the MMET, especially in the early start-up regime. However, case I3 shows that the greater the in-plane spin velocity, the lower the out-of-plane nutation.

4.3.0.4 Behaviour of α with ι

Figures 4.13a to 4.13e show the $\dot{\alpha}$ vs. ι interaction of the system.

The graphs here are inconclusive. There is a large interplay between α and ι in cases I3 and I5, where the in-plane velocity $\dot{\psi}$ is large, and a correspondingly smaller relationship between the two in cases I2 and I4 where the $\dot{\psi}$ term is zero. This, however, does not point to any concrete notions of interdependence.

Case I4 clearly shows the progression of α from a large out-of-plane motion (starting in the bottom right of the graph) to a smaller angle as the in-plane velocity increases.

⁷The inclination orbit is the orbital plane, offset $29\pi/180 \text{ rad}$ from the inertial plane.

4.3.0.5 Behaviour of ψ , $\dot{\psi}$, $\ddot{\psi}$

The eclipse functionality is clearly shown in the ψ phase plots in Figures 4.14a to 4.14e and the plot of ΔV in Figure 4.16a to 4.16e.

The ψ phase plane plots illustrate the shadow periods of the graph where the in-plane angular acceleration $\ddot{\psi}$, shown in the horizontal axis, is approximately zero compared to the illuminated periods where the tether is accelerated by the motor.

The plots of ΔV highlight the end result of the work done by the motor – the ΔV the system can impart to the payload. In this case, a ΔV of approximately 400 m/s is attained for a modest acceleration period of 17.5 hours.

In cases I1 and I3, the out-of-plane coordinate α is zero and the rate of increase in $\dot{\psi}$ is highest. The greater the out-of-plane spin angle, the less energy is available to transfer into increasing the (useful) in-plane spin rate.

Cases I4 and I5 show the more disordered plots when the out-of-plane coordinate is non-zero. Clearly, having a clean acceleration profile is advantageous from a stress-minimisation point of view – these profiles have a spin-up phase that feature a large $\dot{\alpha}$ term, which is difficult to aim when the payload must be released.

Similarly, case I2 does not have a clean spin-up phase when compared to case I1. This is purely due to the large out-of-plane motion that interferes with the in-plane spin.

4.3.0.6 Behaviour of α , $\dot{\alpha}$, $\ddot{\alpha}$

The α phase plane behaviour of the system is shown in Figures 4.15a to 4.15e. In case I3 – high $\dot{\psi}$ and the out-of-plane initial angle, α , set to zero – the out of plane velocity is minimised. Marginally larger out-of-plane angular velocities and accelerations are shown by case I4: zero initial $\dot{\psi}$ and the out-of-plane initial angle set to coincide with the inertial plane.

4.3.0.7 Behaviour of ΔV with time

The ΔV vs. time behaviour of the system is shown in Figures 4.16a to 4.16e.

The calculation of ΔV is straightforward, it is the product of the tether length and the angular velocity. The maximum useful ΔV is obtained when the out-of-plane angle is zero, and is analysed in Section 4.4. In this case, the maximum useful ΔV is simply the product of length and angular speed:

$$\Delta V = L \dot{\psi} \quad (4.40)$$

As the graphs of ΔV show the magnitude of the resultant velocity, cases I1 I2 and I4 should be almost identical, and cases I3 and I5 should also be identical. Whereas the former is true, case I5 has a useful velocity that is lower than expected. This is caused by rapid changes in the out-of-plane velocity $\dot{\alpha}$, which detracts from the in-plane spin velocity, $\dot{\psi}$.

4.3.0.8 Behaviour of tension with time

The tension profile of the tether is shown in Figures 4.17a to 4.17e.

The cases with zero initial in-plane spin – cases I1, I2 and I4 – exhibit similar levels of tension in the tether, approximately 10 kN. The tension appears to be slightly lower in the baseline case I1, however, this may be due to the larger out-of-plane movements in cases I2 and I4.

The remaining cases I3 and I5 start with a higher tension due to their large initial in-plane spin rate. Similarly to the ΔV plot in Figure 4.16e, the tension in case I5 rapidly fluctuates due to the large out-of-plane angular motions.

4.3.0.9 Behaviour of stress with time

The stress profile of the tether is shown in Figures 4.18a to 4.18e.

The graphs here are very similar to the tension graphs, as stress is equal to tension divided by the cross-sectional area, 0.000064 m^2 (equal to an 8 mm square section of tether).

4.3.1 Analysis of tension and stress in tether

The tension in the tether ignores any out-of-plane motion of the tether, as it was shown that the out-of-plane motion is not significant for small deviations from the spin-plane.

The tension in the tether is calculated as:

$$T_{\text{payload}} = M_{\text{payload}} \dot{\psi}^2 L_{\text{payload}} + \rho A \dot{\psi}^2 \frac{L_{\text{payload}}}{2} \quad (4.41)$$

with the first term as the tension due to the payload, the second term as the tension due to mass of the tether itself. The second term dominates in this case, as the mass of the tether is an order of magnitude higher than the mass of the payload.

The stress in the tether is calculated as:

$$\sigma = \frac{T_{\text{payload}}}{A} \quad (4.42)$$

The maximum allowable stress in the tether is calculated using the Ultimate Tensile Stress (for Zylon, the UTS is $5.9 * 10^9 \text{ N/m}^2$) and a Safety Factor (SF=1.5) as:

$$\sigma_{\max} = \frac{\sigma}{\text{SF}} = \frac{5.9 * 10^9}{1.5} = 3.933 \text{ GPa} \quad (4.43)$$

The variables are defined as:

$$M_{\text{payload}} = 10 \text{ kg}, L = 1000 \text{ m}, \rho = 1570 \text{ kg/m}^3, A = 0.000064 \text{ m}^2$$

using values of the tether⁸ composed of Zylon™ fibres with properties from Table D.1,

⁸The area is equivalent to a rectangular extrusion of 0.008 m .

Appendix D.

The maximum allowable stress gives an absolute ceiling to the stresses in the tether. This maximum stress, working backwards through the tension, is dependant on the in-plane velocity assuming the material and geometric properties of the system do not change when it is in-orbit. This interplay between $\dot{\psi}$ and $L_{payload}$ drives the maximum ΔV and therefore the entire feasibility of the system.

4.4 Tether release aiming

The criteria to maximise the ΔV when using the motorised tether with a Hohmann two-burn trajectory are as follows.

The tether will gain the most velocity from the release if the velocity vector is at right-angles to the orbital plane⁹. This is generally satisfied when the tether arm is aligned with the radius vector, a criteria of $\psi \approx 0$ and $\alpha \approx 0$

An excellent treatment of the sensitivity to errors in transfer orbits for Hohmann transfers is given in [Kamel and Soliman, 2006]. This may be directly applied to tethers for the same type of manoeuvres. For example, a 0.1% error in ΔV may give up to a 5% error in radius and semi-major axis. A thorough treatment of the errors due to an early or late release is needed for the tether.

In terms of release strategy for an inclined orbit, this criteria for release is generally only satisfied at one point in the cycle when the inclined orbital plane cuts the inertial plane, the direction is determined from the classical Hohmann trajectory, as in [McLaughlin, 2000].

An alternative to the Hohmann trajectory is the WSB method, which has been described in the literature: [Belbruno, 1987], [Miller and Belbruno, 1991] and [Koon

⁹This assumes that the mission is to provide the maximum ΔV ; many alternative tether missions exist, including a inclination change using a tether releasing the payload at an angle to the orbital plane.

et al., 2001]. To summarise, the WSB utilises the gravitational interaction of the Earth-Sun-Moon system to lower the ΔV required to capture a satellite in Lunar orbit. The WSB can be thought of as two Circular Restricted 3 Body Problems (CR3BP) patched together with a small correction burn of less than 25 m/s at the boundary between the Sun-Earth system and the Earth-Moon system.

A patch point is located by integrating forward the dynamics of the spacecraft in the Earth-Moon system from the patch point until the spacecraft is ballistically captured in Lunar orbit, and simultaneously integrating backward the dynamics of the spacecraft in the Sun-Earth system until the spacecraft links up with a LEO orbit around the Earth. Thus a patch point is found along with two halves of the trajectory from LEO to ballistic capture in Lunar orbit via the patch point.

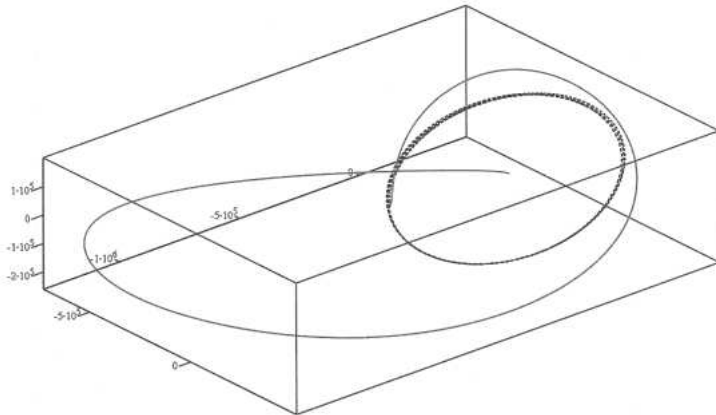


Figure 4.6: Diagram showing an example of the WSB trajectory, from ESA Bulletin 103: [Biesbroek and Janin, 2000]

Timing the release of the tether payload to launch on a WSB transfer is a difficult computational puzzle, but one which may be solved by optimising a numerical solution to the equations of motion. A trajectory is planned for a future time and the tether mission must provide a ΔV precisely with a very small margin of error in release angle.

The useful tip velocity (ΔV) will be approximately equal to the local body-centred

velocity of the tip payload. The local velocity is given in Equation 4.44 below:

$$V_{\text{payload } 1} = \begin{pmatrix} -L \sin(\alpha) \cos(\psi) \dot{\alpha} & -L \cos(\alpha) \sin(\psi) \dot{\psi} \\ -L \sin(\alpha) \sin(\psi) \dot{\alpha} & +L \cos(\alpha) \cos(\psi) \dot{\psi} \\ -L \cos(\alpha) \dot{\alpha} \end{pmatrix} \quad (4.44)$$

This reduces to the simple one-dimensional angular velocity when considering the optimal release case of a perfectly aligned tether of $\psi \rightarrow 0$, $\alpha \rightarrow 0$ and $\dot{\alpha} \rightarrow 0$:

$$V_{\text{payload } 1} \rightarrow \begin{pmatrix} 0 \\ L \dot{\psi} \\ 0 \end{pmatrix} \quad (4.45)$$

The major long-term perturbations such as J2, Lunar and Solar gravity etc. are not covered here as they do not affect the short-term dynamics of tether spin-up. [Parsons, 2006] covers some of these alongside the WSB trajectories.

4.4.1 Tether error analysis

Small changes in the tether variables could have a large effect on the performance of the tether, therefore it is important to quantify these for the purposes of risk mitigation. An analysis was performed to quantify the effects that a small change in the system parameters have on the payload apogee and inclination, when calculated at the orbital location directly opposite the separation point¹⁰.

The Figures 4.7 and 4.8 are calculated by solution of the equations of motion for MMET tether system with two payloads, with the default initial conditions:

$$\begin{aligned} L_{\text{pay}} &= 1000 \text{ m}, M_{\text{pay}} = 10 \text{ kg}, M_{\text{tether}} = 100 \text{ kg}, M_{\text{hub}} = 500 \text{ kg}, e = 0, \\ i[0] &= 0 \text{ rad/s}, \dot{\psi}[0] = 0.1 \text{ rad/s}, \dot{\alpha}[0] = 0 \text{ rad/s}, \dot{R}[0] = 0 \text{ m/s}, \end{aligned}$$

¹⁰Calculated as π radians round the orbit from the system centre of mass point when the payload is separated from the tether.

$\dot{\theta}[0] = 0.00113905 \text{ rad/s}$, $\iota[0] = 29\pi/180 \text{ rad}$, $\psi[0] = 0 \text{ rad}$, $\alpha[0] = 0 \text{ rad}$,
 $R[0] = 0 \text{ m}$, $\theta[0] = 0 \text{ rad}$, Torque = 1000 Nm,
Nominal Orbital Period = 6306.95 s.

The initial conditions above equate to an equivalent ΔV of 100 m/s.

The payload is released when the tether is aligned with the radius vector ($\psi = 0$ and $\alpha = 0$) and follows a ballistic trajectory thereafter. No allowance is made here for angular momentum effects between the payload and tether system on release.

Errors are simulated by the addition of small offsets in the initial conditions at the release point. The effect that the errors have on that variable is analysed by comparing the apogee and the inclination to the unperturbed values measured at the apogee point. The starting radius¹¹ is 7,378,000 m. With the default initial conditions above, the apogee is 7,747,377 m, a difference of 369,377 m or approximately 5% of the radius vector. In terms of altitude, the starting altitude is 100,000 m and the apogee when the payload is released is 469,377 m. The inclination of the apogee point is equal to the magnitude of the perigee inclination of 29°.

Figure 4.7a shows the effect that a small change in radius has on the tether apogee. A change in radius of 1000 m at the tether release point corresponds to a 7460 m increase in the apogee of the payload. The difference of the apogee is higher than the expected first order approximation of $7\Delta L$ as suggested¹² in [Ziegler and Cartmell, 2001] by 460 m, the higher calculated number is a result of the ΔV supplied by the rotating tether.

The change in apogee due to small changes in inclination is shown in Figure 4.7b. It follows from orbital mechanics that a small change in the inclination to flatten the orbit will increase the apogee.

A small change in the in-plane rotation angle, ψ , causes minor changes to the apogee altitude, as shown in Figure 4.7c. The relationship is predominantly parabolic

¹¹That is, the perigee point.

¹²For a hanging tether.

based due to the increase in energy supplied to the orbit $\frac{1}{2}m\Delta V^2$, which is itself dependent on $\dot{\psi}$.

4.4.2 Lunar capture

Once the spacecraft is ballistically captured around the Moon, a small thrust is required to ensure that the orbital energy is reduced below the threshold required for the spacecraft to escape. A ΔV of less than 50 m/s will fix the spacecraft in a highly elliptical ($e = 0.9$) but stable Lunar orbit.

A midpoint burn of $\Delta V = 25 \text{ m/s}$ with a capture burn of $\Delta V = 50 \text{ m/s}$ corresponds to a fuel mass fraction of 9.6% assuming an I_{sp} rating of 75 s for a Nitrogen cold gas thruster. A conservative estimate of 1 kg mass for the engine and associated structure leaves the 10 kg original satellite mass with 8.04 kg of useful payload mass.

When this is compared to the Hohmann transfer ΔV cost, [Koon et al., 2001, p71] calculates that the WSB transfer requires 20% less fuel to execute. This necessarily transfers into a lower mass of the payload and subsequent cost savings.

Once the payload is captured, it is possible to use tethers for the descent to the Lunar surface. Staged tethers as in [Cartmell et al., 2004] or Lunar elevators may be used to transfer the payload to the surface, and Lunar minerals to LEO. [Williams et al., 2005, p 784] claims that the payload can be delivered within 1 cm for a controlled handover of a staged tether system, and can be held in a 10 m window for approximately 135 seconds, which is ideal for the multi-staged tether system provided a control system can be devised that will enable an automatic remote handover of payloads.

4.5 A demonstration Lunar mission with a tether launch

A demonstration mission to the Moon is outlined below, involving a tether launch from LEO to Lunar parking orbit. It is examined using hardware available in 2008, as a low-cost micro-satellite mission that could be launched in the short term, with today's technology.

4.5.1 Spacecraft sizing

The MMET system is sized to launch a 10 kg payload to Lunar capture orbit. This is intended as a demonstration level mission, although the MMET system may be scaled to launch larger payloads, as discussed previously.

The facility is proposed to be entirely housed within a cylinder containing the motor and gearbox. The solar arrays will consist of 35000 standard sized $2\text{ cm} \times 4\text{ cm}$ solar cells, which provide the power required by the motor, recharge the batteries and provide power to the spacecraft bus. The solar cells will be a *InGaP/GaAs/Ge* type capable of 25% efficiency [Green et al., 2003], with a degradation rate of $1\%/\text{year}$ [Griffin and French, 1991]. The mission length of 5 years is based on the probability of a tether cut due to orbital debris when using multiple redundant tether strands, coupled with the useful life of the solar arrays.

The power to the motor will only be available during the time the facility is not in eclipse and this is factored into the equations using the function **Eclipse** described in Section 4.2.5.

The total useful power available for a $2\text{ m} \times 3\text{ m}$ cylinder augmented by a $1.5\text{ m} \times 6\text{ m}$ fold out panel will be 4.3 kW when launched and 3.05 kW at the end of a 5 year mission. The end of life power allows the motor characteristics to be defined, in this case the motor used will be a 3 kW rated motor capable of driving 1000 Nm

of torque through a reducing gearbox. The gearbox will reduce the rotations from the motor armature rotation of $430\ rad/s$ to the required angular velocity of the rotor arm of $20\ rad/s$. This motor is based around GE Industrial DC motor model 5BC49JB1115, rated at $4\ hp$ and $4150\ RPM$, which is designed to drive an electric vehicle.

The rotor is comprised of two $1\ km$ tether sections with each linking the facility to the payloads. The stator is identical, with the payloads replaced by counterweights. The tether itself is ZylonTM fibre with a tensile strength of $5.8\ GPa$, density of $1570\ kg/m^3$ and cross sectional area of $64\ mm^2$. This leads to a tether mass of $100\ kg$ for each of the four tether lines, totalling $400\ kg$. A safety factor of 1.3 is applied to the calculation of the maximum breaking stress, however additional precautions must be taken by careful design of the tether structure to ensure the tether will remain intact if impacted by micro-meteorites or debris [Forward and Hoyt, July 1995].

The tether mass outweighs the payload mass in order to keep the breaking stress to a manageable level. This is advantageous as the tethers may be adjusted to compensate for any tether failure mode or asymmetric payload release.

The MMET is designed to be highly reusable. The 5 day spin up cycle must be matched by an equal 5 day spin down cycle to return the rotor to a stationary position aligned with the gravity vector. When this is achieved, the payload will be much easier to dock than when in motion. For the WSB transfer, payloads can be transferred to the Moon every Lunar month, leaving a window of 20 days to dock the payloads to the tethers.

4.5.2 Analysis

The square of the characteristic velocity, U_{vel} , of the tether is proportional to the tensile strength, T , and inversely proportional to the density, ρ :

$$U_{\text{vel}} = \sqrt{\frac{2T}{\rho}} \quad (4.46)$$

The characteristic velocity determines the maximum velocity attainable for a tether supporting its own mass while rotating. Adding a payload limits the velocity a tether can impart by increasing the tension and stress in the tether, therefore by keeping the mass of the payload to a fraction of the tether's mass, the decrease in characteristic velocity is minimised.

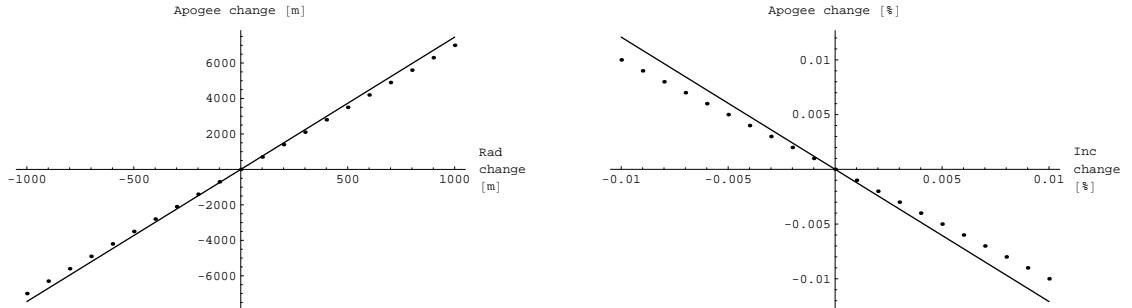
A tether manufactured from Zylon™ with $T = 5.9 \text{ GPa}$, $\rho = 1570 \text{ kg/m}^3$ with a safety factor of 1.3 gives a characteristic velocity of 2.238 km/s . With a payload mass equivalent to 10% of the tether mass attached to the end of the tether, the characteristic velocity will drop by approximately 10% to 2.10 km/s . To achieve Lunar orbit, the payload will need 3.187 km/s [Sweetster, 1991] from LEO at 167 km altitude. Therefore, the tether will have to occupy a higher earth orbit of 1000 km to successfully launch to the moon, or a staged system will be required [Cartmell et al., 2004].

The necessary orbital altitude of 1000 km is unfortunate in terms of the orbital debris that the tether will encounter. Figure 4.9 shows the debris environment from LEO to Geostationary Earth Orbit (GEO) – the debris environment is relatively dense until 3000 km altitude, meaning the risk of a severed tether is higher in this region of space. This is compounded by the long time to clear the debris from the higher orbits, meaning the orbital debris will continue to pose problems for decades to come.

4.6 Conclusions

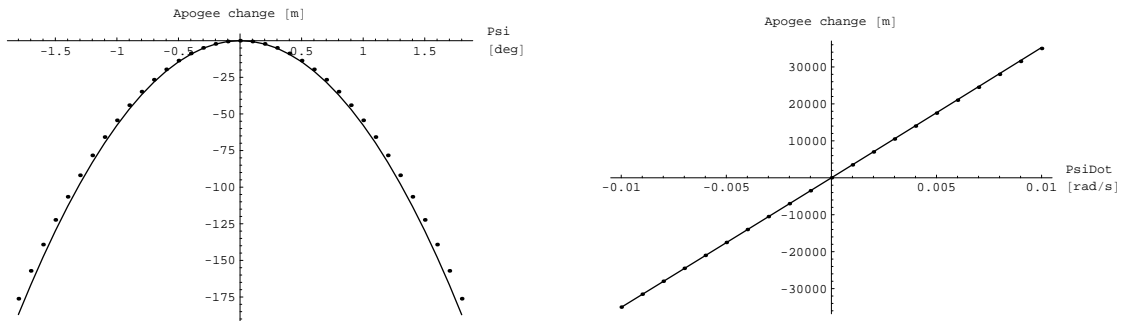
A demonstration mission launching a micro-satellite from MEO to Lunar orbit is achievable using current technology. The safety margins, however, are extremely small and the MMET launcher would be located in an orbit with large amounts of debris.

The inclination term does not significantly alter the dynamics of the MMET system. However, any out-of-plane component in the local axes – whether on an inclined orbit or not – interacts with the orbital parameters to create an unsteady oscillation in the tether. This is unacceptable for payload aiming and release, therefore the local out-of-plane angle should be minimised insofar as possible.



(a) Payload apogee change (m) vs. change in radius (m). Solid line – calculated results, dotted line – linear relationship $\Delta\text{Apogee} = 7 * \Delta R$

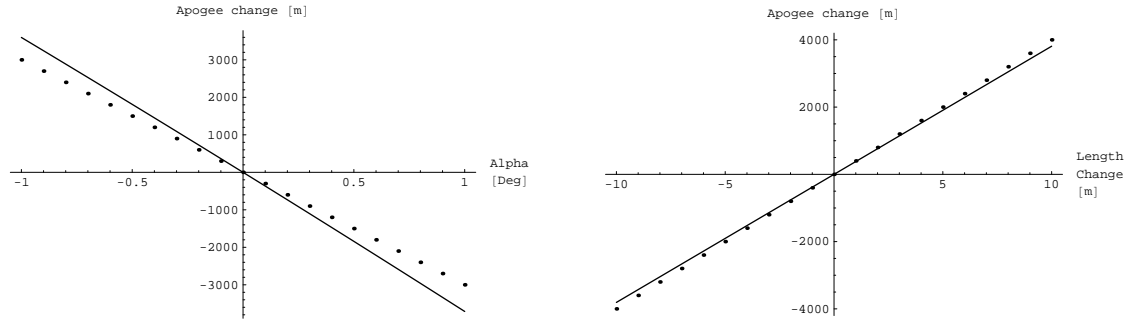
(b) Payload apogee change (%) vs. change in inclination (%). Solid line – calculated results, dotted line – linear relationship $\Delta\text{Apogee} = -1 * \Delta i$



(c) Payload apogee change (m) vs. change in ψ (deg). Solid line – calculated results, dotted line – trigonometric relationship $\Delta\text{Apogee} = ((\Delta\psi))^2 * -60$

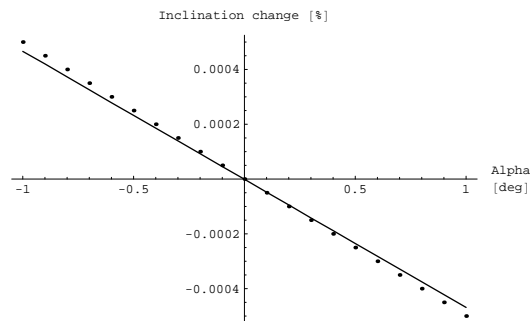
(d) Payload apogee change (m) vs. change in $\dot{\psi}$ (rad/s). Solid line – calculated results, dotted line – linear relationship $\Delta\text{Apogee} = 3500000 * \Delta\dot{\psi}$

Figure 4.7: Change in apogee of the payload after release from the tether system after one half of an orbit compared to small changes of system parameters



(a) Payload apogee change (m) vs. change in α (deg). Solid line – calculated results, dotted line – linear relationship $\Delta\text{Apogee} = -3000 * \Delta\alpha$

(b) Payload apogee change (m) vs. change in length (m). Solid line – calculated results, dotted line – linear relationship $\Delta\text{Apogee} = 400\Delta L$



(c) Payload inclination change (%) vs. change in α (deg). Solid line – calculated results, dotted line – linear relationship $\Delta\iota = -\frac{1}{2000}\Delta\alpha$

Figure 4.8: Change in apogee and inclination of the payload after release from the tether system after one half of an orbit compared to small changes of system parameters

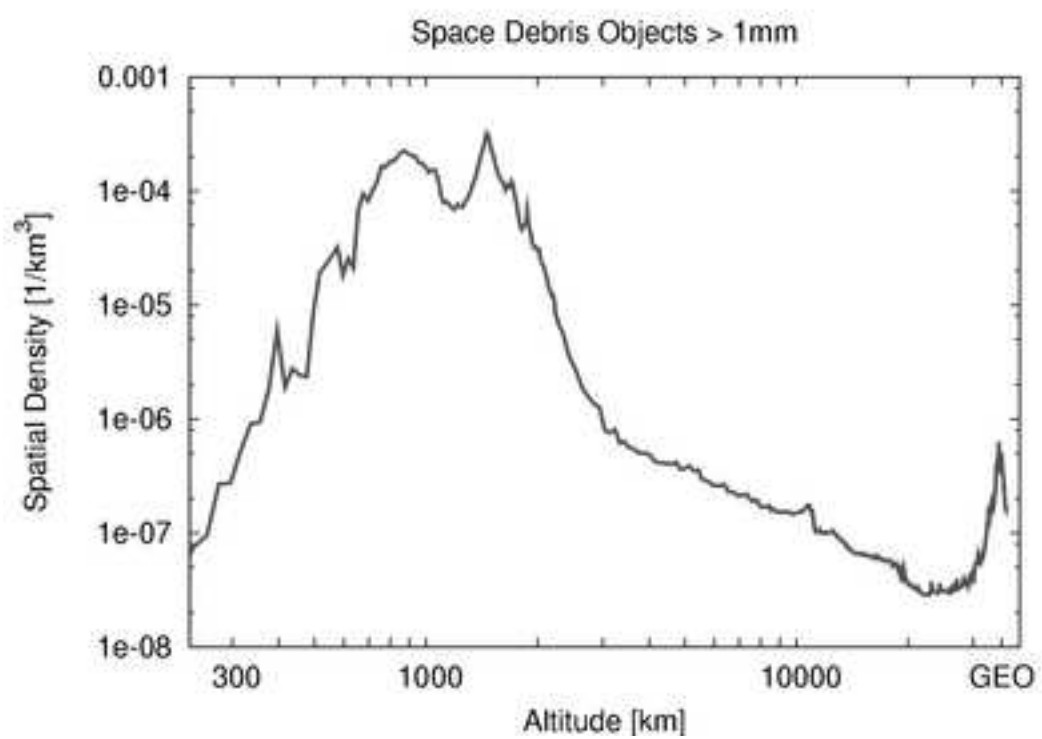


Figure 4.9: The orbital debris environment from LEO to GEO, from [Wikipedia, 2008]

4.7 Inclination plots

Table 4.3 shows the varying cases with an explanation of their initial conditions. This is an exact duplicate of Table 4.2, reprinted for reference.

case	i	$\dot{\psi}$	$\dot{\alpha}$	ι	ψ	α	eccent	τ
I1	0	0	0	0	0	0	0	1000
I2	0	0	0	$29\pi/180$	0	0	0	1000
I3	0	1	0	$29\pi/180$	0	0	0	1000
I4	0	0	0	$29\pi/180$	0	$-29\pi/180$	0	1000
I5	0	1	0	$29\pi/180$	0	$-29\pi/180$	0	1000

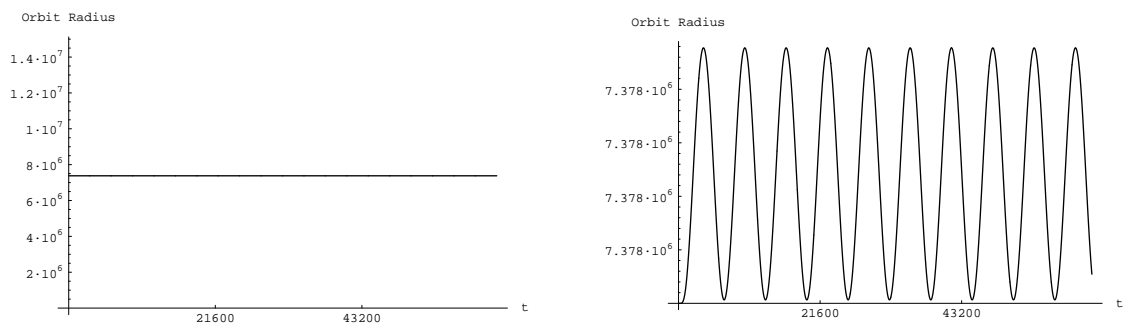
Table 4.3: Initial conditions for the inclination numerical solutions.

The initial conditions for the other parameters held constant are:

$$L = 1000 \text{ m}, M_{\text{payload}} = 10 \text{ kg}, M_{\text{tether}} = 100 \text{ kg}, M_{\text{facility}} = 500 \text{ kg}, e = 0,$$

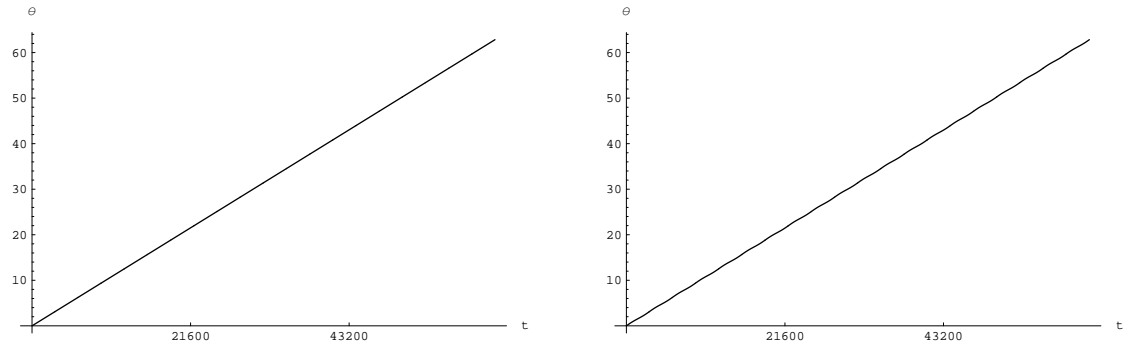
$$\dot{R}[0] = 0, \dot{\theta}[0] = 0.00113905 \text{ rad/s},$$

$$\theta[0] = 0, R[0] = 7.378 * 10^6 \text{ m}$$



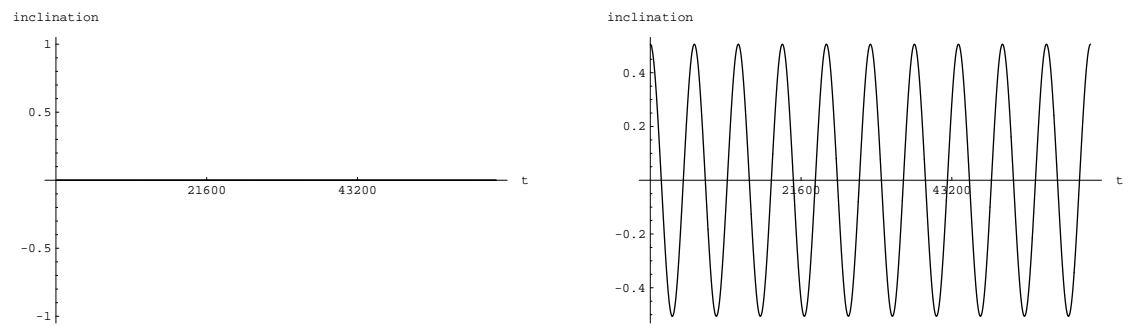
(a) Case 1: R (m) vs. time (s)

(b) Cases 2-5: R (m) vs. time (s)



(c) Case 1: θ (rad) vs. time (s)

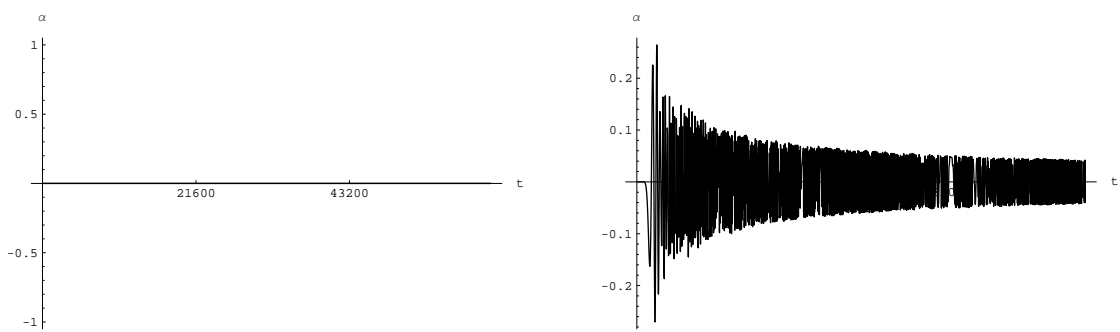
(d) Cases 2-5: θ (rad) vs. time (s)



(e) Case 1: ι (rad) vs. time (s)

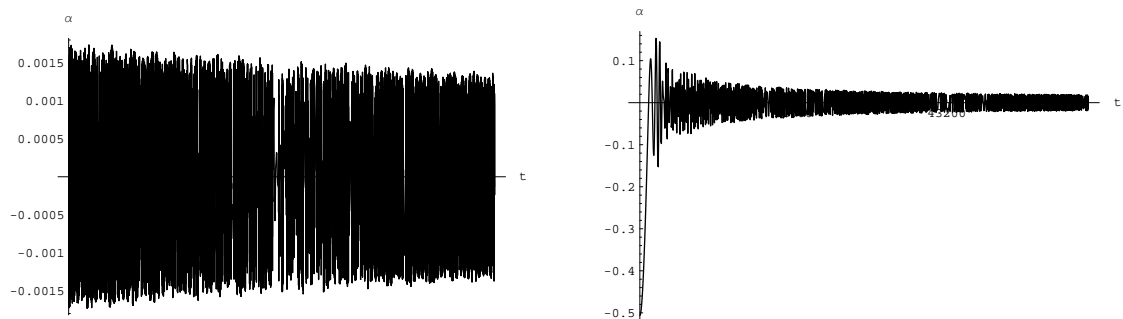
(f) Cases 2-5: ι (rad) vs. time (s)

Figure 4.10: Plots of R , θ and ι vs. time for the five cases.



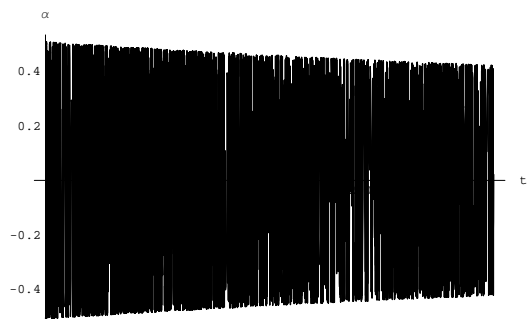
(a) Case 1: α (rad) vs. time (s)

(b) Case 2: α (rad) vs. time (s)



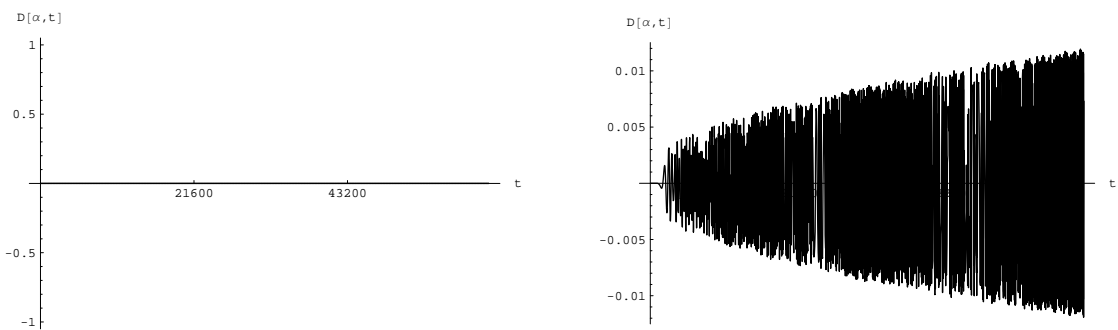
(c) Case 3: α (rad) vs. time (s)

(d) Case 4: α (rad) vs. time (s)



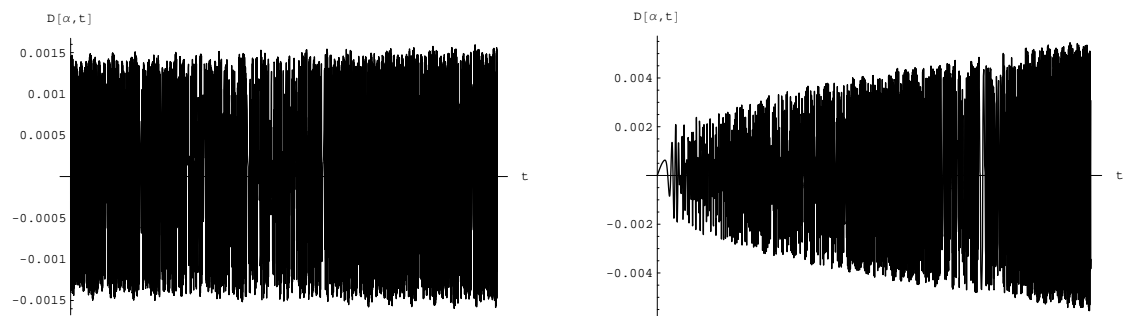
(e) Case 5: α (rad) vs. time (s)

Figure 4.11: Plots of α vs. time for the five cases.



(a) Case 1: $\dot{\alpha}$ (rad/s) vs. time (s)

(b) Case 2: $\dot{\alpha}$ (rad/s) vs. time (s)



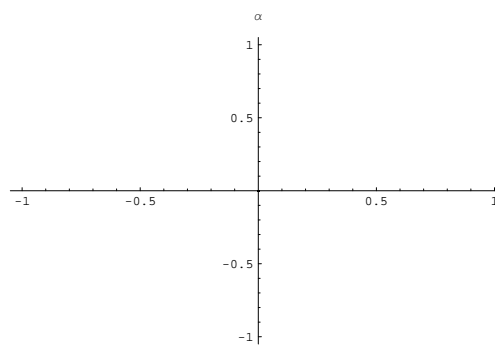
(c) Case 3: $\dot{\alpha}$ (rad/s) vs. time (s)

(d) Case 4: $\dot{\alpha}$ (rad/s) vs. time (s)

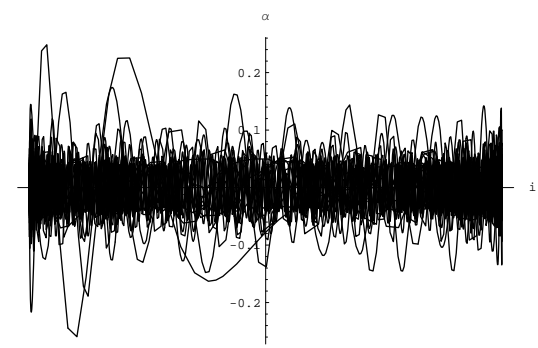


(e) Case 5: $\dot{\alpha}$ (rad/s) vs. time (s)

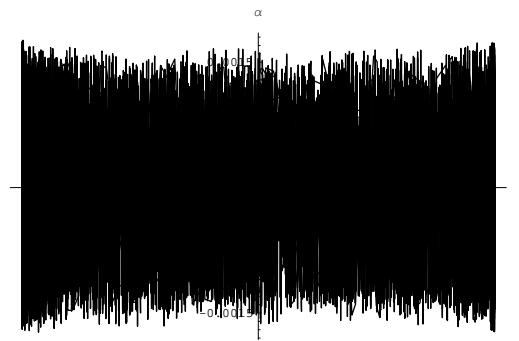
Figure 4.12: Plots of $\dot{\alpha}$ vs. time for the five cases.



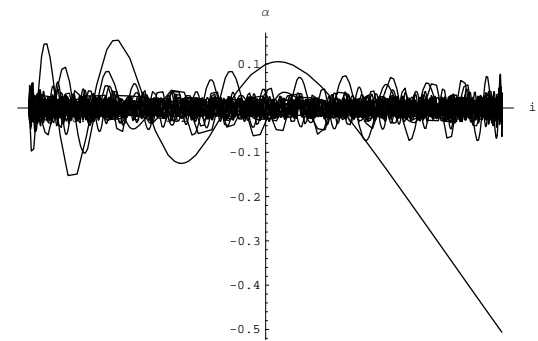
(a) Case 1: α (rad) vs. i (rad)



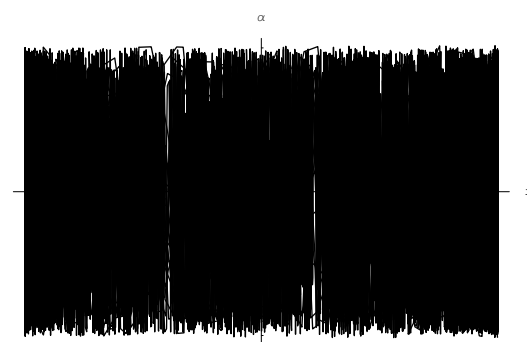
(b) Case 2: α (rad) vs. i (rad)



(c) Case 3: α (rad) vs. i (rad)



(d) Case 4: α (rad) vs. i (rad)



(e) Case 5: α (rad) vs. i (rad)

Figure 4.13: Plots of α vs. i for the five cases.

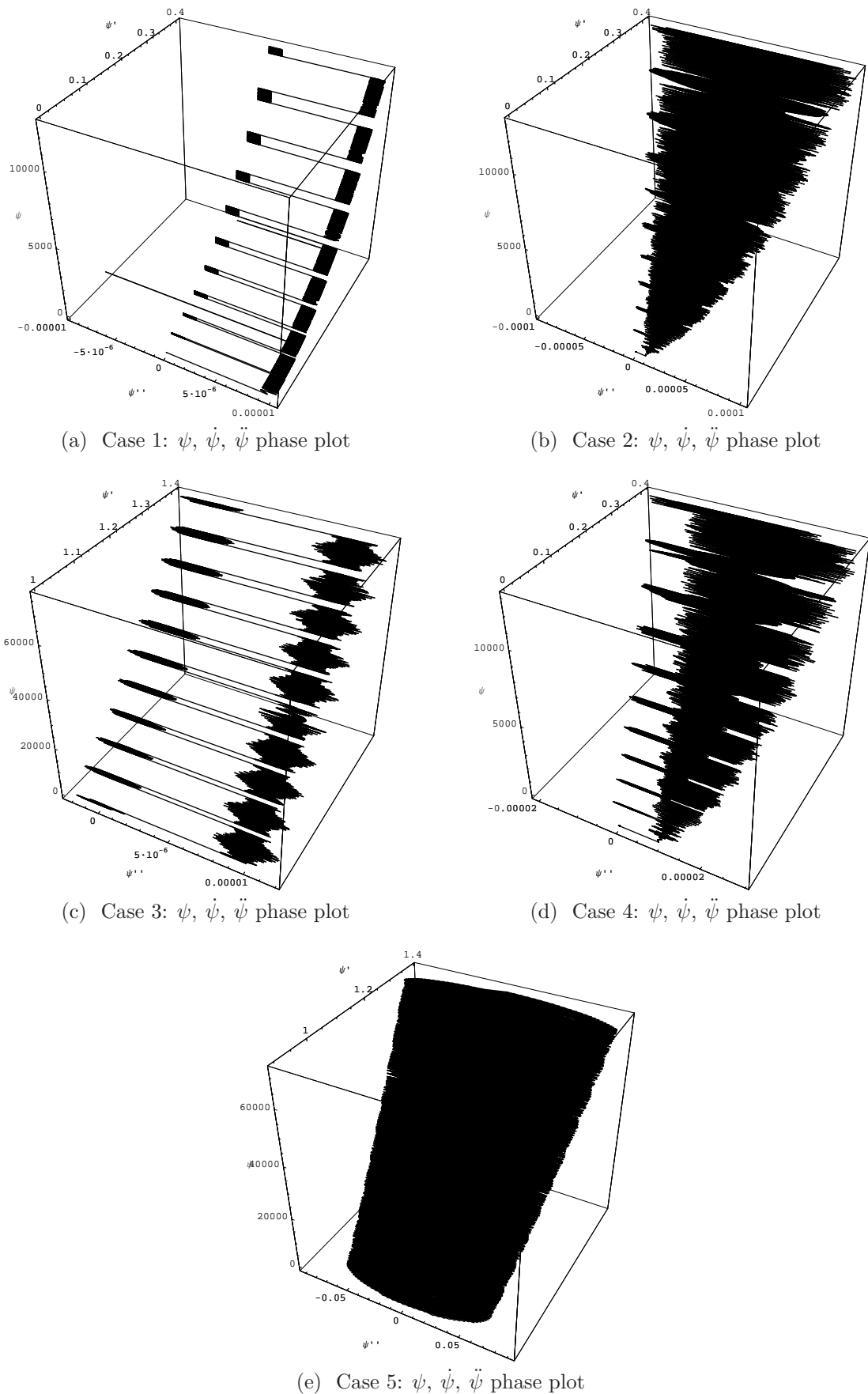


Figure 4.14: Phase plots of ψ for the five cases.

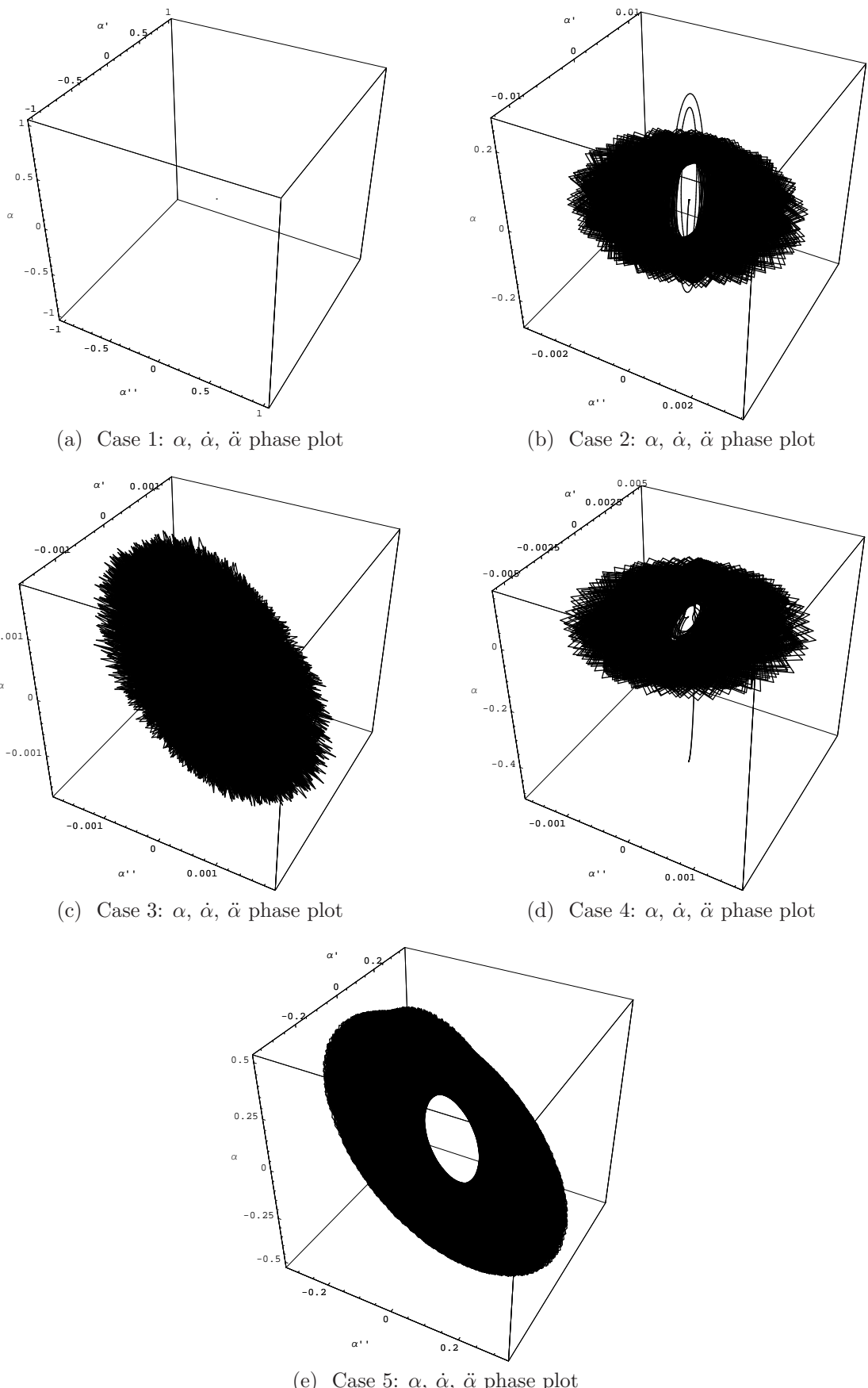
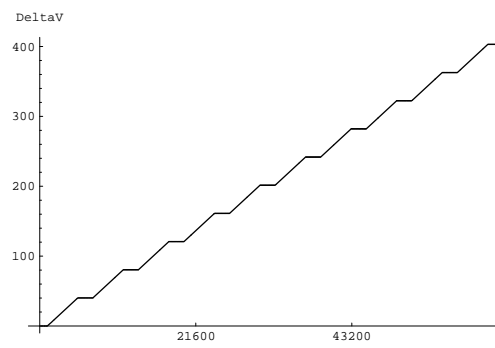
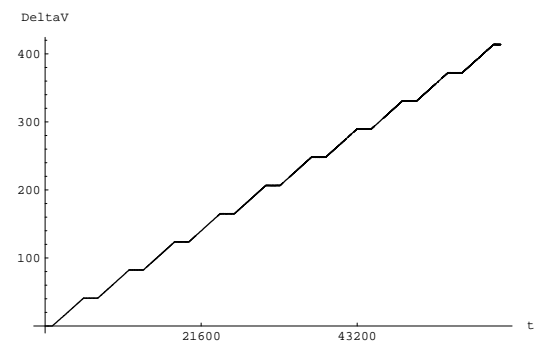


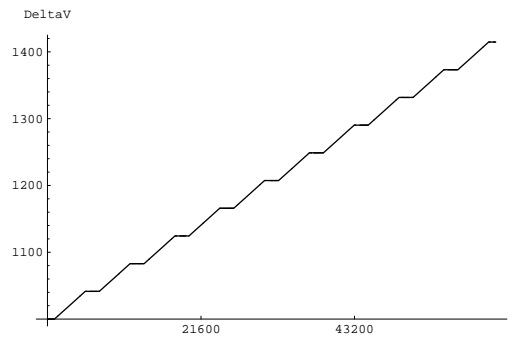
Figure 4.15: Phase plots of α for the five cases.



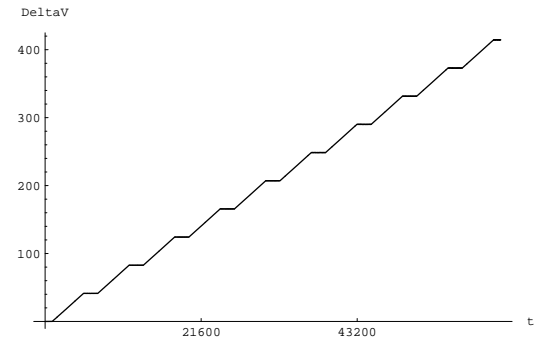
(a) Case 1: ΔV (m/s) vs. time (s)



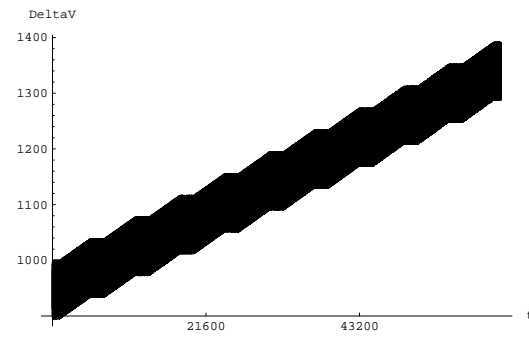
(b) Case 2: ΔV (m/s) vs. time (s)



(c) Case 3: ΔV (m/s) vs. time (s)

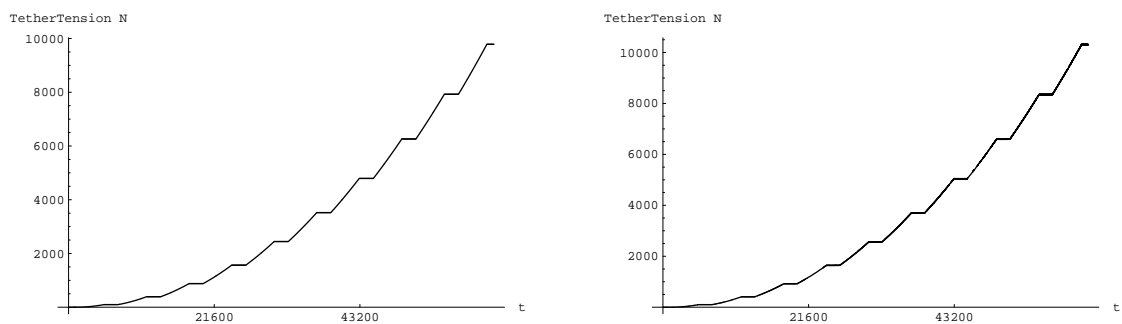


(d) Case 4: ΔV (m/s) vs. time (s)



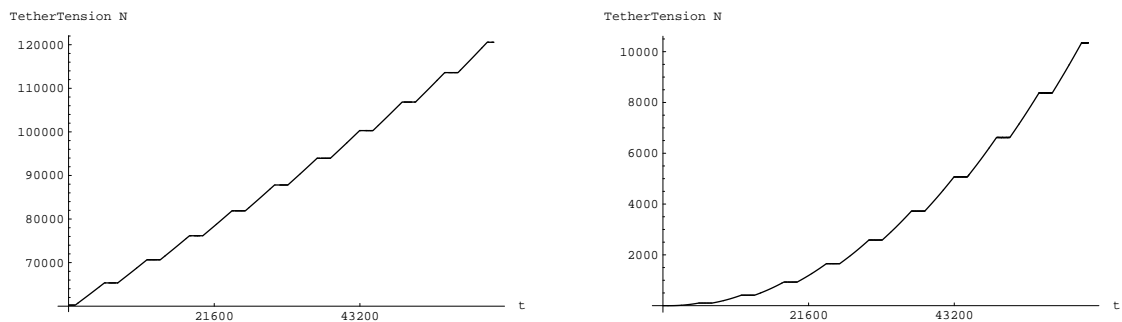
(e) Case 5: ΔV (m/s) vs. time (s)

Figure 4.16: Plots of ΔV vs. time for the five cases.



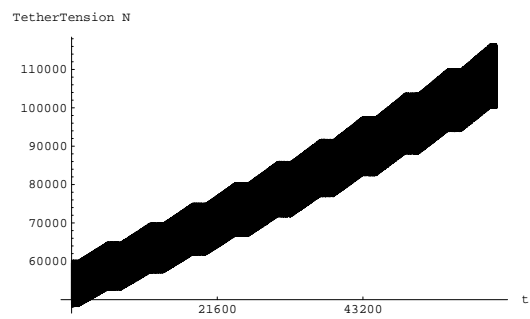
(a) Case 1: Tension (N) vs. time (s)

(b) Case 2: Tension (N) vs. time (s)



(c) Case 3: Tension (N) vs. time (s)

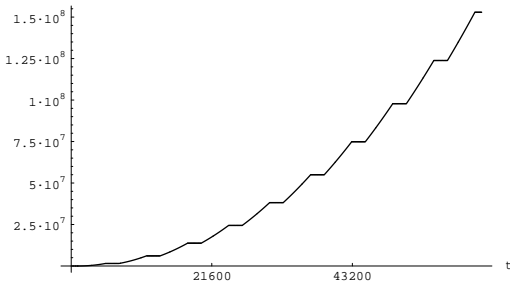
(d) Case 4: Tension (N) vs. time (s)



(e) Case 5: Tension (N) vs. time (s)

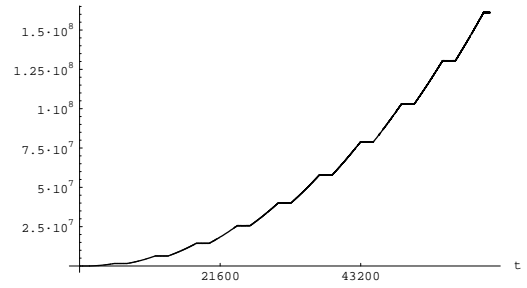
Figure 4.17: Plots of Tension vs. time for the five cases.

Tether Stress (Pa)
Tether Intact



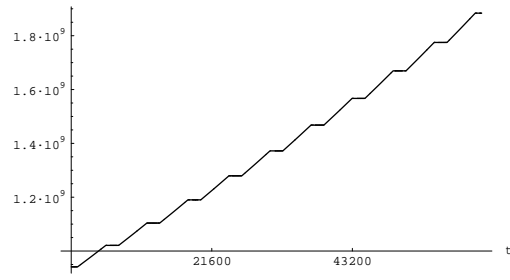
(a) Case 1: Stress (N/m^2) vs. time (s)

Tether Stress (Pa)
Tether Intact



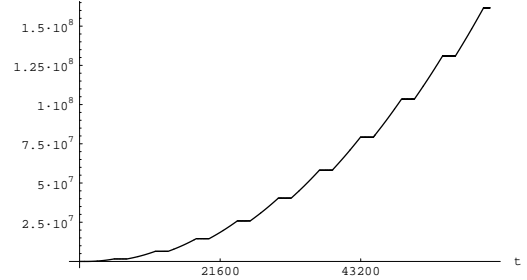
(b) Case 2: Stress (N/m^2) vs. time (s)

Tether Stress (Pa)
Tether Intact



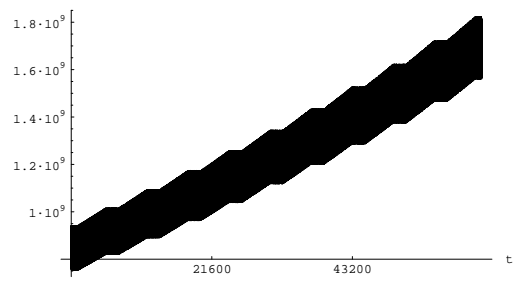
(c) Case 3: Stress (N/m^2) vs. time (s)

Tether Stress (Pa)
Tether Intact



(d) Case 4: Stress (N/m^2) vs. time (s)

Tether Stress (Pa)
Tether Intact



(e) Case 5: Stress (N/m^2) vs. time (s)

Figure 4.18: Plots of Stress vs. time for the five cases.

Chapter 5

Dynamics of tethers with length deployment

As has been shown in Chapter 4, it is possible to describe the motion of the MMET around complex orbital paths. Now the deployment characteristics of the MMET will be explored.

5.1 Deployment and recovery with the MMET

The two payload arms of the MMET may both be gainfully employed to launch two payloads, and this presents a set of unique challenges for the launcher. Both payload tethers must be able to demonstrate all the necessary properties of a single system tether, with the additional demands of a dual-launch system overlaid. The tethers must be strengthened for a potential asymmetric release, and the oscillations that this imposes on the system and tethers.

The generalised coordinates have been chosen in order to ascertain the impact that the length deployment has on the MMET without over-complicating the dynamics

of the system. The global coordinates R and θ have been included to model the orbital dynamics. The primary rotational coordinate, ψ , has been expanded to include both payload arms in the form of ψ_1 and ψ_2 . Similarly, each payload arm has been assigned a length coordinate, L_1 and L_2 , to enable independent, rigid motion of the extendable tether arm.

To limit the number of generalised coordinates, the inclination variable, ι , and the out-of-plane coordinate, α , have not been included as generalised coordinates. A six degree of freedom model will be adequate to examine the dynamics of length deployment, however a nine degree of freedom model has the potential to introduce orbital resonance to the deployment. At this early stage of research, nine degrees of freedom are too many to successfully isolate and examine the effects of length deployment on the system.

5.2 Addition of length as a generalised coordinate

The six variables of interest – $\{R, \theta, \psi_1, \psi_2, L_1, L_2\}$ – fulfil all the requirements of generalised coordinates. An analysis will be performed to investigate the effect that deployment and recovery have on the tether system orbit.

A system of equations will be constructed to include a symmetrical dumbbell tether with a facility mass at the centre of the system. The important mass points included in the model are the two identical payload masses, M_{payload} , the facility mass, M_{facility} , and the n discretized tether masses, M_{tether} , which are evenly distributed along each tether.

As before, the stator is not included in this model because this would significantly increase the complexity of the system.

As previously, Lagrange's equations will now be derived for the system.

5.3 Constructing the equations of motion

A system of Lagrange's equations is constructed using the rotational method described in Chapter 3, similarly employed for the inclination equations in Chapter 4.

The local position of the masses with respect to the facility mass are derived. This allows the centre of mass with respect to the facility mass to be calculated. The orbital positions are then assembled from these equations.

Simplifying assumptions have been made to lower the computational cost of assembling and solving these equations.

- The orbital length used in the calculation of potential energy is assumed to be the orbital radius vector, R . This is acceptable as $\frac{L}{R} \ll 1$.
- The orbital rotations have been decoupled from the local rotations. This is sufficient to analyse the fast rotations of the dual-payload system, but should be treated with caution when analysing the stationary characteristics of the MMET.
- The tethers are assumed to be rigid and inelastic.
- The cross-sectional area (CSA) of the tether is assumed to be constant along the tether length. The CSA will almost certainly be a function of length when the tether is built (i.e. tapered), however, this assumption builds in a level of conservatism into the analysis which can be refined at a later stage.

These assumptions are designed to maximise the benefit of the solution to the equations, while minimising the computational cost and minimising the risk of losing that information while studying a multi-parameter system.

As outlined in the above assumptions, the orbital and local rotations have been decoupled. The positional equation of the first payload therefore is defined as:

$$P_{\text{final1}} = R_{\theta,\text{Z}} \cdot (P_{0 \rightarrow \text{CoM}}) - (P_{\text{facility} \rightarrow \text{CoM}}) + (R_{\psi_1,\text{Z}} \cdot P_1) \quad (5.1)$$

As can be seen in Equation 5.1, the rotations are purely based on a series of Z-axis rotations.

Using the rotation matrices defined in Section 3.5, along with the following definitions¹ for the payload position:

$$P_1 = \begin{pmatrix} L_1 \\ 0 \\ 0 \end{pmatrix} \quad (5.2)$$

leads to the expanded version of the positional equation for payload 1: When evaluated, this becomes:

$$P_{\text{final1}} = \begin{pmatrix} R \cos \theta \\ R \sin \theta \\ 0 \end{pmatrix} - \begin{pmatrix} CoM_X \\ CoM_Y \\ CoM_Z \end{pmatrix} + \begin{pmatrix} L_1 \cos(\psi_1) \\ L_1 \sin(\psi_1) \\ 0 \end{pmatrix} \quad (5.3)$$

The position of the centre of mass from the facility, $P_{0 \rightarrow \text{CoM}}$, is calculated with the system mass points including the payload, facility and tether mass points.

The tether is discretized with each tether comprising n equal mass points, as shown in Equation 5.4 and Figure 5.1. The aim in discretizing the tether is to enhance the potential and rotational energy expressions. The n discrete mass elements were chosen so the centre of mass of the tether falls on the geometric centre of the tether, necessitating $n + 1$ spaces between the elements.

$$P_{0 \rightarrow \text{CoM}} = \begin{pmatrix} \frac{(M_1 + \frac{n}{2} M_{\text{tether } 1}) L_1 \cos(\psi_1) + (M_2 + \frac{n}{2} M_{\text{tether } 2}) L_2 \cos(\psi_2)}{M_1 + M_2 + M_{\text{facility}} + n M_{\text{tether } 1} + n M_{\text{tether } 2}} \\ \frac{(M_1 + \frac{n}{2} M_{\text{tether } 1}) L_1 \sin(\psi_1) + (M_2 + \frac{n}{2} M_{\text{tether } 2}) L_2 \sin(\psi_2)}{M_1 + M_2 + M_{\text{facility}} + n M_{\text{tether } 1} + n M_{\text{tether } 2}} \\ 0 \end{pmatrix} \quad (5.4)$$

To create Lagrange's equations, the position, velocity and energy of each point

¹Where L_1 is the length in absolute terms between the facility and the payload.



Figure 5.1: Discretised tether diagram with $n = 5$ mass points

must be determined.

The positions of all the mass points are given as:

$$P_{\text{payload } 1} = \begin{pmatrix} R \cos \theta \\ R \sin \theta \\ 0 \end{pmatrix} - \begin{pmatrix} CoM_X \\ CoM_Y \\ CoM_Z \end{pmatrix} + \begin{pmatrix} L_1 \cos(\psi_1) \\ L_1 \sin(\psi_1) \\ 0 \end{pmatrix} \quad (5.5)$$

$$P_{\text{payload } 2} = \begin{pmatrix} R \cos \theta \\ R \sin \theta \\ 0 \end{pmatrix} - \begin{pmatrix} CoM_X \\ CoM_Y \\ CoM_Z \end{pmatrix} + \begin{pmatrix} L_2 \cos(\psi_2) \\ L_2 \sin(\psi_2) \\ 0 \end{pmatrix} \quad (5.6)$$

$$P_{\text{tether } 1, j} = \begin{pmatrix} R \cos \theta \\ R \sin \theta \\ 0 \end{pmatrix} - \begin{pmatrix} CoM_X \\ CoM_Y \\ CoM_Z \end{pmatrix} + \begin{pmatrix} L_1 \cos(\psi_1) \\ L_1 \sin(\psi_1) \\ 0 \end{pmatrix} \left(\frac{j}{n+1} \right) \quad (5.7)$$

$$P_{\text{tether } 2, j} = \begin{pmatrix} R \cos \theta \\ R \sin \theta \\ 0 \end{pmatrix} - \begin{pmatrix} CoM_X \\ CoM_Y \\ CoM_Z \end{pmatrix} + \begin{pmatrix} L_2 \cos(\psi_2) \\ L_2 \sin(\psi_2) \\ 0 \end{pmatrix} \left(\frac{j}{n+1} \right) \quad (5.8)$$

$$P_{\text{facility}} = \begin{pmatrix} R \cos \theta \\ R \sin \theta \\ 0 \end{pmatrix} - \begin{pmatrix} CoM_X \\ CoM_Y \\ CoM_Z \end{pmatrix} \quad (5.9)$$

where each j is the number of the n tether mass points.

The velocity of each point is determined. The payload 1 is used as an illustrative

example: in local axes in Equation 5.10 and in inertial axes in Equation 5.11

$$V_{\text{payload 1, local}} = \begin{pmatrix} \dot{L}_1 \cos(\psi_1) - L_1 \sin(\psi_1) \dot{\psi}_1 \\ \dot{L}_1 \sin(\psi_1) + L_1 \cos(\psi_1) \dot{\psi}_1 \\ 0 \end{pmatrix} \quad (5.10)$$

$$V_{\text{payload 1, inertial}} =$$

$$\begin{aligned} & \begin{pmatrix} \dot{R} \cos(\theta) - R \dot{\theta} \sin(\theta) \\ \dot{R} \sin(\theta) + R \dot{\theta} \cos(\theta) \\ 0 \end{pmatrix} + \begin{pmatrix} -L_1 \dot{\psi}_1 \sin(\psi_1) + \dot{L}_1 \cos(\psi_1) \\ L_1 \dot{\psi}_1 \cos(\psi_1) + \dot{L}_1 \sin(\psi_1) \\ 0 \end{pmatrix} \\ & + \left(\frac{1}{M_1 + M_2 + M_{\text{facility}} + 2nM_{\text{tether}}} \right) \cdot \\ & \left[\begin{pmatrix} -\left(M_1 + \frac{n}{2}M_{\text{tether}}\right) \left(L_1 \dot{\psi}_1 \sin(\psi_1) - \dot{L}_1 \cos(\psi_1)\right) \\ -\left(M_1 + \frac{n}{2}M_{\text{tether}}\right) \left(L_1 \dot{\psi}_1 \cos(\psi_1) + \dot{L}_1 \sin(\psi_1)\right) \\ 0 \end{pmatrix} \right. \\ & \left. + \begin{pmatrix} \left(M_2 + \frac{n}{2}M_{\text{tether}}\right) \left(L_2 \dot{\psi}_2 \sin(\psi_2) - \dot{L}_2 \cos(\psi_2)\right) \\ \left(M_2 + \frac{n}{2}M_{\text{tether}}\right) \left(L_2 \dot{\psi}_2 \cos(\psi_2) - \dot{L}_2 \sin(\psi_2)\right) \\ 0 \end{pmatrix} \right] \end{aligned} \quad (5.11)$$

The expressions for energy are then calculated from the velocity and position information.

The translational kinetic energy, T_{trans} , of the system is calculated for the MMET

tether with n discrete masses per tether²:

$$\begin{aligned}
T_{\text{trans}} = & \frac{M_1}{2} V_{\text{payload } 1} \cdot V_{\text{payload } 1} + \frac{M_2}{2} V_{\text{payload } 2} \cdot V_{\text{payload } 2} \\
& + \sum_{j=1}^n \frac{M_{\text{tether}}}{2} V_{\text{tether } 1 \ j} \cdot V_{\text{tether } 1 \ j} \\
& + \sum_{j=1}^n \frac{M_{\text{tether}}}{2} V_{\text{tether } 2 \ j} \cdot V_{\text{tether } 2 \ j} \\
& + \frac{1}{2} (M_1 + M_2 + nM_{\text{tether}} + nM_{\text{tether}} + M_{\text{facility}}) (V_{\text{CoM}} \cdot V_{\text{CoM}})
\end{aligned} \quad (5.12)$$

The rotational kinetic energy, T_{rot} , of the system is found in a similar way:

$$\begin{aligned}
T_{\text{rot}} = & (I_{\text{payload } 1} + I_{\text{payload } 2}) \cdot (\omega_{\text{local}} \cdot \omega_{\text{local}}) \\
& + \sum_{j=1}^n I_{\text{tether } 1 \ j} \cdot (\omega_{\text{local } j} \cdot \omega_{\text{local } j}) + \sum_{j=1}^n I_{\text{tether } 2 \ j} \cdot (\omega_{\text{local } j} \cdot \omega_{\text{local } j})
\end{aligned} \quad (5.13)$$

where:

$$\omega_{\text{local}} = \begin{pmatrix} 0 \\ 0 \\ \dot{\psi} \end{pmatrix} \quad I_3 = \begin{pmatrix} 1 & 0 & 0 \\ 0 & 1 & 0 \\ 0 & 0 & 1 \end{pmatrix}$$

$$I_{\text{payload } 1} = L_1^2 M_{\text{payload } 1} \cdot I_3 \quad I_{\text{payload } 2} = L_2^2 M_{\text{payload } 2} \cdot I_3$$

$$I_{\text{tether } 1 \ j} = L_{1j}^2 M_{\text{tether } 1 \ j} \cdot I_3 \quad I_{\text{tether } 2 \ j} = L_{2j}^2 M_{\text{tether } 2 \ j} \cdot I_3$$

The evaluated sum of the component rotational kinetic energies for $n = 10$ tether masses are:

$$T_{\text{rot}} = \frac{L_1^2 M_1 \dot{\psi}_1^2}{2} + \frac{L_2^2 M_2 \dot{\psi}_2^2}{2} + \frac{35 M_{\text{tether}}}{22} \left(L_1^2 \dot{\psi}_1^2 + L_2^2 \dot{\psi}_2^2 \right) \quad (5.14)$$

²Where M_{tether} is the discrete mass point, this sums to the total tether mass $M = n M_{\text{tether}}$.

The sum of the potential energies, U , are:

$$U = \sum_{j=1}^n \frac{\mu m_j}{|P_j|} \quad (5.15)$$

where P_j are the mass point locations given in Equations 5.5 to 5.9.

The potential energy term is simplified by using the assumption that the mass points are sufficiently close to the centre of mass of the system, that is $\frac{P_j}{R} \ll 1$, that the potential energy of each mass point of the system may be represented as if it were at a distance R from the major gravitational body. The evaluated form of one tether arm is therefore:

$$U = \sum_{j=1}^n \frac{\mu m_j}{R} = \frac{n M_{\text{tether}}}{R} \quad (5.16)$$

Summing over all the mass points³ gives the full form for the potential energy of the MMET:

$$U = -\frac{\mu M_1}{R} - \frac{\mu M_2}{R} - \frac{20 \mu M_{\text{tether}}}{R} - \frac{\mu M_{\text{facility}}}{R} \quad (5.17)$$

The Lagrangian is then given by $\mathbb{L} = T - U$.

Lagrange's equations are then generated for the five generalised coordinates, $\{R, \theta, \psi_1, \psi_2, L_1, L_2\}$ as follows:

$$\frac{d}{dt} \left(\frac{\partial T}{\partial \dot{q}_j} \right) - \frac{\partial T}{\partial q_j} + \frac{\partial U}{\partial q_j} = Q_j \quad (5.18)$$

5.4 Non-conservative forces

The motor on the MMET spins up the payload arms, while the counter-torque rotates the stator in the opposite direction. This is a non-conservative force in action, as the energy is transferred from the solar cells⁴ to the rotational motion of

³There are 10 discrete mass points on each tether.

⁴Or the equivalent driving power source.

the payloads, via the motor. The non-conservative forces are derived according to the principles of virtual work outlined in Section 3.4:

$$Q = \begin{pmatrix} 0 \\ 0 \\ \tau \cos(\gamma) \\ \tau \cos(\gamma) \\ -\left(L_{damp} \dot{L}_1^2\right) \\ -\left(L_{damp} \dot{L}_2^2\right) \end{pmatrix} \quad (5.19)$$

where τ is the torque magnitude, γ is the angle that the torque acts relative to the in-plane spin and L_{damp} is a braking term modelling the action of the spool-out mechanism. The form of the tether friction braking was taken after the velocity based barber-pole braking system analysed in [Lennert and Cartmell, 2006].

5.4.1 Tether braking

It is proposed to use a barber pole braking system for this tether analysis. This is a passive system employed to minimise the need for an active control system or complicated reel-out mechanism. The kinetic energy of the tether and payload spools out the tether with friction forces providing resistance to ensure the tether is deployed in a controlled manner.

The braking force on the tether will be proportional to the square of the speed of deployment:

$$F = -\left(L_{damp} \dot{L}^2\right) \quad (5.20)$$

where L_{damp} is a proportional constant modelling the friction properties and physical characteristics of the braking system. This allows a flexibility to either define the damping coefficient to reflect a physical braking system or to specify a damping coefficient and match a braking system to the numerical modelling.

5.5 Analysis of length deployment of tether

The MMET is different to other tether systems by virtue of the dual-payload motorized arrangement of its tethers. This confers several advantages through the symmetric arrangement of the payloads, however the dynamics of the spin-up are untested in an orbital environment⁵.

A goal is set to study the dynamics of the MMET system: it must be capable of imparting a $\Delta V = 1000 \text{ m/s}$ to the payloads. This is a moderate velocity increment that will demonstrate the usefulness of the MMET system, allowing inclusion on a small launcher or as a secondary payload.

The system of equations is solved in Mathematica™, using NDSolve, for a time of $t = 208129 \text{ s}$ (approx 33 orbits). Figures 5.2 and 5.3 show the results for the following initial conditions:

$$\begin{aligned} M_1 &= M_2 = 10 \text{ kg}, M_{\text{tether}} = \frac{100}{10} = 10 \text{ kg}, M_{\text{facility}} = 500 \text{ kg}, \\ \dot{R}[0] &= 0, \dot{\theta}[0] = 0.00113905 \text{ rad/s}, \dot{\psi}_1[0] = 0.1 \text{ rad/s}, \dot{\psi}_2[0] = 0.1 \text{ rad/s}, \\ \dot{L}_1[0] &= 0, \dot{L}_2[0] = 0, R[0] = 7.378 * 10^6 \text{ m}, \theta[0] = 0, \psi_1[0] = 0.01^\circ, \psi_2[0] = 180.1^\circ, \\ L_1[0] &= 100 \text{ m}, L_2[0] = 100 \text{ m}, L_{\text{damp}} = 5 * 10^8 \text{ kg/m}, \tau_{\text{max}} = 1000 \text{ Nm} \end{aligned}$$

A further explanation of the starting conditions is below:

- the starting radius $R[0]$ is equivalent to 1000 km above the surface of the Earth.
- the motor torque is proportional to time, and increases from $\tau = 0$ at $t = 0 \text{ s}$ to $\tau = 1000 \text{ Nm}$ at $t = 208129 \text{ s} \approx 33$ orbits.
- the initial conditions for the tether positions, ψ_1 and ψ_2 are chosen to be slightly asymmetrical.
- the tether mass, M_{tether} , is the *discretized* mass of a section of the tether, the total tether mass in this case is given by $nM_{\text{tether}} = 100 \text{ kg}$.

⁵For details of ground testing and analysis, see [Cartmell et al., 2003].

An asymmetry in the initial tether angles was chosen to counter numerical integration problems – the numerical solver has great difficulties in integrating the equations of motion when the tether arms are exactly 180° apart. The small asymmetry is acceptable, as the tether arms will never be exactly opposite.

The solution to the equations of motion for the above initial conditions are given in Figures 5.2 to 5.4.

5.5.1 Discussion of results for deployment

As can be seen in Figures 5.2a, the radius vector R is constant – this is due to the assumption in the expression for potential energy that the masses act at distance R from the inertial origin.

The motor torque shown in Figures 5.2b is increased linearly to a maximum torque to avoid any large start-up transients. This is key to ensure a smooth deployment phase. A slow increase in the torque results in a gradual increase in the tether rotational velocity, and a gradual increase in the stress in the tether.

The length of the payload 1 tether smoothly reels out from the hub, as shown in Figures 5.2c, first slowly, then speeds up to a moderate and predictable linear increase due to the tether braking⁶.

If the torque was suddenly increased from zero to maximum, the initial few minutes of deployment would be uncontrolled, and this is likely to cause significant problems in several areas – including tether asymmetry and nonlinear flexing in the tethers. This would invalidate the previous assumptions, perhaps leading to payload/stator interaction, which is to be avoided at all costs.

The linear scaling in torque undoubtedly delays the overall time taken to deploy the tether, compared to a flat maximum torque profile, and could be optimised

⁶Recall that the tether braking force is proportional to the square of the tether velocity: $F \propto -L_{damp}\dot{L}^2$

further. This is a conservative approach to ensure the safe deployment of the tether, and inevitably leads to a longer deployment time than is absolutely necessary.

The torque drives the tether rotational speed, as shown in Figures 5.2d: it first increases, then trends back to an asymptote at around 1.35 rad/s .

The profile of angular velocity varying with length is shown in Figure 5.3b. This shows that the rate of increase of $\dot{\psi}_1$ is within acceptable limits and will not place onerous demands on the strength of the tether.

The potential ΔV the payload may achieve is defined as the dependence between the rotation and length, $\Delta V = \dot{\psi}_1 L_1$, and is shown in Figure 5.3a. The ΔV increases approximately linearly, in contrast to the nonlinear behaviour of the angular rotation and length generalised coordinates. At the end of the numerical integration, $\Delta V \approx 1000 \text{ m/s}$.

One issue with the MMET system is that there is a possibility of mutual interference with the tethers of the payload and stator arms. As Figures 5.3c and 5.3d show, in this case, the difference between the angle of the tethers and the lengths of the tethers are small. The angular difference is nominally zero after a start-up transient, with an initial maximum of $\approx 0.5^\circ$, which is acceptable for the spin-up criteria⁷. The difference in lengths of the tethers are minimal – this is likely a result of rounding errors encountered using a numerical solver.

Analysing the tension and stress in the tether shows that the tether is intact and within material bounds. The tether tension, shown in Figure 5.4a, at around 100 kN is high, but within acceptable limits. The stress, shown in Figure 5.4b, assumes a CSA of 64 mm^2 , equivalent to a single circular section⁸ of diameter 9 mm .

The stress level in the tether is below failure point. The tensile strength of Zylon

⁷This may be unacceptable for the final ‘launch phase’ of the payloads where the required accuracy of the tether angle is likely to be more stringent.

⁸This is a simplifying assumption – a tether launch satellite would be likely to employ a combination of a tapered tether to reduce the mass along the span of the tether and a multi-strand tether to mitigate against single-strand failure.

fibre is 5.9 GPa ; with a safety factor of 1.5, the maximum acceptable tensile strength is 3.9 GPa . The maximum calculated stress in the tether is 1.6 GPa , which provides an additional level of redundancy in the tether. The total safety factor is approximately $\frac{1.6}{5.9} = 3.7$.

The stress in the tether has been designed to be linear, avoiding step-increases in the stress and allowing the load to distribute evenly along the fibre in a progressive way.

The tether tension is calculated as the sum of the tension due to the tether mass and the payload:

$$T = \frac{1}{2} A \rho L_1^2 \dot{\psi}_1^2 + L_1 M_1 \dot{\psi}_1^2 \quad (5.21)$$

where A is the cross-sectional area (CSA) of the tether, and ρ is the tether density. The tether stress is defined conventionally as:

$$\sigma = \frac{T}{A} \quad (5.22)$$

5.6 Refining the equations of motion

A refinement of the tether mathematical model is proposed. Whereas the previous model describes a discretized tether of constant mass, M_{tether} , this can be more accurately modelled as a mass proportional to the tether length:

$$M_{\text{tether}} = \frac{\rho A L}{n} \quad (5.23)$$

where ρ is the tether density, and $\frac{L}{n}$ is the effective distance between mass points.

As shown previously in Figure 5.1, the tether mass model allows the dynamics of a varying tether mass to be investigated. This is more accurate, better reflecting the realities of the mass distribution when the tether is deployed.

The previous set of equations modelled the mass points as fixed fractions of the tether which moved proportional to each other and did not vary in mass. This is unsatisfactory because the entire tether mass would be distributed over the length of the tether, whether the tether length is a few metres or at full deployment. Obviously, this is not representative of the tether mass therefore a new model is proposed to better describe the tether mass in Equation 5.23. This refines the tether mass model to increase the tether mass in proportion to the length of the tether, giving a more representative model of the tether mass.

As with the previous investigation into the deployment of the tether, the equations of motion are solved for the following initial conditions for a time period⁹ of 69376 s:

$$\begin{aligned} M_1 &= M_2 = 10 \text{ kg}, M_{\text{tether}} = \rho A L / n, M_{\text{facility}} = 500 \text{ kg}, \\ \rho &= 1570 \text{ kg/m}^3, A = (0.008)^2 = 0.000064 \text{ m}^2, n = 10 \\ \dot{R}[0] &= 0, \dot{\theta}[0] = 0.00113905 \text{ rad/s}, \dot{\psi}_1[0] = 0.1 \text{ rad/s}, \dot{\psi}_2[0] = 0.1 \text{ rad/s}, \\ \dot{L}_1[0] &= 0, \dot{L}_2[0] = 0, R[0] = 7.378 * 10^6 \text{ m}, \theta[0] = 0, \psi_1[0] = 0.01^\circ, \psi_2[0] = 180.1^\circ, \\ L_1[0] &= 100 \text{ m}, L_2[0] = 100 \text{ m}, \tau_{\max} = 1000 \text{ Nm}, L_{\text{damp}} = 5 * 10^8 \text{ kg/m} \end{aligned}$$

To avoid the problem of initially over-accelerating the payloads, a nonlinear torque is applied by the tether motor, as shown in Figure 5.5b. This effectively limits the initial spin-up torque, limiting the angular acceleration and providing a stable basis for controlled deployment. The maximum value of angular acceleration is 0.025 rad/s^2 , and the maximum angular speed is 10.2 rad/s . Figure 5.5d shows a time-history of $\dot{\psi}$ with a moderate angular acceleration in the first few seconds of spin-up, followed by a progressive and controlled deployment of the tether thereafter.

The torque is controlled in such a way to avoid an initial spike of acceleration, to progress rapidly to a high-torque plateaux and furthermore, to provide a smooth

⁹This corresponds to exactly 11 orbits.

transition between the two.

$$\tau = \tau_{max} \cdot \exp\left(\frac{-7500}{t+1}\right) + 50 \quad (5.24)$$

where the maximum torque provided by the motor, $\tau_{max} \approx 1000 \text{ Nm}$ and t is the elapsed time in seconds.

A significant advantage of the motor torque control is that the tether is deployed linearly, with the intention of limiting the jerk or acceleration to the tether, as shown in Figure 5.5c. The linear deployment is very successful in limiting the tension and stress in the tether, see Figure 5.7a and Figure 5.7b respectively.

The expression for the tether tension at the facility (i.e. the point of greatest tension) has changed compared to the previous tether mass model described in Equation 5.21. The tension is not calculated with respect to the centre of mass of the tether in the centre of the tether, it is instead assumed that the tether mass acts in its entirety at the root of the tether. The tether tension in the discretized tether is calculated as:

$$T = A \rho L_1^2 \dot{\psi}_1^2 + L_1 M_1 \dot{\psi}_1^2 \quad (5.25)$$

where A is the cross-sectional area of the tether, and ρ is the tether density.

When examining stresses in the tether, the maximum stress levels for the exponential torque case appears higher at 2.1 GPa , compared to 1.3 GPa for the linear torque model. This is due to the differing tension (and therefore, stress) expressions in the two cases, and can not be directly compared.

However, if the stress is qualitatively examined, it is interesting to compare the stress profiles. The time at which the maximum stress is applied is very different; with the linear torque case, the stress is maximum at the end of the spin-up just before payload release; with the exponential torque case, the stress quickly rises to maximum early in the spin-up, and is eased slightly before payload release achieving

a stress before release of 1.75 GPa . The maximum allowable stress, for comparison, is 3.9 GPa

The time taken to spin the payload to release velocity is significantly less in the exponential torque case – the time taken to spin-up is one third of the linear torque case. This is partly due to the difference in mass modelling, and partly due to the torque profile used. This represents a marked improvement, and will undoubtedly enhance the economic strengths of the MMET as a renewable launch platform.

In terms of tether synchronisation, Figures 5.6c reveals that the tethers are well separated by approximately 180° , and furthermore, they tend to settle at a point diametrically opposed to each other. This is an important result, especially when the tethers are initially separated by a few fractions of degrees as would occur in a real spin-up scenario. The solution to the equations of motion were based on the initial conditions $\psi_1 = 0.01^\circ$ and $\psi_2 = 180.1^\circ$.

Likewise, in Figure 5.6d, the difference in tether lengths are minimal. This may not be true in the real world, as material properties and coefficients of friction are very difficult to exactly match between the two tether arms. Clearly, the asymmetrical spin-up scenario requires further study.

As it is clear that deploying the tethers with a MMET system is achievable for a modest payload, the recovery of the tether model shall be examined.

5.7 Recovery of tethers

One of the strengths of the MMET is in its role as a reusable launcher of payloads. In order to re-use the tethers, they must be de-spun and then recovered to the facility.

The hardware required to perform the de-spin is a large braking system – the disc brake system on a car axle is similar in operation to what may be required. There are important differences, however, as the disc brake must be cooled. On Earth's

roads, the cooling is provided by conductive heat transfer of air; on orbit, conduction and radiation are necessary to channel the excess heat away from the brake to the vacuum of space.

The required braking energy is significant – approximately equal to the energy supplied to accelerate the tether to release velocity. The power supplied by the solar cells to the motor will be comparable to the power required to brake the assembly, assuming equal time spent accelerating and decelerating the payloads. Given that the solar cells are currently in the kW range, the braking system and heat dissipation systems should be sized accordingly and should not burdensome to source.

5.7.1 Recovery profile

Recovery requires a different approach to deployment – the two are conceptually opposite, but can not be treated as mirror images when analysing the technicalities as there are important differences between the two cases.

Deployment simply requires a spinning motor and a braking system, the tether arms held rigid by the rotation.

When recovering the arms, there are requirements that must be fulfilled:

- the tethers must be slowed gradually to avoid backlash and tether tangling
- there must be a minimum spin rate to keep the tether rigid
- the tethers must be fully recovered to enable a subsequent deployment

The initial slow-down phase is similar to the spin-up phase – energy is dissipated during the slow-down to minimise tension in the tether, making recovery easier. The motor required to reel the tether in for storage may require less power (doing less work against the tether tension) and therefore will be lighter and cheaper.

5.7.2 The equations of motion for recovery

The equations of motion are the same as the deployment equations of motion for the orbital generalised coordinates, R and θ , and the spin generalised coordinates, ψ_1 and ψ_2 . The length generalised coordinates, L_1 and L_2 shown in Equations 5.26 and 5.27, differ in the fact that they are not braked to stop fast deployment, but they are retracted under motor power. Similarly, the initial conditions and non-conservative forcing terms¹⁰ have been altered to reflect the differences between decelerating and accelerating the tether arms.

The aim of the new length equations of motion is to provide a consistent length recovery rate for the tethers: $\dot{L} = -v$. This models a constant speed motor reeling in the tethers. A small acceleration term, \ddot{L} , is added to make both length equations into two ODEs, such that the equations of motion may be solved numerically.

$$0.000001\ddot{L}_1 + \dot{L}_1 = -L_{rec} \quad (5.26)$$

$$0.000001\ddot{L}_2 + \dot{L}_2 = -L_{rec} \quad (5.27)$$

The non-conservative forces in the right hand side of Largange's equations are:

$$Q = \begin{pmatrix} 0 \\ 0 \\ -(\psi_{damp} \dot{\psi}_1) \\ -(\psi_{damp} \dot{\psi}_2) \\ -(L_{rec}) \\ -(L_{rec}) \end{pmatrix} \quad (5.28)$$

The non-conservative forces for the length equations of motion provide a constant reel-in speed, modelled by the rate L_{rec} . Similarly, the spin generalised coordinates

¹⁰ The right hand side terms of Lagrange's equations, shown in Equation 5.28.

dictate a linear braking proportional to the rotational speed of the tethers.

5.7.3 Solving the equations of motion for recovery

The recovery stage necessitates a two-stage approach to recovering the tether. The first stage recovers the tethers close in to the facility, at which point a slower recovery stage is used to safely guide the remaining length of tether into the facility.

The tether arms must be kept rigid¹¹, and this requires a minimum rotational velocity of the tether system. The tether is decelerated to a small rotational velocity in the first phase with a constant braking force. Once the tether arm is rotating slowly, close to the facility, a much lower braking force and marginally lower tether retraction speed are employed to ensure the safe recovery of the last section of tether.

The initial conditions for the first recovery phase, numerically solved for a time period of 50000 s, are:

$$M_1 = M_2 = 10 \text{ kg}, M_{\text{tether}} = \rho A L / n, M_{\text{facility}} = 500 \text{ kg},$$

$$\rho = 1570 \text{ kg/m}^3, A = (0.008)^2 = 0.000064 \text{ m}^2, n = 10,$$

$$\dot{R}[0] = 0, \dot{\theta}[0] = 0.00113905 \text{ rad/s}, \dot{\psi}_1[0] = 1.0 \text{ rad/s}, \dot{\psi}_2[0] = 1.0 \text{ rad/s},$$

$$\dot{L}_1[0] = 0, \dot{L}_2[0] = 0, R[0] = 7.378 * 10^6 \text{ m}, \theta[0] = 0, \psi_1[0] = 0.01^\circ, \psi_2[0] = 180.1^\circ,$$

$$L_1[0] = 1000 \text{ m}, L_2[0] = 1000 \text{ m}, \text{Torque}_{\max} = 0 \text{ Nm},$$

$$L_{\text{rec}} = 0.015 \text{ kg/m}, \psi_{\text{damp}} = 1500 \text{ Ns}$$

Again, an asymmetry in the tether angles was chosen to reflect the unknowns that affect the payload release dynamics. Additionally, the numerical solver has great difficulties in integrating the equations of motion when the tether arms are exactly 180° apart.

The second phase of recovery has the initial conditions similar to the first phase, and is numerically solved for a time period of 25000 s. Initial conditions that differ

¹¹This is an explicit assumption made when assembling the equations of motion.

are listed below:

$$\begin{aligned}\dot{\psi}_1[0] &= 0.026707 \text{ rad/s}, \dot{\psi}_2[0] = 0.026707 \text{ rad/s}, \\ \dot{L}_1[0] &= 0, \dot{L}_2[0] = 0, \\ L_1[0] &= 250 \text{ m}, L_2[0] = 250 \text{ m}, \\ L_{\text{rec}} &= 0.010 \text{ kg/m}, \psi_{\text{damp}} = 100 \text{ Ns}\end{aligned}$$

The goal for recovery of the tethers are to provide a stable and controlled reel-in, avoiding scenarios that would lead to a break of the tether such as tether asymmetry or uncontrolled resonance in the tether.

For a circular orbit and a linear tether recovery profile, the payload tethers remain separated by approximately 180° . The maximum range of tether movement from the symmetric centre line is approximately 0.43° , as shown in Figures 5.9c and 5.12c. Furthermore, there are no significant deviations or other areas of concern in either the spin angle or the tension or stress profiles.

The tension and stress in the tether are gradually lowered, while keeping the tether taut, as seen in Figures 5.10a, 5.13a, 5.10b and 5.13b. This will not guarantee a successful recovery, but will reduce the risk of a transient phenomenon that may cause the tether to momentarily rise above the ultimate strength of the material, thus breaking the tether.

The rotational speed of the arms initially increase due to conservation of momentum, as the length (and therefore inertia) of the tethers are reduced. Angular momentum is conserved, and as Figure 5.9b clearly shows, the tether payloads rotate at a faster rate while reeled in. This does not lead to an increase in the tension or ΔV due to the careful choice of the rotational braking system (and braking constant ψ_{damp}) and the reel-in speed (L_{rec}).

The second phase of tether recovery is shown in Figures 5.11 to 5.13. This occurs with 250 m of tether still outside the facility, i.e. one quarter remaining to recover. The tether arms are rotating slowly enough to reduce the tension in the tether to

minimal levels, while keeping the tether rigid enough to ensure the equations of motion remain valid in describing the motion.

The tether arms are decelerated at a lower rate than the previous recovery phase, with $\psi_{\text{damp}} = 100 \text{ Ns}$. The tether recovery rate is slowed slightly to $\dot{L} = 0.1 \text{ m/s}$.

Similar to the first recovery phase, the remaining tether is slowly retracted into the facility with no adverse dynamic effects. The angle between the tethers remains at approximately $180^\circ \pm 0.5^\circ$. However, at such a low tension, it is unknown whether the tether can remain rigid without coiling or exhibiting other nonlinear behaviour. An in-depth analysis should be performed to ascertain the tether's behaviour in such an environment, as a study that involves non-rigid tether behaviour is beyond the scope of this thesis.

The time taken to deploy then recover the tether is $69376 + (50000 + 25000) = 144376 \text{ s}$, ≈ 40 hours, or a little under 22 orbits¹², not taking into account the time taken to release the payloads and the time to stabilise the tethers between the two recovery stages. This short timespan allows a small swarm of 18 nano-satellites to be launched from the MMET within a month.

As one of the key strengths of the MMET is the re-usability of the platform, this is an encouraging finding.

5.8 Deployment and recovery on an elliptical orbit

The MMET describing an elliptical orbit may interact with the tether while deploying or retracting the tethers. In order to study this, a sensitivity analysis is carried out to ascertain if this hypothesis is correct.

The deployment and recovery of the tether are carried out under identical initial

¹² One orbit takes approx. 6307 s at an altitude of 1000 km.

conditions to the equations describing the discretized mass model with the exponential tether tension model.

The non-dimensional ellipse eccentricity parameter, $e = 0.25$, is supplied to the initial conditions of Lagrange's equations of motion through the orbital angle initial condition: $\dot{\theta} = 0.00111382 \text{ rad/s}$.

This is calculated using the semi-latus rectum and orbital parameters, as in [Szabolcs and Mark, 1998], to calculate the orbital angular velocity thus:

The semi-latus rectum (SLR) is calculated:

$$SLR = R(1 + e \cos(\theta)) \quad (5.29)$$

where e is the eccentricity.

This is used to calculate the orbital angular velocity as in [Ziegler, 2003]:

$$\dot{\theta} = \frac{\sqrt{\mu} (1 + e \cos \theta)^2}{SLR^{\frac{3}{2}}} \quad (5.30)$$

While deploying the tether, the orbital parameter θ does not adversely affect the dynamics of the tether deployment. As shown in Figure 5.14b, the key deployment metrics – the smooth deployment of the entire tether length and a progressive increase in stress over time – are realised. When the parameters for the circular and elliptical are compared, the parameters share much in common. When comparing the tether length with angular velocity, for example, Figures 5.14b and 5.6b are almost identical.

Similarly, when the recovery of the tether undergoing a elliptical orbit is analysed, the solutions to the equations of motion present a similar result. The length and angular velocity are very similarly matched over the two cases, as is shown when comparing Figures 5.15b and 5.9b.

5.9 Centre of mass movement

Additional stresses may be exerted on the tether by centre of mass movement. This movement causes the root of the tether to librate along the orbital path, subjecting the tether to additional loading.

The movement of the centre of mass is shown in Figure 5.16 for the deployment cases and Figure 5.17 for the recovery case. The movement of the centre of mass with respect to the facility mass is given by Equation 5.4.

The maximum movement of the CoM, for the deployment cases, are 0.07 m and 0.0017 m – the latter is the discretized mass model using exponential torque. The effort expended to model the tether mass in more detail has stripped back a layer of conservatism, and shown that the centre of mass movement is minimal. This reinforces the earlier findings of the rotation and length generalised coordinates; the symmetrical angle of the tethers and the equal lengths of the tethers both contribute to a very symmetrical system.

The maximum movement of the CoM for the recovery case is an order of magnitude greater, at 0.7 m for the first phase and 0.08 m for the second phase. This is due to the starting assumption of asymmetrical tether angles: $\psi_1[0] = 0.01^\circ$ and $\psi_2[0] = 180.1^\circ$.

Whereas the difference in the tether angle in Figure 5.6c at full deployment tends to zero, the initial conditions to recover the tether are asymmetrical. This is an allowance for the payload release, which is an unknown quantity in MMET dynamics. Therefore, an initial asymmetry of 0.1° and 0.01° was chosen to investigate the recovery dynamics. To remedy this unknown, a separation study is recommended, to fully investigate the effects that a symmetrical (or asymmetrical) dual release have on the tethers, however this is outside the scope of this document.

On further examination, the graphs of the magnitude of position and acceleration were plotted against time, and are show in Figures 5.18a and 5.18b.

The maximum acceleration, due to the moving CoM, encountered in the recovery phase is approximately 0.8 m/s^2 , therefore the force exerted by the moving centre of mass, given a total system mass of $10 + 10 + 100 + 100 + 500 = 720 \text{ kg}$ is:

$$F = ma = 0.8 * 720 = 576 \text{ N} \quad (5.31)$$

Given this is several orders of magnitude less than the tether tension of $110,000 \text{ N}$ in Figure 5.10a, it does not present a significant risk to the tether. Indeed, it explains the slight high frequency tension superimposed on the overall smooth downward trend shown in that figure.

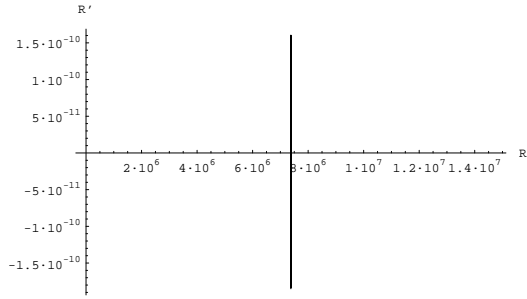
On payload release, the likelihood of a small tether asymmetry may be significant. Removing this asymmetry, insofar as possible, could be achieved by repeated cycling of short recovery and deployment phases, or an active control system on the payload release mechanism.

5.10 Conclusions

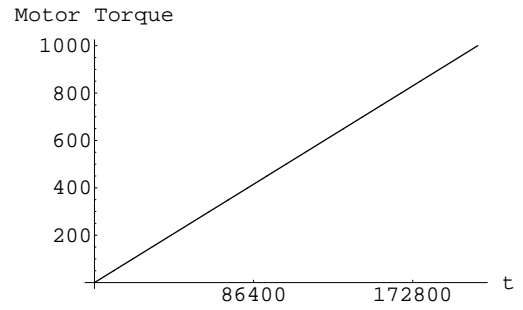
Deploying and recovering the tethers on the MMET system is not a trivial matter; however, they can be achieved in a well controlled and structured way.

A method for deployment and recovery in the orbital plane have been outlined, giving confidence that the MMET is capable and suitable for use as a reusable launch platform.

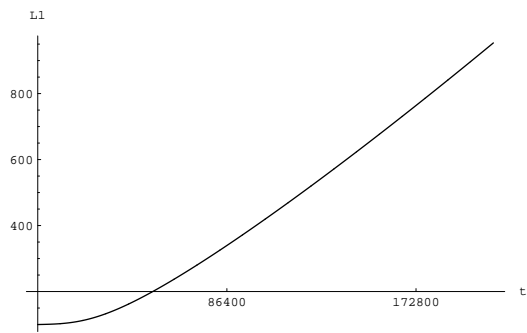
5.11 Figures



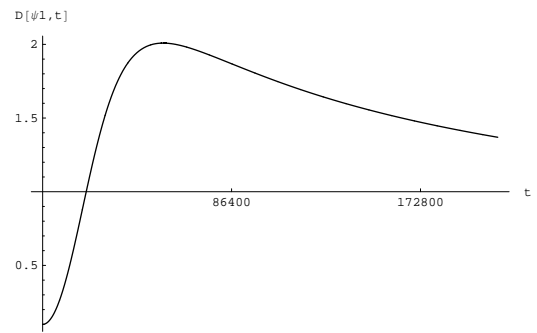
(a) Phase plot: radius velocity \dot{R} (m/s) vs. radius of CoM R (m)



(b) Applied motor torque τ (Nm) vs. time t (s)



(c) Tether 1 length L_1 (m) vs. time t (s)



(d) Tether 1 rotational velocity $\dot{\psi}_1$ (rad/s) vs. time t (s)

Figure 5.2: Initial MMET Spin-up

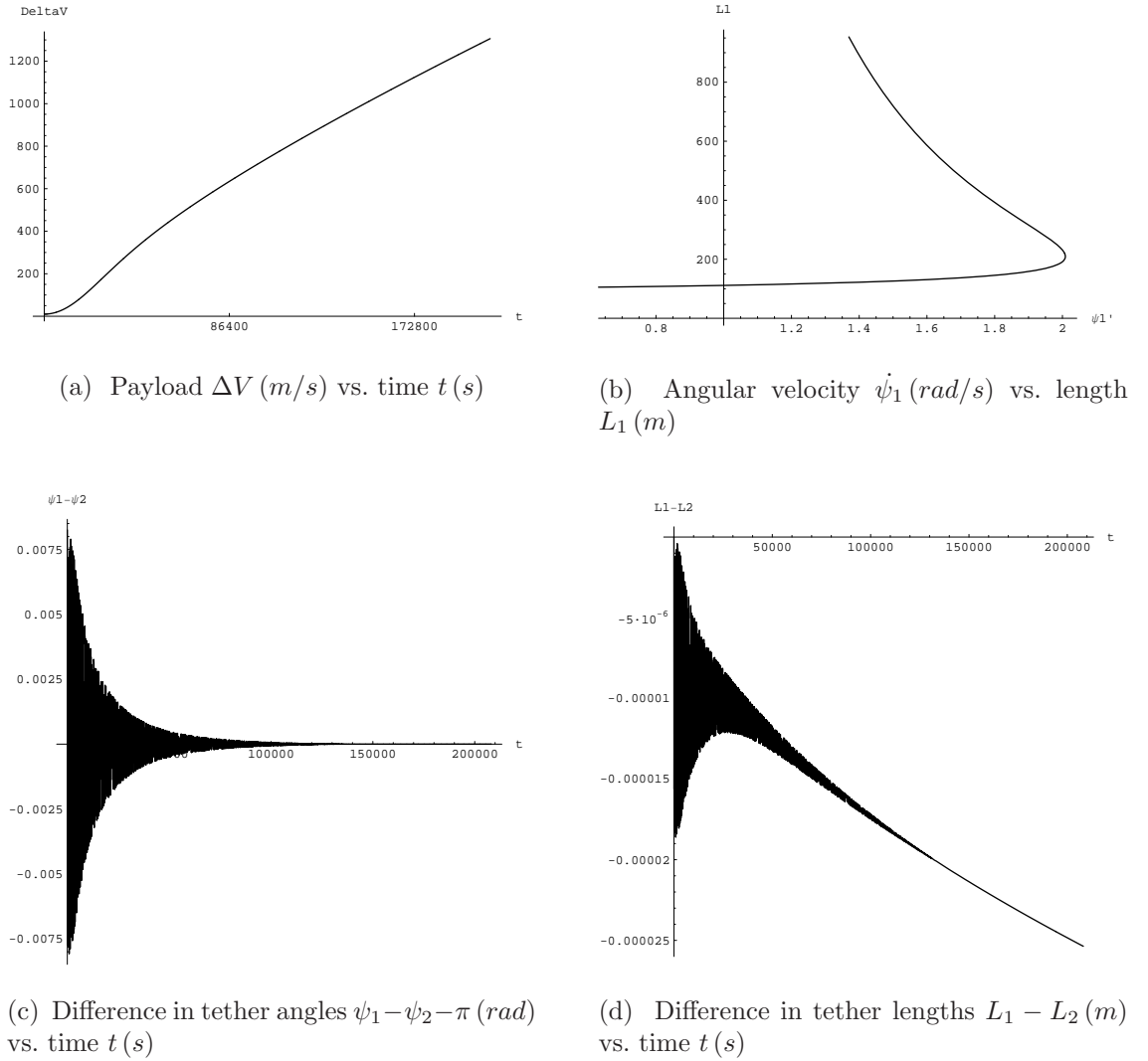


Figure 5.3: Initial MMET Spin-up

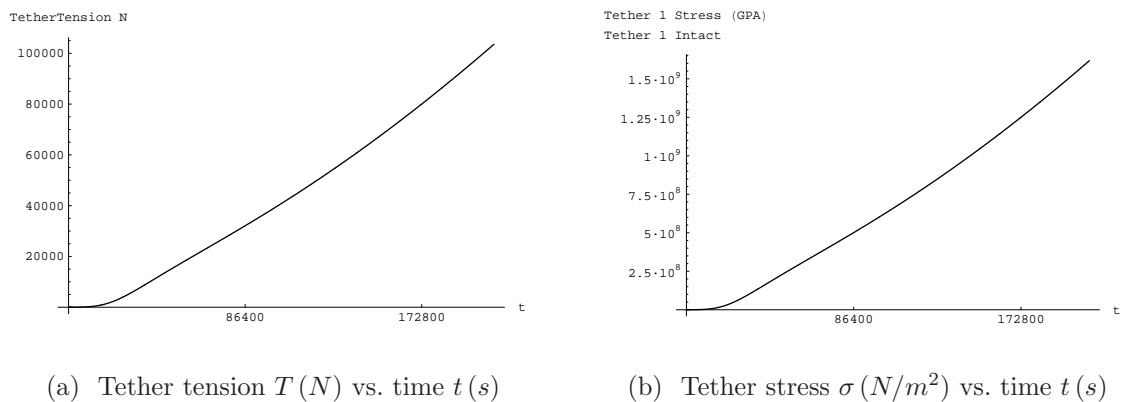


Figure 5.4: Initial MMET Spin-up

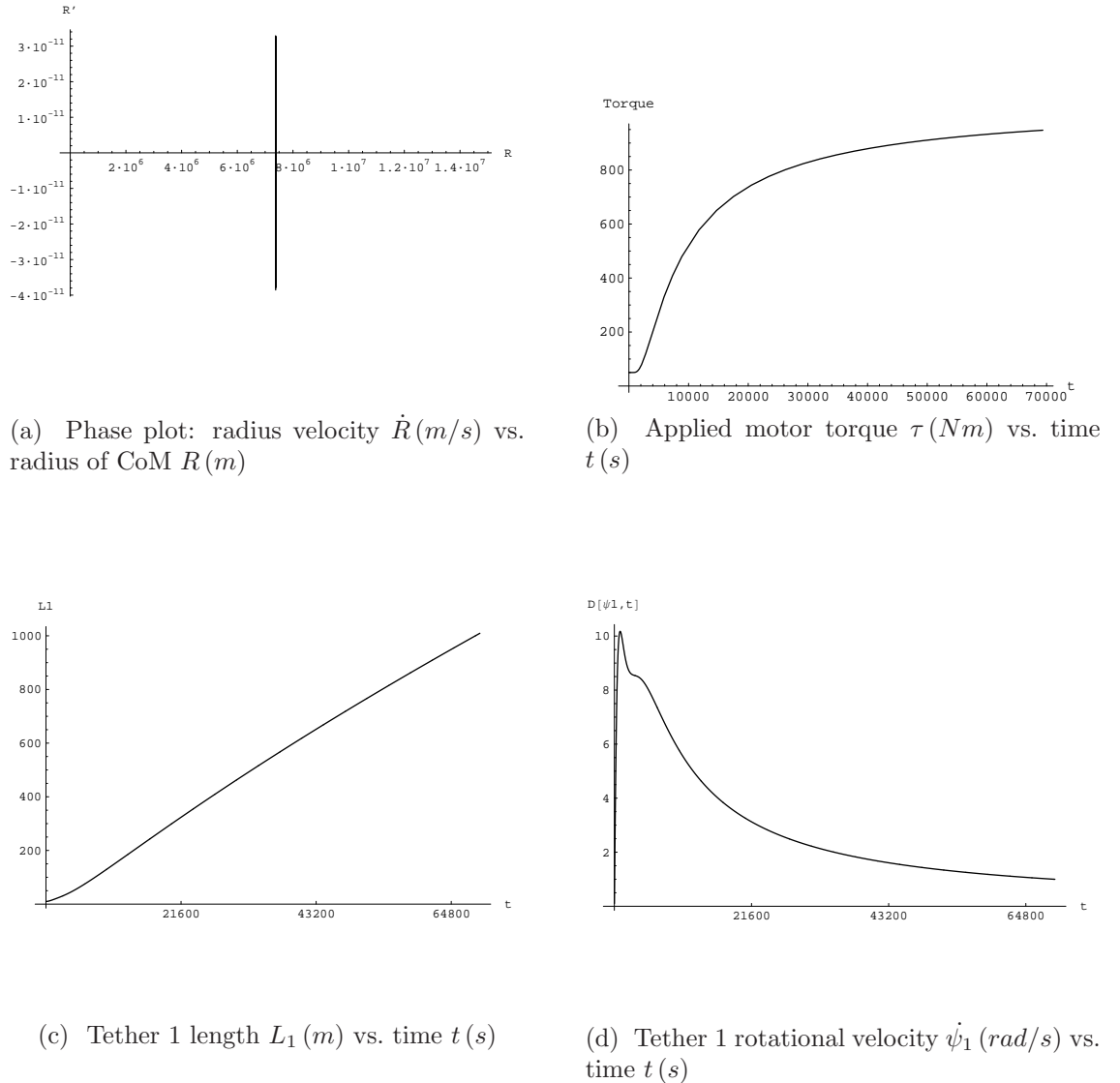


Figure 5.5: Initial MMET Spin-up, discretized tether mass model

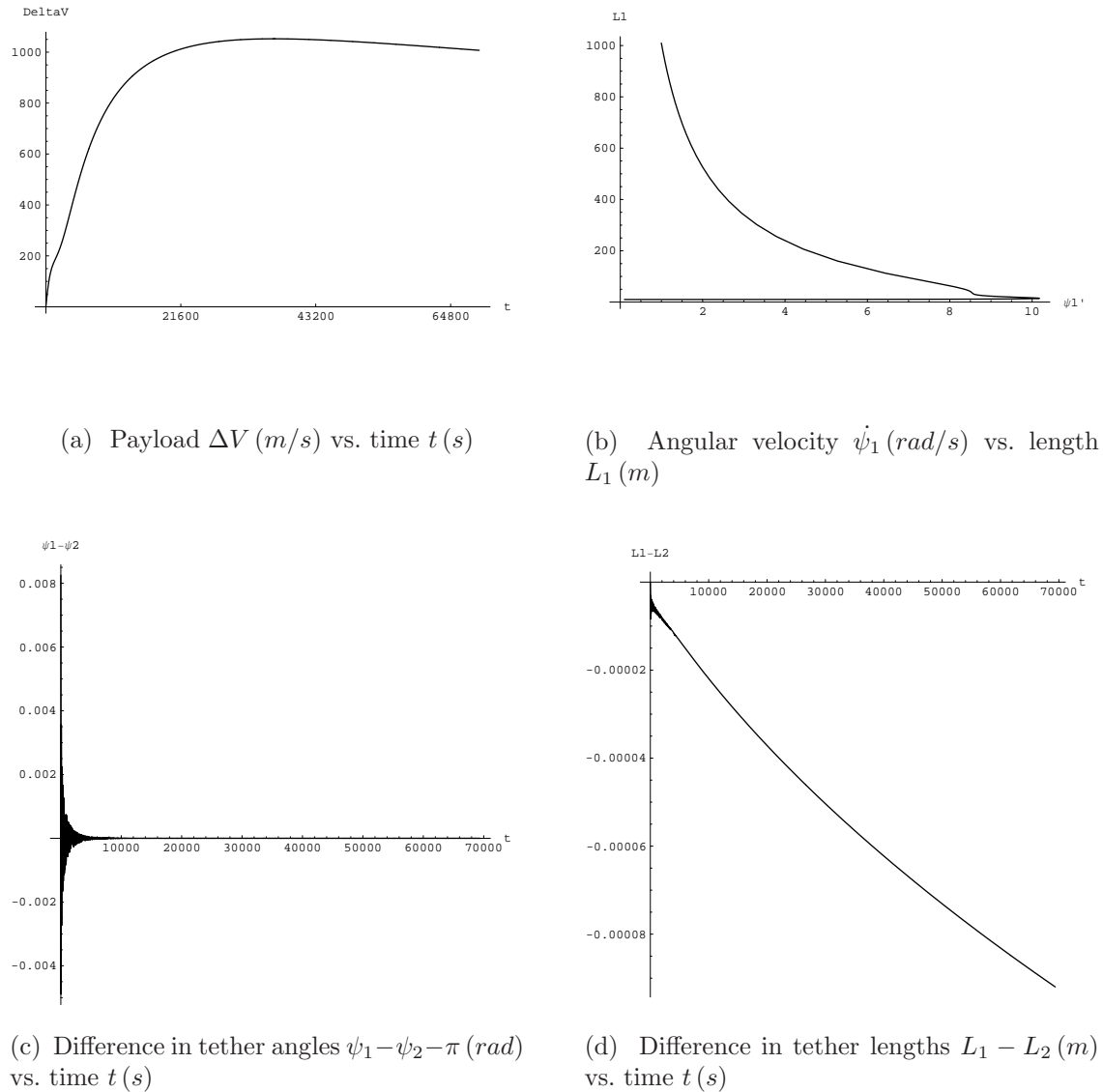
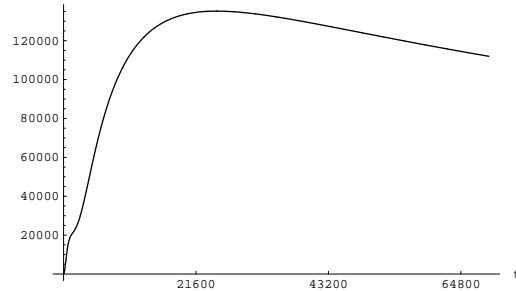


Figure 5.6: Initial MMET Spin-up, discretized tether mass model

TetherTension N



Tether 1 Stress (GPA)

Tether 1 Intact

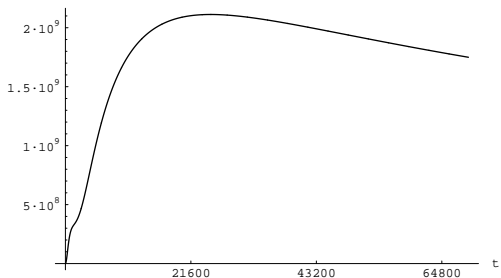
(a) Tether tension T (N) vs. time t (s)(b) Tether stress σ (N/m^2) vs. time t (s)

Figure 5.7: Initial MMET Spin-up, discretized tether mass model

L1

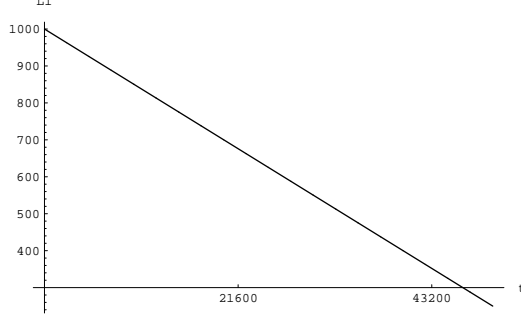
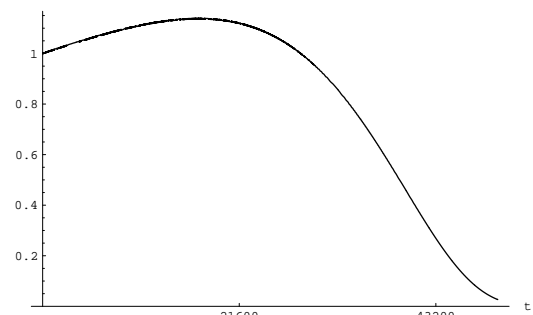
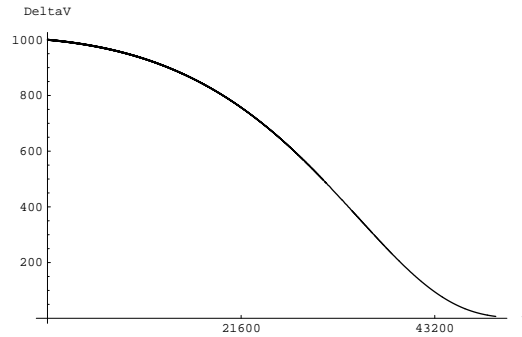
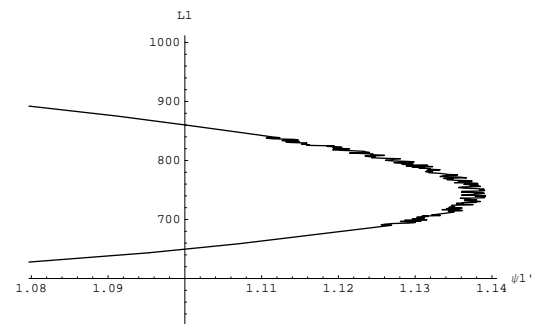
 $D[\psi_1, t]$ (a) Tether 1 length L_1 (m) vs. time t (s)(b) Tether 1 rotational velocity $\dot{\psi}_1$ (rad/s) vs. time t (s)

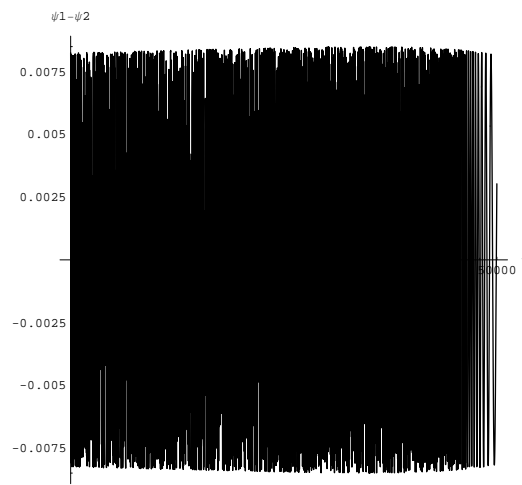
Figure 5.8: MMET reel in, first phase



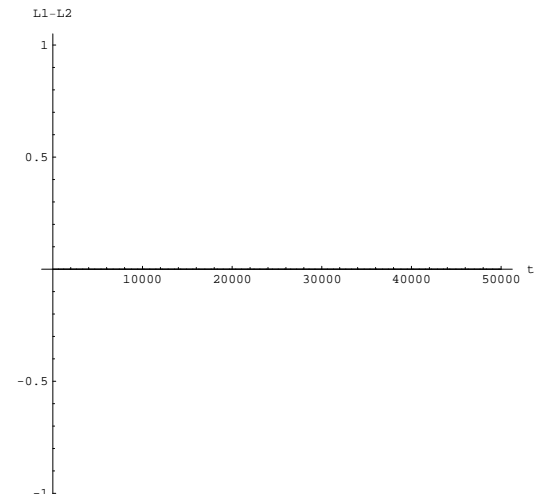
(a) Payload ΔV (m/s) vs. time t (s)



(b) Angular velocity $\dot{\psi}_1$ (rad/s) vs. length L_1 (m)

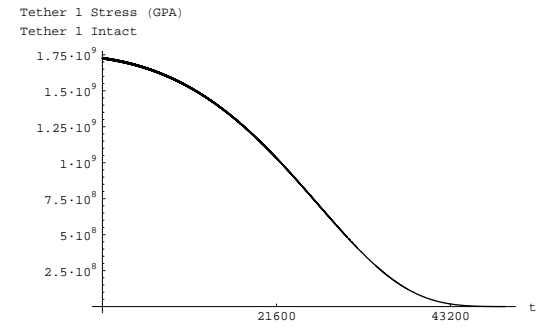
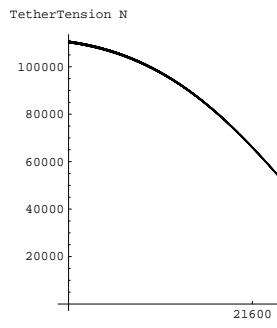


(c) Difference in tether angles $\psi_1 - \psi_2 - \pi$ (rad) vs. time t (s)



(d) Difference in tether lengths $L_1 - L_2$ (m) vs. time t (s)

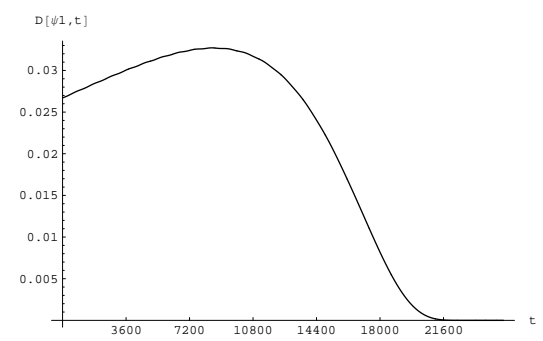
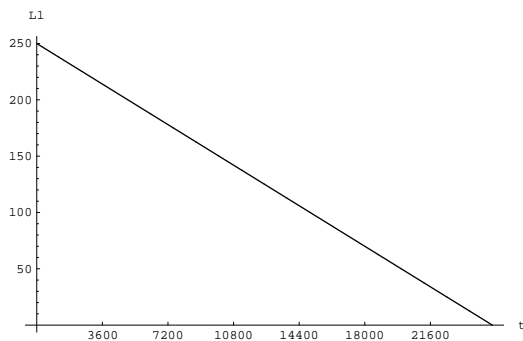
Figure 5.9: MMET reel in, first phase



(a) Tether tension T (N) vs. time t (s)

(b) Tether stress σ (N/m^2) vs. time t (s)

Figure 5.10: MMET reel in, first phase

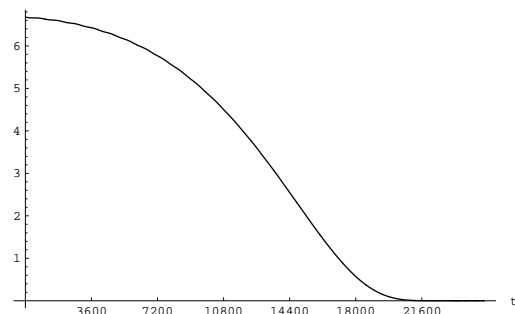


(a) Tether 1 length L_1 (m) vs. time t (s)

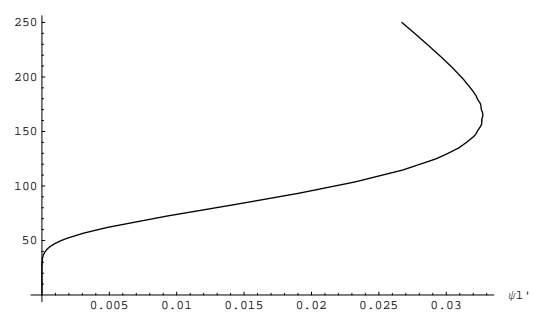
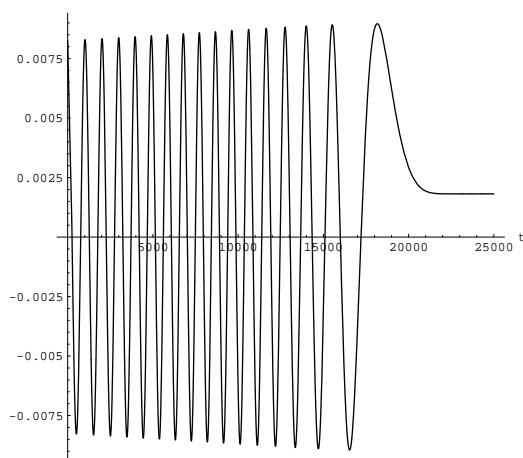
(b) Tether 1 rotational velocity $\dot{\psi}_1$ (rad) vs. time t (s)

Figure 5.11: MMET reel in, second phase

DeltaV

(a) Payload ΔV (m/s) vs. time t (s)

L1

(b) Angular velocity $\dot{\psi}_1$ (rad/s) vs. length L_1 (m) $\psi_1 - \psi_2$ (c) Difference in tether angles $\psi_1 - \psi_2 - \pi$ (rad) vs. time t (s)

L1-L2

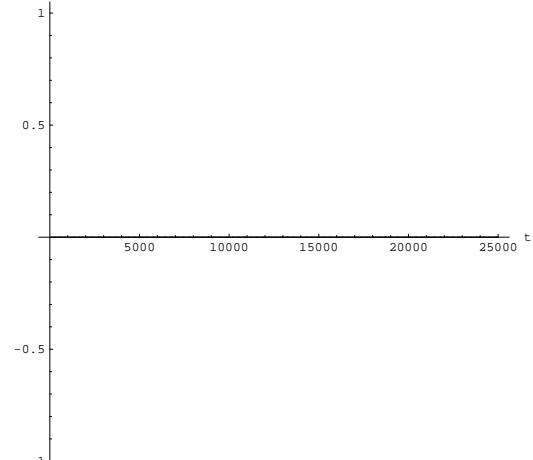
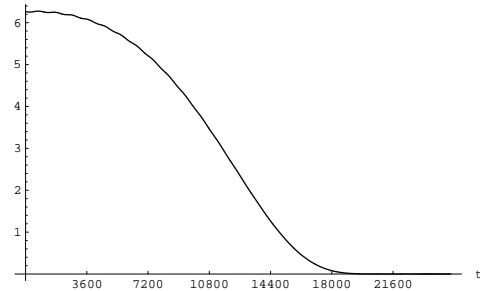
(d) Difference in tether lengths $L_1 - L_2$ (m) vs. time t (s)

Figure 5.12: MMET reel in, second phase

TetherTension N



Tether 1 Stress (GPA)

Tether 1 Intact

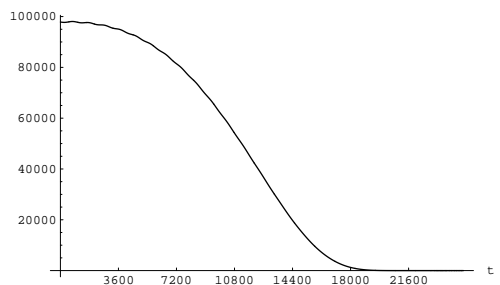
(a) Tether tension T (N) vs. time t (s)(b) Tether stress σ (N/m^2) vs. time t (s)

Figure 5.13: MMET reel in, second phase

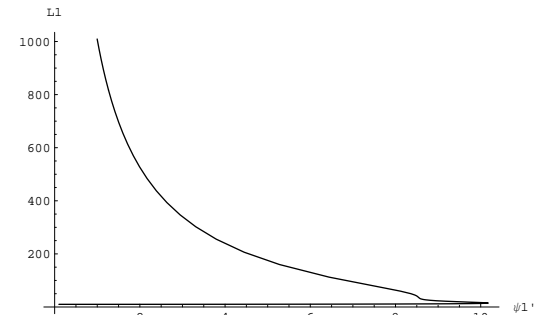
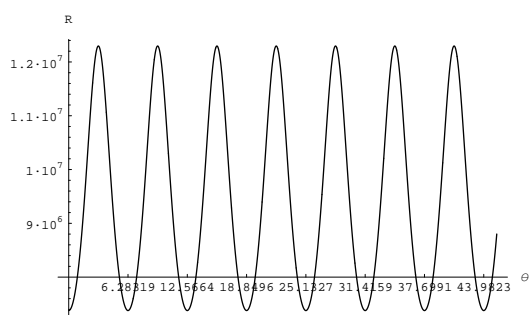
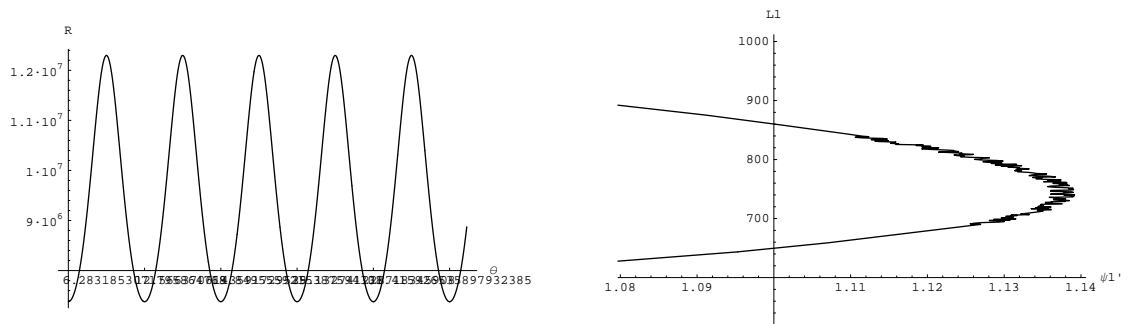
(a) Orbital radius R (m) vs. orbital angle θ (rad)(b) Angular velocity $\dot{\psi}_1$ (rad/s) vs. length L_1 (m)

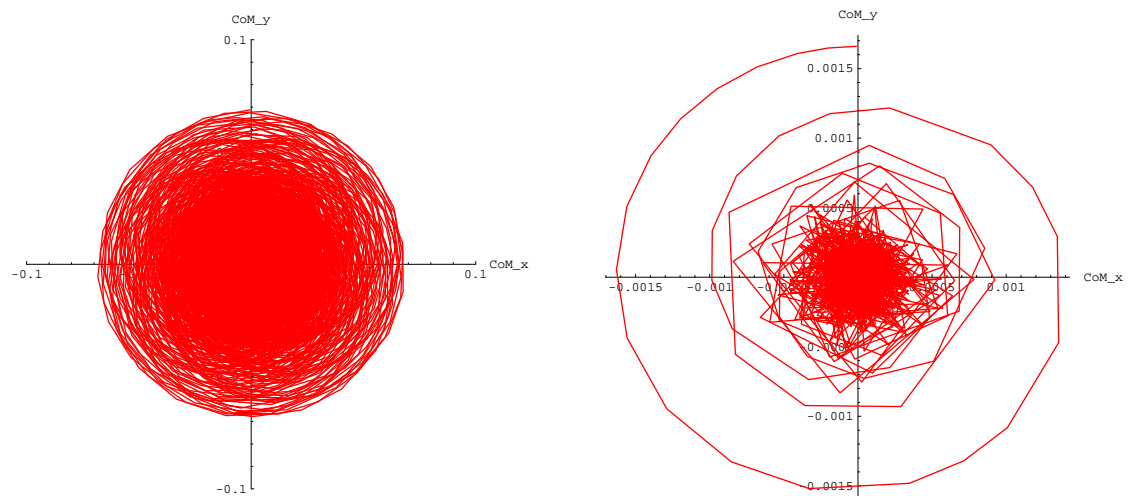
Figure 5.14: MMET deployment with elliptical orbit



(a) Orbital radius $R(m)$ vs. orbital angle $\theta(rad)$

(b) Angular velocity $\dot{\psi}_1(rad/s)$ vs. length $L_1(m)$

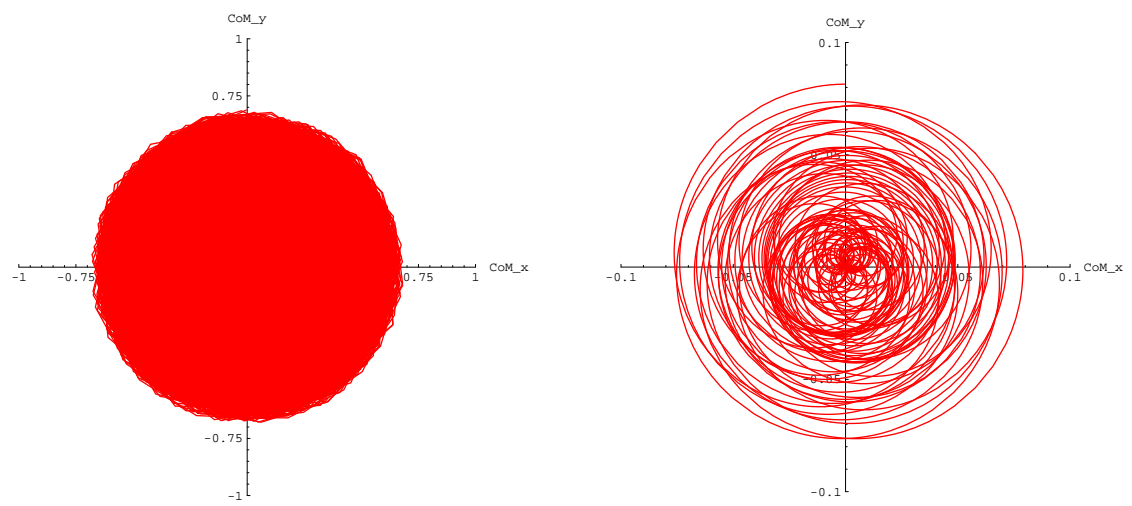
Figure 5.15: MMET recovery with elliptical orbit



(a) Centre of mass position, linear mass model

(b) Centre of mass position, discretized mass model

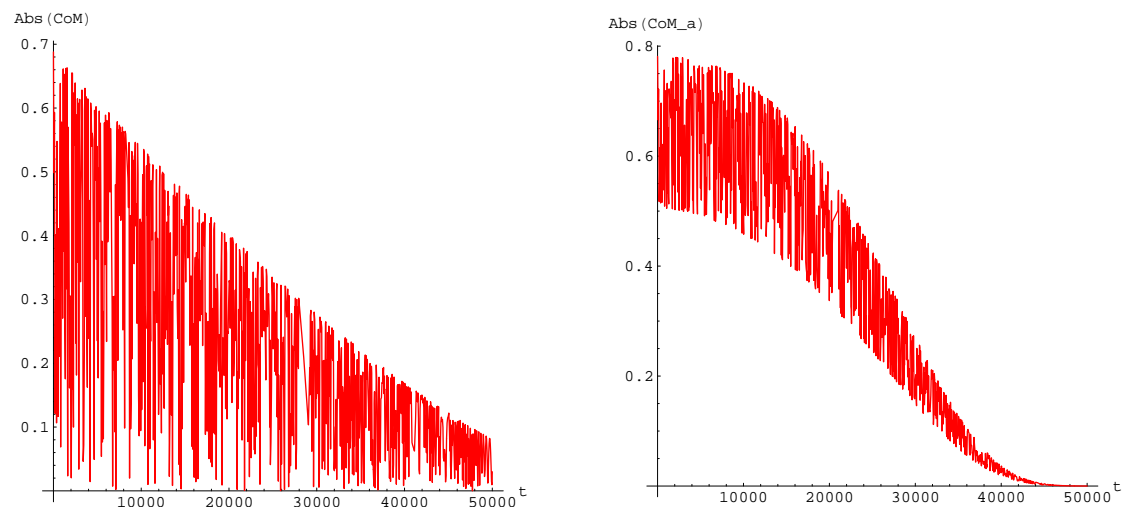
Figure 5.16: MMET deployment, centre of mass movements



(a) Centre of mass position, discretized mass model, first stage

(b) Centre of mass position, discretized mass model, second phase

Figure 5.17: MMET recovery, centre of mass movements



(a) Absolute position of CoM, discretized mass model, first phase

(b) Absolute acceleration of CoM, discretized mass model, first phase

Figure 5.18: MMET recovery, position and acceleration of centre of mass

5.11.1 Linear kinetic energy

The linear kinetic energy of the MMET with length deployment and ten discrete tether masses, expanded from the analytical version in Equation 5.12, is as follows:

$$\begin{aligned}
T_{\text{trans}} = & M_{\text{tether}}(11M_1(M_2 + M_{\text{facility}}) + 145M_1M_{\text{tether}} + 5M_{\text{tether}}(7(M_2 + M_{\text{facility}}) + 85M_{\text{tether}}))\dot{L}_1^2 + (11M_2(M_1 + M_{\text{facility}}) \\
& + 5(7M_1 + 29M_2 + 7M_{\text{facility}})M_{\text{tether}} + 425M_{\text{tether}}^2)\dot{L}_2^2 + 11M_1^2\dot{R}^2 + 22M_1M_2\dot{R}^2 + 11M_2^2\dot{R}^2 + 22M_1M_{\text{facility}}\dot{R}^2 + 22M_2M_{\text{facility}}\dot{R}^2 \\
& + 11M_{\text{facility}}^2\dot{R}^2 + 440M_1M_{\text{tether}}\dot{R}^2 + 440M_2M_{\text{tether}}\dot{R}^2 + 440M_{\text{facility}}M_{\text{tether}}\dot{R}^2 + 4400M_{\text{tether}}^2\dot{R}^2 + 11M_1^2R^2\dot{\theta}^2 + 22M_1M_2R^2\dot{\theta}^2 \\
& + 11M_2^2R^2\dot{\theta}^2 + 22M_1M_{\text{facility}}R^2\dot{\theta}^2 + 22M_2M_{\text{facility}}R^2\dot{\theta}^2 + 11M_{\text{facility}}^2R^2\dot{\theta}^2 + 440M_1M_{\text{tether}}R^2\dot{\theta}^2 + 440M_2M_{\text{tether}}R^2\dot{\theta}^2 \\
& + 440M_{\text{facility}}M_{\text{tether}}R^2\dot{\theta}^2 + 4400M_{\text{tether}}^2R^2\dot{\theta}^2 + 22(M_1 + 5M_{\text{tether}})(M_2 + 5M_{\text{tether}})L_1 \sin(\psi_1 - \psi_2)\dot{L}_2\dot{\psi}_1 \\
& + 11M_1M_2L_1^2\dot{\psi}_1^2 + 11M_1M_{\text{facility}}L_1^2\dot{\psi}_1^2 + 145M_1M_{\text{tether}}L_1^2\dot{\psi}_1^2 + 35M_2M_{\text{tether}}L_1^2\dot{\psi}_1^2 + 35M_{\text{facility}}M_{\text{tether}}L_1^2\dot{\psi}_1^2 + 425M_{\text{tether}}^2L_1^2\dot{\psi}_1^2 \\
& - 22(M_1 + 5M_{\text{tether}})(M_2 + 5M_{\text{tether}})\cos(\psi_1 - \psi_2)L_1L_2\dot{\psi}_1\dot{\psi}_2 + (11M_2(M_1 + M_{\text{facility}}) + 5(7M_1 + 29M_2 + 7M_{\text{facility}})M_{\text{tether}} \\
& + 425M_{\text{tether}}^2)L_2^2\dot{\psi}_2^2 - 22(M_1 + 5M_{\text{tether}})(M_2 + 5M_{\text{tether}})\dot{L}_1(\cos(\psi_1 - \psi_2)\dot{L}_2 + L_2 \sin(\psi_1 - \psi_2)\dot{\psi}_2)22(M_1 + M_2 + M_{\text{facility}} + 20M_{\text{tether}})
\end{aligned} \tag{5.32}$$

Chapter 6

Dynamics of space-webs

This chapter was funded as part of the ESA Ariadna study into space-webs; the final report was presented as [McKenzie et al., 2006]. The author wishes to acknowledge the hard work and contributions to this report from M.P Cartmell and M. Vasile of the University of Glasgow and D. Izzo of the ESA ACT.

6.1 Introduction

As was outlined in Section 2.3, a generic satellite that may be constructed or re-configured as needed is a useful concept. Studies have previously shown that robots may be deployed in this way to reconfigure the net structure [Kaya et al., 2004a], [Nakano et al., 2005].

This chapter will consider the fundamental conceptual design of an appropriate and generic thin membrane, its orbital mechanics and control.

A model of a net in orbit is presented here, with robots moving along the surface of the net, simulating reconfiguration of the system. Useful guidelines to the initial conditions of the net and components are found and give a starting point for further

studies into the field.

This new class of structures with robots moving over the surface will be defined as ‘Space-webs’, with the robots correspondingly named ‘Spiderbots’. A concept illustration of the idea is shown in Figure 6.1.

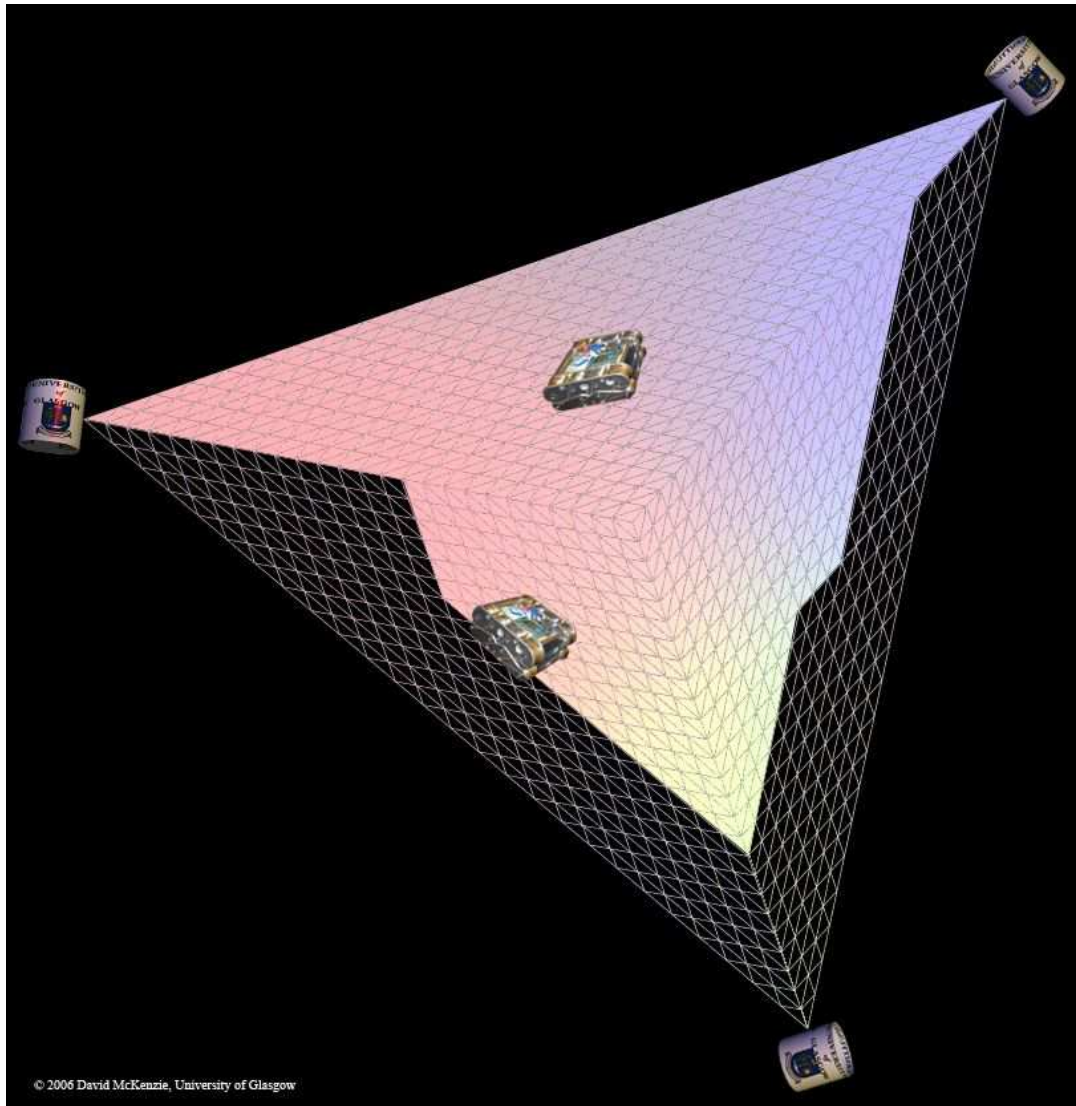


Figure 6.1: Concept rendering of the space-web with spiderbots on the surface.

Space-webs have one definite advantage over single use spacecraft: the ability to reconfigure the web to suit the mission or environment. Due diligence must therefore be observed to ensure that the act of reconfiguring the web does not endanger the web or satellite. Investigating the movement of the robots while moving over the web is essential: the movement of their mass and momentum may significantly affect

the web dynamics.

The stability of the system is investigated while the robots crawl along the web surface in two pre-defined motions:

- Three robots simultaneously moving along the outer catenaries of the web
- Three robots simultaneously moving from the centre to the outside of the web

6.2 Modelling methodology

This study will aim to develop an analytical model of the fully deployed space-web system that may be numerically integrated.

When constructing a numerical simulation of an existent system, it is important to consider that the simulation can only be said to represent a real life scenario when the model has been validated and the initial conditions used in the calculation are representative of the simulation scenario.

This may seem like an obvious statement, but these facts are often overlooked for convenience or speed.

In modelling the space-web, it is important to make the modelling process transparent and verifiable. In this spirit, the steps followed to assemble the space-web model are outlined paying particular attention to the steps followed to produce a model in *Mathematica* and the process of validating the model against previous models and the real life case where possible.

6.3 Web meshing

6.3.1 Web structure

To gain an accurate estimate of the energy of the web, the mass distribution over the web is discretized [Ziegler, 2003]. An algorithm has been designed in *Mathematica* to take the triangle bounded by the i^{th} sub-span, the $(i + 1)^{th}$ sub-span and the facility mass and divide this into equally sized smaller triangles.

The space-web is modelled as s sub-spans, clustered around the central facility mass. Each sub-span is considered to be rigid and massless, held rigid by the centripetal force of rotation around the centre of mass. An idealized point mass m_i is placed at the end of the sub-span, at length l_i , with the position of each endpoint mass given by $P_{i_{\text{local}}}$ in Equations 6.5, 6.6. In this form, this is very similar to the tethers previously modelled, the differences are multiple sub-spans and massless tethers.

The web is stretched between the sub-spans i and $i + 1$ and replicated to give s triangular webs. Each triangular web section is idealised as an elastic plane containing the mass of that section, however the internal elastic forces within the web are not modelled at this stage.

6.3.2 Dividing the web

Each web section is divided into n equal sections (referred to here as ‘divisions’), in the direction given by the line joining the midpoint of the sub-span ends and the facility, as represented in Figures 6.2 to 6.4.

For each of the n web sections;

$$\begin{aligned}
\text{triangles} &= (n+1)^2 \\
\text{triangles in top row} &= 2n+1 \\
\text{row configuration} &= \{2n+1, 2(n-1)+1, \\
&\quad 2(n-2)+1, \dots, 3, 1\} \\
\text{number of rows} &= n+1 \\
\text{nodes} &= \frac{1}{2}(n+2)(n+3) \\
\text{midpoints} &= (n+1)^2
\end{aligned}$$

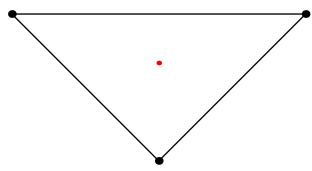


Figure 6.2: 0 divisions

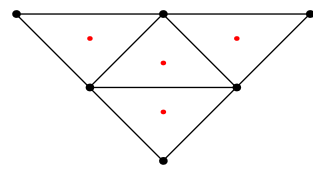


Figure 6.3: 1 division

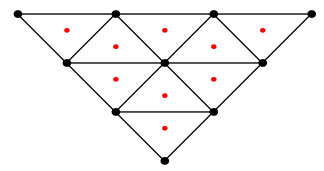


Figure 6.4: 2 divisions

6.3.3 Web divisions

A point mass is placed at each mid-point, therefore the total number of masses for the webs are $s(n+1)^2$, where s is the number of sub-spans. That is to say, the number of masses in the web increases as the square of the number of divisions. This can lead to a very large number of mass points to consider for a fine-grain web.

Assembling the space-web with three sub-spans ($n = 3$) and 0 divisions gives the layout shown in Figure 6.5, with Figure 6.6 showing the same layout with 1 division, and finally Figure 6.7 shows the same layout with 2 divisions. Each red dot is a mass-point on the web.

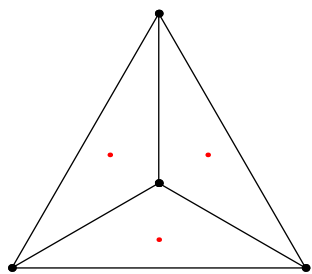


Figure 6.5: 3 sub-spans
– 0 divs

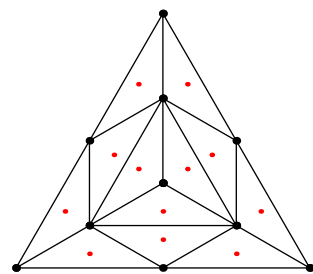


Figure 6.6: 3 sub-spans
– 1 div

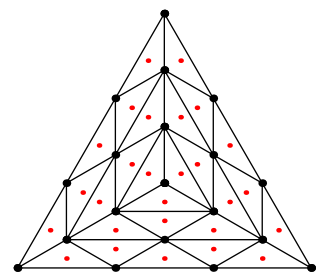


Figure 6.7: 3 sub-spans
– 2 divs

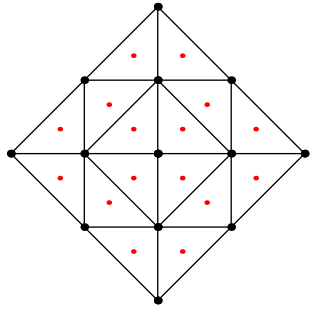


Figure 6.8: 4 sub-spans
– 1 div

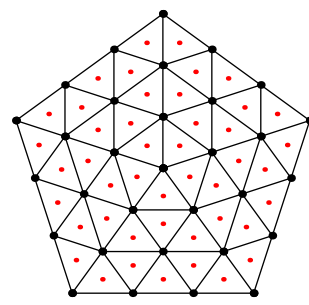


Figure 6.9: 5 sub-spans
– 2 divs

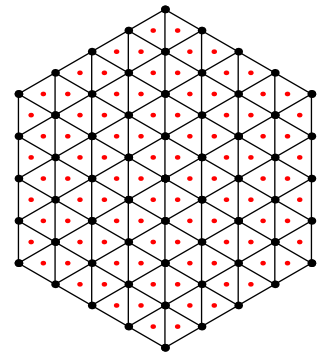


Figure 6.10: 6 sub-spans – 3 divs

The space-web layout may be expanded to analyse different web configurations. A square layout with 1 division per section is shown in Figure 6.8; a pentagonal layout with 2 divisions per section is shown in Figure 6.9; and a hexagonal layout with 3 divisions per section is shown in Figure 6.10 with total of 103 masses¹.

6.4 Equations of motion

6.4.1 Centre of mass modelling

The mass of the web is likely to be unevenly distributed. Modelling this requires an expression for the centre of mass (CoM) position, in this case using the facility mass as the origin.

For n masses with positions $\{X_i, Y_i, Z_i\}$, the position of the centre of mass about the facility, in terms of the local $\{X, Y, Z\}$ coordinate system centred on the facility mass, is:

$$P_{facility \rightarrow CoM} \left\{ \frac{\sum_{i=1}^n M_i X_i}{\sum_{i=1}^n M_i}, \frac{\sum_{i=1}^n M_i Y_i}{\sum_{i=1}^n M_i}, \frac{\sum_{i=1}^n M_i Z_i}{\sum_{i=1}^n M_i} \right\} \quad (6.1)$$

This is used when taking the position *from* the centre of mass *to* the facility mass, as $P_{CoM \rightarrow facility} = -P_{facility \rightarrow CoM}$

¹103 masses = 96 web midpoints + 6 sub-span masses + 1 central facility mass.

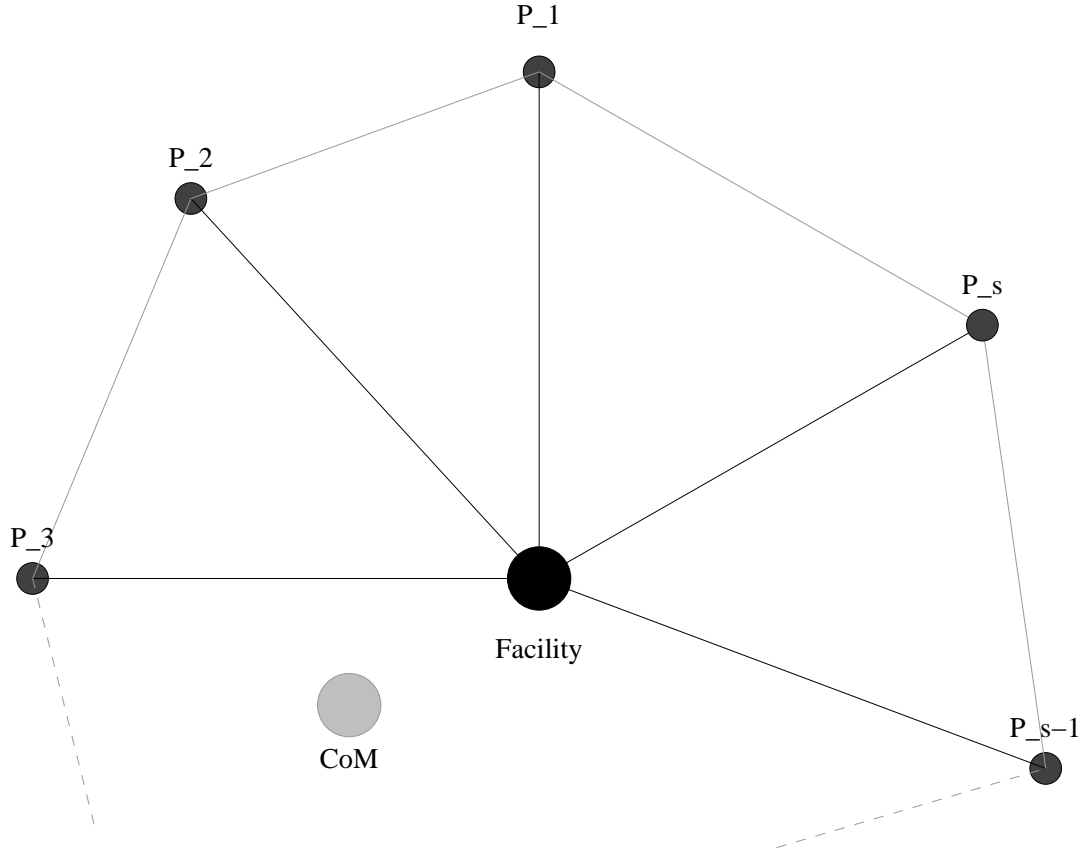


Figure 6.11: Simplified space-web layout with s sub-spans

6.4.2 Rotations

Rotational matrices are used to rotate the starting vectors to their positions on the local and inertial planes. The local position vector in Equation 6.5 is the matrix product of a series of rotations. A diagram of the space-web configuration is shown in Figure 6.13 with the web removed for clarity.

$$R_{\psi_i, \text{X}} = \begin{bmatrix} 1 & 0 & 0 \\ 0 & \cos(\psi_i) & -\sin(\psi_i) \\ 0 & \sin(\psi_i) & \cos(\psi_i) \end{bmatrix} \quad (6.2)$$

$$R_{\alpha_i, \text{Y}} = \begin{bmatrix} \cos(\alpha_i) & 0 & \sin(\alpha_i) \\ 0 & 1 & 0 \\ -\sin(\alpha_i) & 0 & \cos(\alpha_i) \end{bmatrix} \quad (6.3)$$

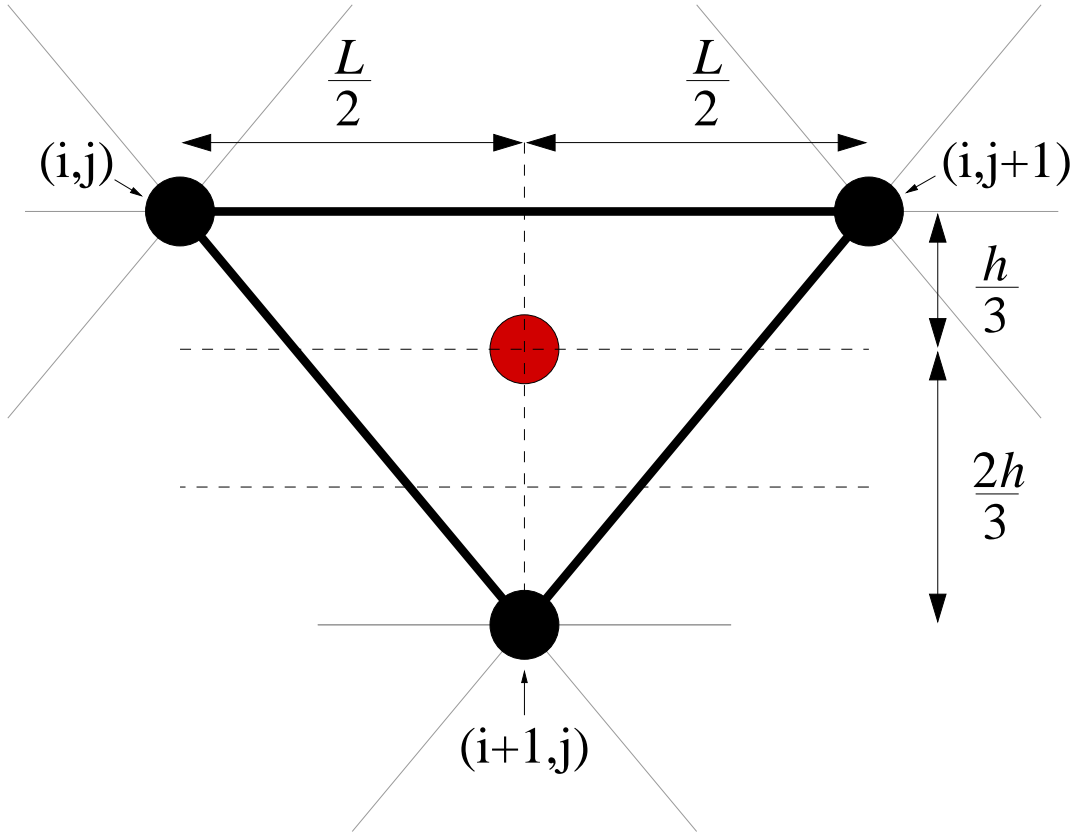


Figure 6.12: Midpoint location

$$R_{\phi_i, Z} = \begin{bmatrix} \cos(\phi_i) & -\sin(\phi_i) & 0 \\ \sin(\phi_i) & \cos(\phi_i) & 0 \\ 0 & 0 & 1 \end{bmatrix} \quad (6.4)$$

$$P_{i_{\text{Local}}} = R_{\psi_i, X} \cdot R_{\alpha_i, Y} \cdot R_{\phi_i, Z} \cdot L_i \quad (6.5)$$

where $L_i = \{0, 0, l_i\}^T$, aligned along the local Z-axis

$$P_{i_{\text{inertial}}} = R_{\theta, Z} (P_{0 \rightarrow \text{CoM}} - P_{\text{facility} \rightarrow \text{CoM}} + (R_{\psi_i, X} \cdot R_{\alpha_i, Y} \cdot R_{\phi_i, Z} \cdot L_i)) \quad (6.6)$$

Rotations may be performed using the rotation order Z then Y then X :

The sub-span is rotated around the facility by an angle ψ with the axis of rotation in the X-axis only. This vector is then rotated around the facility by an angle α with the axis of rotation in the Y-axis only. Finally, this vector is then rotated around the facility by an angle ϕ with the axis of rotation in the Z-axis only.

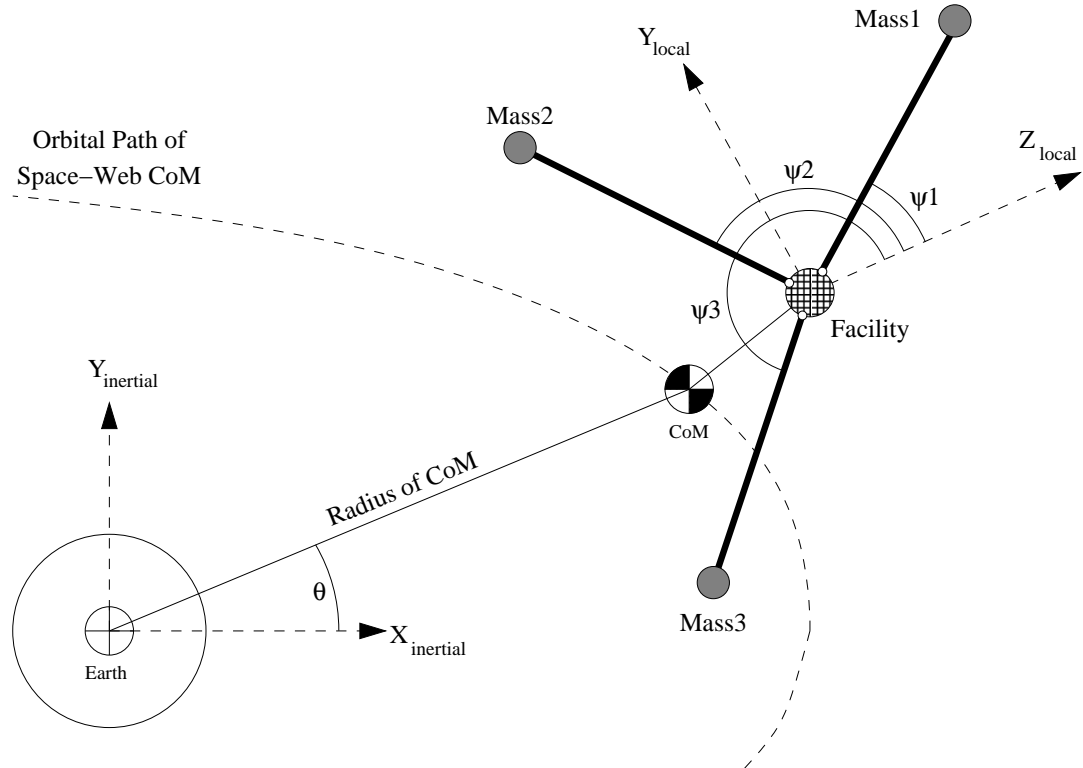


Figure 6.13: Space-web diagram with 3 sub-spans shown in inertial space. Note: the local axes are in the Y-Z plane.

The angles are projected about their respective axes i.e., the Z-rotation, ϕ , is contained in the $X - Y$ plane. The angles themselves can be compared to the standard aerospace rotations, with the sub-span direction from the facility to the edge taken as the tail-nose direction. In this case: ψ is the yaw angle, in the plane of the space-web; α is the pitch angle, out of the space-web plane; and ϕ is the roll angle, the twist in the sub-span.

Considering rotations about the ψ direction only – that is constraining the motion of the space-web to be in-plane – gives the following equation

$$P_{i_{\text{inertial}}} = R_{\theta, Z} (P_{0 \rightarrow \text{CoM}} - P_{\text{facility} \rightarrow \text{CoM}} + (R_{\psi_i, X} \cdot L_i)) \quad (6.7)$$

Where $P_{0 \rightarrow \text{CoM}} = \{R, 0, 0\}$, and represents the position of the centre of mass from Earth.

6.4.3 Position equations

The positions of the masses in the local coordinate system must be translated and rotated into the inertial (Earth centred) coordinate system. The local position vectors are added to the position vector from the CoM to the facility and the position vector from the Earth to the CoM. The resultant vector is then rotated into the Earth centred Inertial axis system.

6.5 Energy modelling

For every mass point in the system with position in the inertial frame, P_i , the following steps are undertaken in order to find the Lagrangian energy expression \mathbb{L} :
the respective velocities, V_i are found:

$$V_i = \frac{\partial}{\partial t} P_i \quad (6.8)$$

the kinetic energies (linear T_{lin} and rotational T_{rot}) are obtained and summed:

$$T_{\text{lin}} = \sum_{i=1}^n \frac{1}{2} m_i V_i \cdot V_i \quad (6.9)$$

$$T_{\text{rot}} = \sum_{i=1}^n m_i \frac{1}{2} P_{i_{\text{local}}} \cdot P_{i_{\text{local}}} \left(\frac{\dot{\psi}_1 + \dot{\psi}_2 + \dot{\psi}_3}{3} \right)^2 \quad (6.10)$$

the potential energies, U , are obtained and summed:

$$U = \sum_{i=1}^n \frac{\mu m_i}{\sqrt{P_i \cdot P_i}} \quad (6.11)$$

and the Lagrangian is found:

$$\mathbb{L} = T_{\text{rot}} + T_{\text{lin}} - U \quad (6.12)$$

The moment of inertia of each mass point on the web is calculated using the parallel axis theory about the central facility, then multiplied by the square of the average angular velocities of the three sub-spans to give the rotational kinetic energy.

The average angular velocity of the three sub-spans, as shown in Equation 6.13, was chosen in preference to the actual calculated angular velocities of each mass point to simplify the Lagrangian energy expression and to lighten the computational load. Instead of 27 individual angular velocities, every mass point on the web was assumed to have one common angular velocity. There is an error in this assumption, but this will be acceptably small because the actual velocity is approximately equal to the average velocity.

$$\left(\frac{\partial \psi}{\partial t} \right)_{ave} = \frac{1}{3} \left(\frac{\partial \psi_1}{\partial t} + \frac{\partial \psi_2}{\partial t} + \frac{\partial \psi_3}{\partial t} \right) \quad (6.13)$$

For each mass point, the Lagrangian energy expression is constructed by considering the total kinetic and potential energies of the system.

$$\frac{d}{dt} \left(\frac{\partial T}{\partial \dot{q}_j} \right) - \frac{\partial T}{\partial q_j} + \frac{\partial U}{\partial q_j} = Q_j \quad (6.14)$$

Lagrange's equations are generated for all the generalised coordinates as specified in Equation 6.14.

6.5.1 Virtual work terms

The elastic force the web imparts on the sub-span ends are modelled as a simple elastic tether [Miyazaki and Iwai, 2004], obeying Hooke's Law: $F = Kx$:

$$F = K \left(H \left[(P_i - P_{i+1}) - \frac{2\pi}{s} \right] \right) \quad (6.15)$$

where $H[\dots]$ is the Heaviside function.

The forces are then used to calculate the right hand side of Lagrange's equations,

Q_i , through consideration of the virtual work.

$$Q_i = -K_{sc} \Upsilon_i \frac{\partial \Upsilon_i}{q_i}; \quad (6.16)$$

where Υ_i is the difference between the sub-spans defined by the in-plane (ψ) coordinates as:

$$\Upsilon_1 = 0 \quad (6.17)$$

$$\Upsilon_2 = 0 \quad (6.18)$$

$$\begin{aligned} \Upsilon_3 = & \left(\psi_2 - \psi_1 - \frac{2\pi}{s} \right) H \left[\psi_2 - \psi_1 - \frac{2\pi}{s} \right] \\ & - \left(\psi_1 - \psi_3 - \frac{2\pi}{s} + 2\pi \right) H \left[\psi_1 - \psi_3 - \frac{2\pi}{s} + 2\pi \right] \end{aligned} \quad (6.19)$$

$$\begin{aligned} \Upsilon_4 = & \left(\psi_3 - \psi_2 - \frac{2\pi}{s} \right) H \left[\psi_3 - \psi_2 - \frac{2\pi}{s} \right] \\ & - \left(\psi_2 - \psi_1 - \frac{2\pi}{s} \right) H \left[\psi_2 - \psi_1 - \frac{2\pi}{s} \right] \end{aligned} \quad (6.20)$$

$$\begin{aligned} \Upsilon_5 = & \left(\psi_1 - \psi_3 - \frac{2\pi}{s} + 2\pi \right) H \left[\psi_1 - \psi_3 - \frac{2\pi}{s} + 2\pi \right] \\ & - \left(\psi_3 - \psi_2 - \frac{2\pi}{s} \right) H \left[\psi_3 - \psi_2 - \frac{2\pi}{s} \right] \end{aligned} \quad (6.21)$$

Note: if the angle between sub-spans 1 and 3 ($\psi_1 - \psi_3$) is examined, this would be usually be large and negative – e.g. for an equally spaced space-web. this angle would be -240° instead of 120° . Therefore to counteract this, an offset of 2π has been added to Equation 6.19 to ensure that the angle is positive and similar in size to the other sub-span angles ($\psi_2 - \psi_1$ and $\psi_3 - \psi_2$).

6.5.2 Simplifying Assumptions

To solve the full set of Lagrange's equations for this space-web system in a reasonable time on a desktop PC requires some simplifying assumptions to be made.

Firstly, five generalised coordinates are chosen defining the space web rotating in the plane normal to the radius vector: $(R, \theta, \psi_1, \psi_2, \psi_3)$. The diagram in Figure 6.13 shows the layout of the space-web, where R is the orbital radius, θ is the true anomaly, ψ_n is the angle between the n^{th} sub-span and the X_{local} coordinate system.

If the out-of-plane motion of the space-web were to be included, this would increase the number of generalised coordinates to eight, as each sub-span must have the out-of-plane motion defined.

If the space-web orbits exclusively in-plane, a simplifying assumption may be performed in terms of the potential energy expression:

$$U = \sum_{i=1}^n \frac{\mu m_i}{R} \quad (6.22)$$

6.5.3 Robot Position Modelling

Robots may move across the space-web in order to reconfigure the web or other tasks as discussed previously. To model this as an kinetic energy based term while retaining the flexibility of defining the path without hard-coding this into the equations, the robot position vector needs to be kept in a very general form.

The robot position vector in Equation 6.23 is defined similarly to Equation 6.6: a vector addition of the R vector, the CoM vector and the vector defining the local position of the robot where

$\{P_{Robot_X}, P_{Robot_Y}, P_{Robot_Z}\}_{local}$ are the local vector positions of the robot in the

X, Y, Z axes with the origin coincident on the facility mass.

$$P_{Robot_{inertial}} = R_{\theta, Z}(P_{0 \rightarrow CoM} - P_{facility \rightarrow CoM} + \{P_{Robot_X}, P_{Robot_Y}, P_{Robot_Z}\}_{local}) \quad (6.23)$$

The robot local position vector may be a function of time, position of the sub-span masses (ψ_1, ψ_2, ψ_3), an arbitrary path function or any other smooth generalised function.

The kinetic energies of the robot (both linear and rotational) are derived from the positions of the robot as before. Both the Lagrangian energy expression and Lagrange's equations contain terms for the local position, velocity, and acceleration of the robots.

Keeping the robot position functions in the most general form allows for rapid reconfiguration of the robot paths and may lead to, for example, robot control studies in the future.

6.6 Space-web dynamics

6.6.1 Dynamical simulation

The space-web dynamics are heavily governed by the centre-of-mass movement of the system. The space-web system is very rarely symmetrical (both in reality and in simulations) and this asymmetry can lead to unstable and even chaotic motion in certain configurations of the space-web.

Several different parameters were considered to be possible influences on the stability of the space-web system, including:

- variation of the masses of the web
- the masses of the robots, the sub-span and facility masses

- the position and velocity of the robots
- the general angular momentum of the robots
- the angular velocity of the web
- and the starting configuration of the web or ‘web symmetry’

Lagrange’s equations for the space-web system are solved using the *Mathematica* numerical integrator *NDSolve[...]*. The package LiveGraphics3D [Kraus, 2007] is then used to display any animated graphics in a web-browser.

Additionally, the arrows used to indicate direction in the CoM plots were generated with the CurvesGraphics6 package [Gorni, 2008] for Mathematica 5.1.

6.7 Investigating the stability of the space-web

To test the stability of the space-web with robot movement over the web, several different numerical experiments have been considered, each investigating the impact the following have on the centre of mass movement of the space-web:

- web mass
- robot mass
- web asymmetry
- robot crawl velocity

6.7.1 Mass of the web

The mass of the web was found to have a negative impact on the stability of the system. The higher the mass of the web, the more likely the triangle is to deform from the perfect equilateral shape, and the more likely the system is to exhibit

chaotic motion. This is likely to have been due to the increase in the ratio of the web mass to the other masses, causing the web mass to dominate the other mass terms. Figures B.1, B.2, B.3, B.4, B.5, B.6, B.7 and B.8 demonstrate this effect, which were simulated with Case 1² in which only the mass of the web is varied.

The initial conditions used to numerically integrate the equations are given in Table C.1.

The mass of the web reaches a limit of around 40 kg , after which, the web is no longer able to keep its shape in this configuration.

Runs E01–E04 show the space-web can be stabilised while the robots move across the surface, the mass of the web increasing to a critical value of approximately 25% of the total system mass. The maximum CoM displacement is 0.85 m for these four runs. In runs E05–E06, the mass of the web is increased to 44.82 kg and 48.25 kg respectively. This causes significant instability in the web for the 48.25 kg web, showing that for certain configurations of the space-web system, the mass of the web is a critical parameter. The marginal increase in web mass gives a noticeable degradation in the behaviour of the space-web past that critical point.

6.7.2 Robot mass

The momentum of the robot was thought to be a significant parameter in the stability of the space-web, therefore the robot mass was investigated as a possible parameter. Runs 18-21 tested values of M_{robot} ³ from 1 kg to 100 kg and the CoM positions are shown in Figures B.9, B.10, B.11, B.12, B.13 and B.14.

The initial conditions used to numerically integrate the equations are given in Table C.4.

Counter-intuitively, increasing the mass of the robot caused the space-web to be-

²With symmetrical robot paths.

³From 3% to 17% of the system mass.

come more stable! This is due to the centripetal effect of more mass on the outside of the web causing the sub-spans to become more rigid and effectively act as a damper to the system.

There is a sharp divide between the stable behaviour of the robot masses set at 16 kg shown in Figure B.12, and the unstable behaviour with the masses at 15 kg shown in Figure B.11. This critical dividing line between the acceptable and unacceptable system movement is clear as it is unexpected, and raises significant issues for the construction of the space-web, especially with a lighter robot.

6.7.3 Web asymmetry

The single biggest driver of instability on the space-web system was found to be the asymmetry in the web configuration and mass distribution.

Very small asymmetries in the initial conditions of the space-web (compared to a perfectly symmetrical equilateral triangle) are amplified in certain configurations of the space-web, and may create large instabilities in the system, especially for energetic configurations such as high web mass and/or large angular velocities. A small difference in orientation (on the order of 1°) of the sub-spans may lead to large asymmetries between the sub-spans in a relatively short time ($\approx 100s$).

The cases chosen to investigate the effect of asymmetry on the web are as follows:

- Case 1: Robots 1,2,3 walk along the edges of the web from sub-span to next sub-span – (symmetrical)
- Case 2: Robots 2,3 walk along the edges of the web while Robot 1 is stationary on sub-span 1 – (unsym.)
- Case 3: Robot 3 walks along the edges of the web while Robots 1,2 are stationary on sub-spans 1,2 – (unsym.)
- Case 4: Robots 1,2,3 walk along from the centre to their sub-spans – (sym.)

- Case 5: Robot 1 spirals outwards from the centre to the edges, Robots 2,3 are fixed on sub-spans – (unsym.)
- Case 6: Robot 1 walks along from the centre to sub-span1, Robots 2,3 remain in centre –(unsym.)

The initial conditions used to numerically integrate the equations are given in Table C.2.

Cases 1 and 4 are symmetrical, shown in Figures B.15 and B.18. Case 1 has a stable CoM position throughout the simulation, with a maximum CoM travel of only 0.46 m. Case 4 is symmetrical, however has a maximum CoM travel of 10.96 m and is on the limits of what is defined as acceptable movement for the CoM. In contrast, Cases 2, 3, 5 and 6 are asymmetrical, shown in Figures B.16, B.17, B.19, and B.20. The asymmetric cases show a large CoM movement of between 18 m and 38 m, and are unstable.

Compounding the problem of uneven mass, the initial conditions of the three sub-spans were found to influence the stability of the system. The equations could not be solved with $\psi = \{0^\circ, 120^\circ, 240^\circ\}$ or spacing the web sub-spans by exactly 120° , for reasons not known at this time. Initial conditions for ψ were implemented as a triplet; the three sub-span values of $\{0 + \psi, 120^\circ, 240^\circ - \psi\}$ offer a solution to this problem.

More generally, it is expected that for most configurations of the triangular space-web, holding the three sub-spans permanently rigid at exactly 120° separation will be impossible as small perturbations to the web in the space environment will be constantly experienced.

Adding the effect of many asymmetrical robot masses exacerbates the problem of uneven mass distribution. To remedy this, the space-web must be configured to occupy as low an energy state as the mission will allow: low web mass; light, slow moving robots; low angular velocity of the web. In this state, the asymmetry of the

web still exists, but it is kept to a manageable level.

6.7.4 Robot crawl velocity

The faster the robots travelled along the web, the greater the likelihood of unstable behaviour of the web, as the CoM displacement plots show in Figures B.21 and B.25. Both are simulated with Case 1 – symmetrical robot paths.

The initial conditions used to numerically integrate the equations are given in Table C.3.

When robot crawl velocity was increased from 0.1 m/s to 10 m/s , by lowering the time fixed from 1000 s to 10 s , the maximum CoM displacement increased marginally – from 0.3 m to 1.5 m .

These two cases of mass dependant stability and velocity dependant stability are clearly energy related. The higher the energy contained in the system, the more likely the system is to exhibit unstable behaviour. This boundary has not yet been clearly defined. Generally speaking, however, the slower the robot movement across the web, the more likely the web is to remain stable given a perfectly symmetrical web. Given the levels of CoM displacement, the robot velocity is not a significant destabilising factor in this scenario.

6.8 Statistical investigation into stability

A series of solutions to the space-web equations of motion were examined to examine the effect of five parameters on the space-web stability. The mass of the web, M_{web} , the mass of the three daughter satellites, M_{sat} , the robot mass, M_{robot} , the sub-span angular coordinate, ψ and the average sub-span angular velocity $\frac{\partial\psi}{\partial t}$ were thought to have an effect on the maximum movement of the Centre of Mass (CoM) of the space-web system. Therefore, the solutions to 36 different sets of ini-

tial conditions were found, with $2^5 = 32$ runs complemented by 4 centre point runs. The 36 runs were performed in *Mathematica*, and the results of the maximum CoM displacement were entered into a statistical package, *Design Expert* 7.03. *Design Expert* then performs an analysis of variance (ANOVA) calculation on the factorial data provided. ANOVA is a collection of statistical models and their associated procedures which compare means by splitting the overall observed variance into different parts. A 5 degree of freedom model (or less, if requested) is then extrapolated from the data and analysed for statistical significance.

The five most strongly correlated model parameters were:

$$M_{\text{web}} - \quad M_{\text{sat}} + \quad M_{\text{web}} * \frac{\partial \psi}{\partial t} + \quad M_{\text{sat}} * M_{\text{robot}} * \frac{\partial \psi}{\partial t} - \quad M_{\text{robot}} -$$

$\psi +$ and $\frac{\partial \psi}{\partial t} -$ were statistically relevant in the model, but to a lesser degree than the other parameters. As they have a stronger effect when combined with other variables, the (un)stabilising influence they have may be overtaken by these other factors.

Parameters are shown with a (+) indicating a stabilising effect or a (-) indicating a destabilising effect, with the full table of values located in Appendix C.

As $M_{\text{web}} -$ has the strongest influence over the model, it would be most beneficial to the stability to reduce the mass of the web.

The reverse is true of the daughter satellite mass, $M_{\text{sat}} +$, increasing this parameter will tend to stabilise the system.

For combinations of main parameters such as $M_{\text{web}} * \frac{\partial \psi}{\partial t} +$, it would be most beneficial to increase the product to stabilise the system. In this case, the angular momentum of the web will tend to rigidize the system and enhance the stability.

6.8.1 Masses of the web and satellite

The influence the masses of the web and the daughter satellites have on the CoM position are shown in the contour graph, Figure 6.14. The contours are shaded from

blue (stable) through green and yellow to red (unstable) and follow the maximum CoM displacement from the central facility.

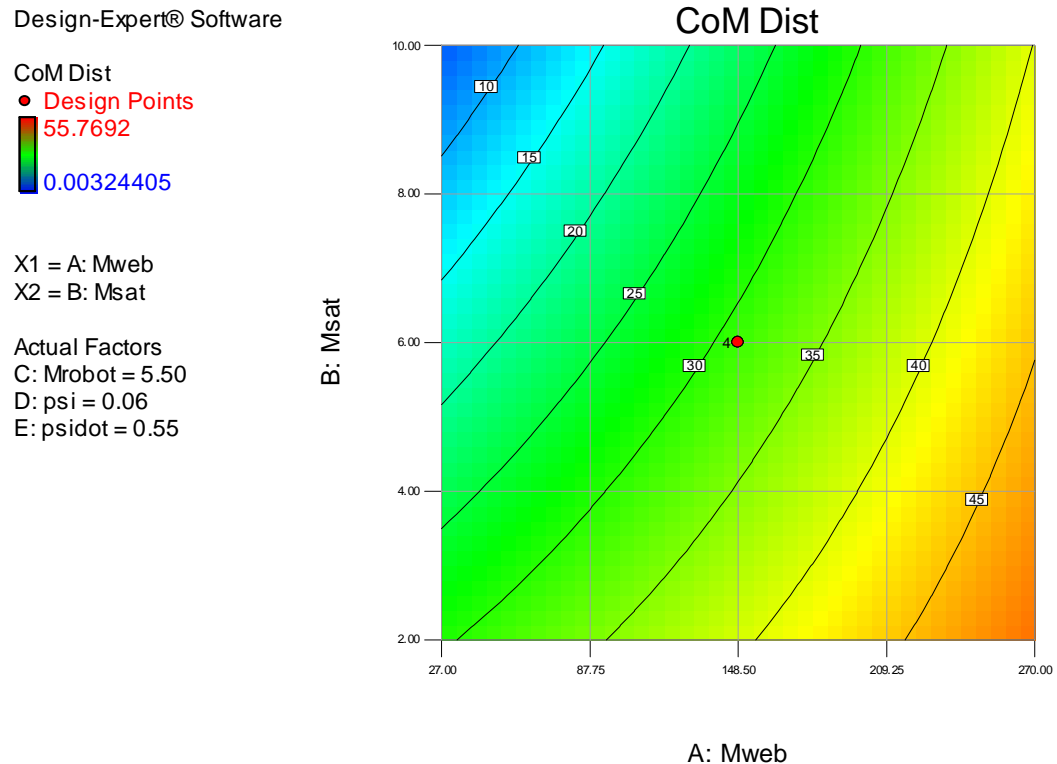


Figure 6.14: Contours of CoM movement while varying web and satellite mass

For the small sample space of initial conditions, the most stable point would be a high satellite mass ($> 8\text{ kg}$) and low web mass ($< 50\text{ kg}$). A CoM displacement of above 10 m is unstable, and would be very difficult for a robot to manoeuvre over the surface.

In general terms, this clearly shows the stabilising effect of the mass of the satellites and the destabilising effect of the mass of the web.

6.8.2 Masses of the web and robot

The influence the masses of the web and the robot have on the CoM position are shown in the contour graph, Figure 6.15. The contours are shaded from blue (stable)

through green and yellow to red (unstable) and follow the maximum CoM displacement from the central facility.

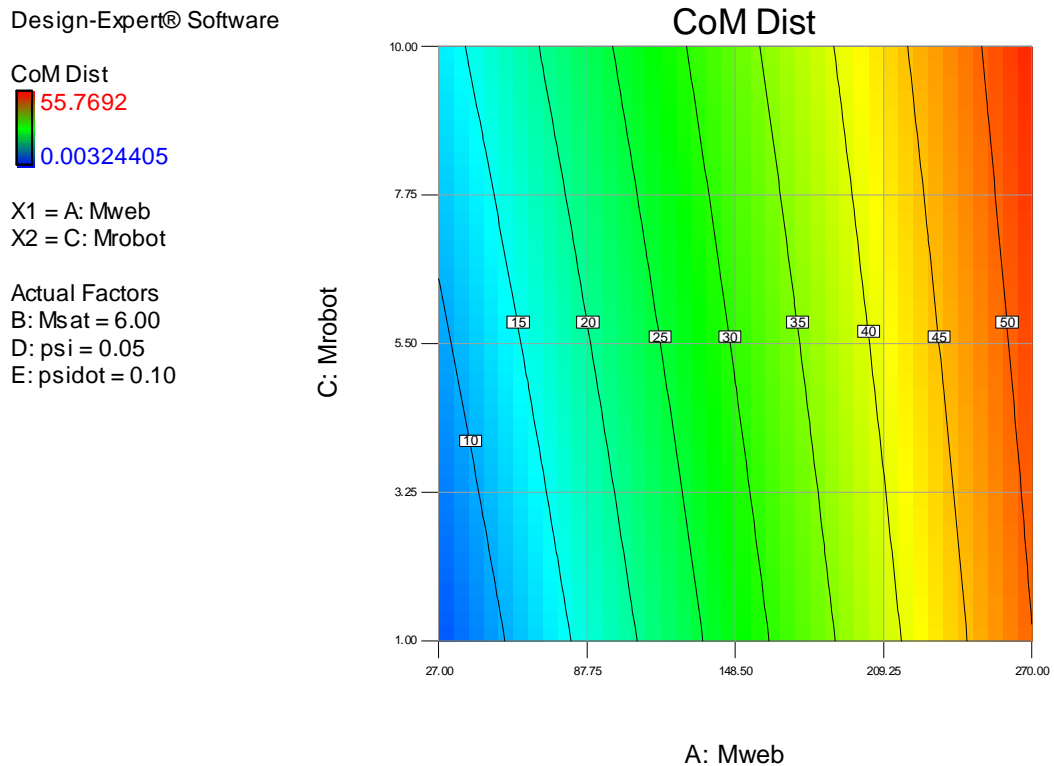


Figure 6.15: Contours of CoM movement while varying web and robot mass

The relative strengths of the robot and web masses are shown, with the mass of the web exerting a much stronger influence over the behaviour of the web. The stability boundary is shown in the bottom left hand corner of the graph. A stability margin of 5 m is preferable, here the web mass must be kept below 50 kg and the mass of the robot, although less influential, would be best suited at below 5 kg. This shows that if a low $\frac{\partial\psi}{\partial t}$ is required, the web can be made more stable with careful consideration of variables.

6.8.3 Mass of the web and angular velocity

The influence the masses of the web and the angular velocity, $\frac{\partial\psi}{\partial t}$, have on the CoM position are shown in the contour graph, Figure 6.16. The contours are shaded from

blue (stable) through green and yellow to red (unstable) and follow the maximum CoM displacement from the central facility.

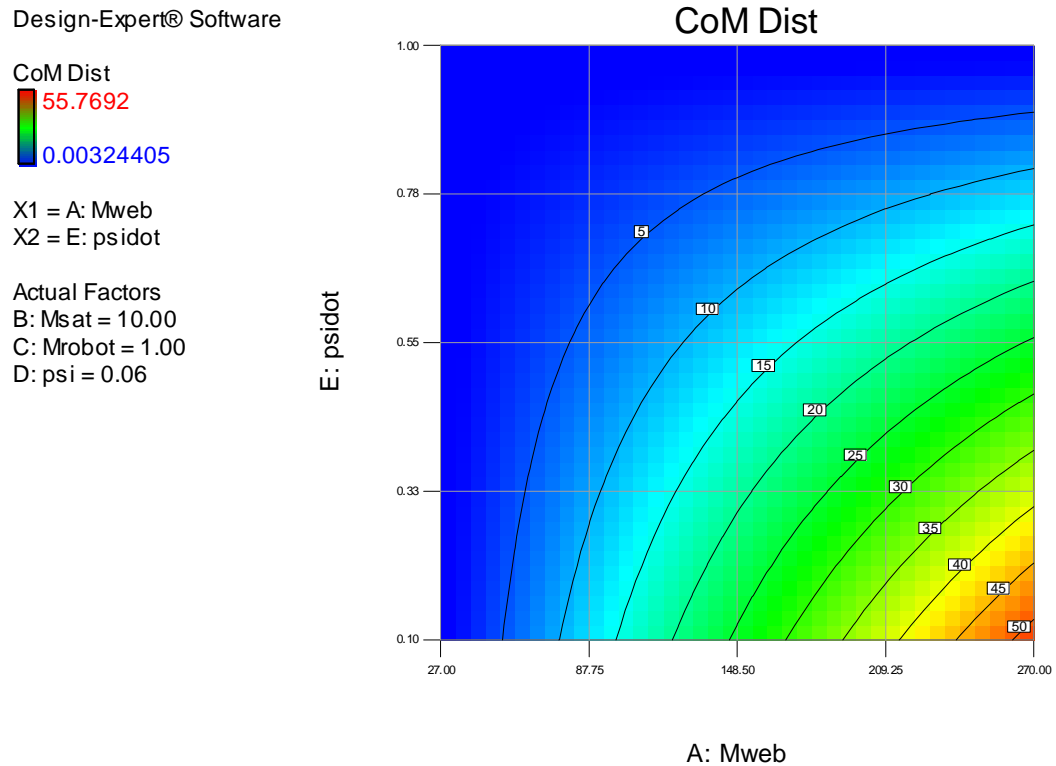


Figure 6.16: Contours of CoM movement while varying web mass and $\frac{\partial\psi}{\partial t}$

In a high-stability scenario, the options to configure the space-web are plentiful. Carefully choosing the previous parameters that lead to a high probability of stability, namely a high satellite mass (10 kg) and a low robot mass (1 kg), affords a larger range of possible values for the mass of the web and the angular velocity of the web.

If the largest acceptable CoM movement is limited to 5 m , then there are three choices available, depending on the primary requirement of the space-web system. If a low web mass is required, then a low $\frac{\partial\psi}{\partial t}$ must match, and vice versa. Alternatively, if a high mass is required, a high $\frac{\partial\psi}{\partial t}$ must be specified, and vice versa. The final option is for a low web mass and a high $\frac{\partial\psi}{\partial t}$, affording a large safety margin that may be advantageous in, for example, a pilot study mission.

6.8.4 Mass of the robot and angular velocity

The influence the mass of the robot and the angular velocity, $\frac{\partial\psi}{\partial t}$, have on the CoM position are shown in the contour graph, Figure 6.17. The contours are shaded from blue (stable) through green and yellow to red (unstable) and follow the maximum CoM displacement from the central facility.

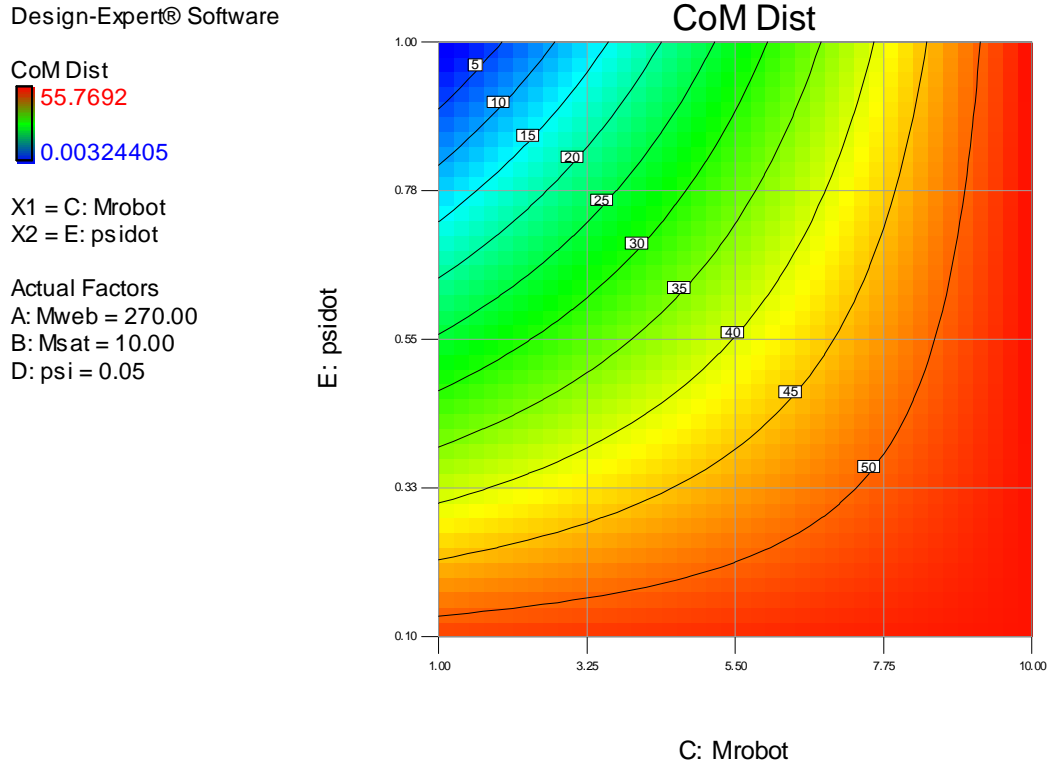


Figure 6.17: Contours of CoM movement while varying robot mass and $\frac{\partial\psi}{\partial t}$

The final comparison is for a high mass specification – a 270 kg web mass and 10 kg satellite mass. This combines the two strongest influences on the system, the former destabilising and the later stabilising. For a stable system, it is essential to ensure the robot mass is small and the angular rotation rate is large.

6.9 Conclusions and recommendations

6.9.1 Conclusions

The achievement of a stable, re-configurable web orbiting in space with robots moving along its surface is a realistic goal. There must, however, be limits to the behaviour of the robots and the configuration of the web. Both the robots and the web must be as light as possible and the robots must be as slow moving as the mission allows, given that this limits the destabilising effects of these parameters. The daughter satellites must be as heavy as possible, and the angular rotation rate must be as large as possible to maximise these stabilising effects. In all cases, the web configuration must be as symmetrical as practicable.

6.9.2 Recommendations

To capitalise on the knowledge gained in this research, there are a few areas that may be expanded on for potential future exploration.

Constructing the web while on orbit would mitigate the deployment phase of the mission, eliminating one of the major failure modes of the system. Using the robots to weave the web could be inspired by spiders on Earth, for example, just as the space web has been inspired by the Furoshiki cloth.

Using the knowledge gained through moving masses over the web, there are many applications that would benefit from simulating web-based constructions with moving masses. Solar-sails and antennae could be assembled or reconfigured by robots moving across their surface.

Chapter 7

Conclusions

7.1 Tether rotations

- Rotations using a different system of equations are equally able to describe the same system.
- Therefore, the choice of rotational system can be tailored in such a way to suit the analysis.

7.2 Tethers with inclination

- A demonstration mission launching a micro-satellite from MEO to Lunar orbit is achievable using current technology. The safety margins, however, are extremely small and the MMET launcher would be located in an orbit with large amounts of debris.
- The inclination term does not significantly alter the dynamics of the MMET system. However, any out-of-plane component in the local axes – whether on

an inclined orbit or not – interacts with the orbital parameters to create an unsteady oscillation in the tether. This is unacceptable for payload aiming and release, therefore the local out-of-plane angle should be minimised insofar as possible.

7.3 Deployment and recovery of tethers

- Deploying and recovering the tethers on the MMET system is not a trivial matter; however, they can be achieved in a well controlled and structured way.
- A method for deployment and recovery in the orbital plane have been outlined, giving confidence that the MMET is capable and suitable for use as a reusable launch platform.

7.4 Space-webs

- The achievement of a stable, re-configurable web orbiting in space with robots moving along its surface is a realistic goal.
- There are limits to the behaviour and configuration of the robots and web: the robots must be light and as slow moving, the web must be as light, the daughter satellites must be heavy and the angular rotation rate must be as large as possible to maximise these stabilising effects. In all cases, the web configuration must be as symmetrical as practicable.

7.5 Further study

It is my belief that tethers, and in particular the MMET, have a significant role to play in mankind's future in space. By addressing the following issues uncovered in this thesis, the case for using the MMET will be strengthened.

The stator arm will require to be modelled and analysed if the concept of the MMET is ever to be successful. The possibility of interference between the tether and stator arms will logically follow on from this analysis.

Likewise, the concept of a space-web is both novel and interesting, and doubtless will be studied further. It is essential to perform further ground tests or even zero-gravity studies of the MMET and space-webs to provide validation of the equations of motion.

Bibliography

- J.A. Andión and C. Pascual. Useful experiences in a series of deployable booms for CLUSTER satellites. In R. A. Harris, editor, *ESA SP-480: 9th European Space Mechanisms and Tribology Symposium*, pages 113–120, September 2001. URL <http://adsabs.harvard.edu/abs/2001smt..conf..113A>.
- Yuri Artsutanov. V kosmos na electrovoze (to the cosmos by electric train). Newspaper report, Komsomolskaya Pravda, July 31 1960. URL http://www.robotstore.com/download/Artsutanov_Pravda_SE.pdf. Translated by Joan Barth Urban, Roger G. Gilbertson and M. Molloy.
- E.A. Belbruno. Lunar capture orbits, a method of constructing Earth Moon trajectories and the Lunar GAS mission. *DGLR, and JSASS, International Electric Propulsion Conference, 19th, Colorado Springs, CO, USA*, AIAA-1987(1054):1–10, 1987.
- Vladimir V. Beletsky and Evgenii M. Levin. *Dynamics of Space Tether Systems (Advances in the Astronautical Sciences)*. American Astronautical Society, 1993. URL <http://eleanor.lib.gla.ac.uk/record=b2210829>.
- Matthew Bennett, Michael F. Schatz, Heidi Rockwood, and Kurt Wiesenfeld. Huygens’s clocks. *Proceedings of the Royal Society of London. Series A: Mathematical, Physical and Engineering Sciences*, 458(2019):563–579, 2002. doi: 10.1098/rspa.2001.0888.

R. Biesbroek and G. Janin. ESA bulletin 103 - "Ways to the Moon?", August 2000.

URL <http://www.esa.int/esapub/bulletin/bullet103/biesbroek103.pdf>.

A. S. Brown. Spreading spectrum of reinforcing fibers,. *Aerospace America*, 27(1):16, January 1989.

Joseph A. Carroll. Tether applications in space transportation. *Acta Astronautica*, 13(4):165–174, April 1986. doi: 10.1016/0094-5765(86)90061-5.

M.P. Cartmell and D.J. McKenzie. A review of space tether research. *Progress in Aerospace Sciences*, 44(1):1–21, January 2008. doi: 10.1016/j.paerosci.2007.08.002.

M.P. Cartmell, S.W. Ziegler, R. Khanin, and D.I.M. Forehand. Multiple scales analyses of the dynamics of weakly nonlinear mechanical systems. *Transactions of ASME, Applied Mechanics Reviews*, 56(5):455–492, 2003. doi: 10.1115/1.1581884.

M.P. Cartmell, S.W. Ziegler, and D.S. Neill. On the performance prediction and scale modelling of a Motorised Momentum Exchange Propulsion Tether. In M. S. El-Genk, editor, *AIP Conf. Proc. 654: Space Technology and Applications International Forum - STAIF 2003*, pages 571–579, January 2003. STAIF-2003-571.

M.P. Cartmell, C.R. McInnes, and D.J. McKenzie. Proposals for a continuous Earth-Moon cargo exchange mission using the Motorised Momentum Exchange Tether concept. *Proc. XXXII International Summer School and Conference on Advanced Problems in Mechanics, APM2004*, pages 72–81, June 24 - July 1 2004.

M.P. Cartmell, D.I.M. Forehand, M.C. D'Arrigo, D.J. McKenzie, Y. Wang, and A.V. Metrikine. Approximate analytical solution for a motorised momentum exchange tether on a circular earth orbit. In *Proceedings of the XXXIVth Summer School on Advanced Problems in Mechanics*, pages 119–130. Russian Academy of Sciences, Repino, St.Petersburg, Russia, 2006.

Arthur C. Clarke. *The Fountains of Paradise*. Victor Gollancz, 1979. ISBN 0-575-02520-4.

M.L. Cosmo and E.C. Lorenzini. *Tethers in Space Handbook (3rd ed)*. Number 3. NASA Marshall Space Flight Center, Cambridge, MA, December 1997. URL <http://www.tethers.com/papers/TethersInSpace.pdf>.

A.N. Danilin, T.V. Grishanina, F.N. Shklyarchuk, and D.V. Buzlaev. Dynamics of a space vehicle with elastic deploying tether. *Computers & Structures*, 72(1-3): 141 – 147, 1999. ISSN 0045-7949. doi: 10.1016/S0045-7949(99)00039-5.

Saswato R. Das. Final thoughts from Sir Arthur C. Clarke. Online, March 2008. URL <http://spectrum.ieee.org/mar08/6075>.

A.B. DeCou. Tether static shape for rotating multimass, multitether, spacecraft for ‘triangle’ Michelson interferometer. *Journal of Guidance, Control, and Dynamics*, 12(2):273–275, 1989. URL <http://www.aiaa.org/content.cfm?pageid=406&gID=20401>.

M. Eiden and M.P. Cartmell. Overcoming the challenges: Tether systems roadmap for space transportation applications. *AIAA/ICAS International Air and Space Symposium and Exposition, Ohio, USA*, 14-17 July 2003.

R.L. Forward. Tether transport from LEO to the Lunar surface. In *Proceedings of the 27th AIAA/ASME/SAE/ASEE Joint Propulsion Conference and Exhibit*. AIAA., 1991. URL <http://www.tethers.com/papers/LEO2Lunar'92.pdf>. 91-2322.

R.L. Forward and R.P. Hoyt. Space tethers. *Scientific American*, February 1999.

R.L. Forward and R.P. Hoyt. Failsafe multiline Hoytether lifetimes. *1st AIAA/-SAE/ASME/ASEE Joint Propulsion Conference, San Diego, CA, AIAA Paper 95-28903*, July 1995.

P.E. Glaser. Power from the sun, its future. *Science*, 162(3856):857–861, 1968. doi: 10.1126/science.162.3856.857.

G. Gómez, A. Jorba, J. Masdemont, and C. Simó. Study of the transfer from the Earth to a halo orbit around the equilibrium point L1. *Celestial Mechanics and Dynamical Astronomy*, 56(4):541–562, August 1993. doi: 10.1007/BF00696185.

Gianluca Gorni. Mathematica plots with directional arrows - the curvesgraphs6 package, 9th August 2008. URL <http://users.dimi.uniud.it/~gianluca.gorni/Mma/Mma.html>.

M.A. Green, K. Emery, D.L. King, S. Igari, and W. Warta. Solar cell efficiency tables (version 22). *Progress in Photovoltaics: Research and Applications*, 11: 347–352, 2003.

M.D. Griffin and J.R. French. *Space Vehicles Design and Construction*. AIAA Education Series, 1991.

A.C. Hindmarsh. ODEPACK, a systematized collection of ODE solvers. In R. S. Stepleman et al., editor, *Scientific Computing (vol. 1 of IMACS Transactions on Scientific Computation)*, volume 1, pages 55–64, North-Holland, Amsterdam, 1983.

Walter Hohmann. *Die Erreichbarkeit der Himmelskörper - Untersuchungen über das Raumfahrtproblem*. Oldenbourg, R., München und Berlin, 1925. ISBN 3-486-23106-5.

Walter Hohmann. *The Attainability Of Heavenly Bodies*. NASA (CASI), November 1960. URL <http://ntrs.nasa.gov/details.jsp?R=191962>. Report NASA-TT-F-44, Translated from original German.

R.P. Hoyt. Stabilization of electrodynamic space tethers. In M.S. El-Genk, editor, *AIP Conf. Proc. 608: Space Technology and Applications International Forum*

- *STAIF 2002*, pages 570–578, January 2002. URL http://www.tethers.com/papers/ED_Stabilization.pdf.

John D. Isaacs, Allyn C. Vine, Hugh Bradner, and George E. Bachus. Satellite elongation into a true “sky-hook”. *Science*, 151(3711):151, Feb 1966. doi: 10.1126/science.151.3711.682.

Solar System Dynamics Group JPL. JPL’s HORIZONS system. Website, August 2008. URL <http://ssd.jpl.nasa.gov/horizons.cgi>.

Osman M. Kamel and Adel S. Soliman. Sensitivity of transfer orbits to small errors in position and velocity at cut-off. *Acta Astronautica*, 58(5):5, March 2006. doi: 10.1016/j.actaastro.2005.09.006.

N. Kaya, M. Iwashita, S. Nakasuka, L. Summerer, and J. Mankins. Crawling robots on large web in rocket experiment on Furoshiki deployment. In *55th International Astronautical Congress 2004 - Vancouver, Canada*, 2004a. URL http://www.esa.int/gsp/ACT/doc/POW/ACT-RPR-NRG-2004-IAC-SPS-Crawling_robots.pdf.

N. Kaya, S. Nakasuka, L. Summerer, and J. Mankins. International rocket experiment on a huge phased array antenna constructed by furoshiki satellite with robots. In *24th International Symposium on Space Technology and Science, Miyazaki, Japan*, 2004b.

Jerry B. Keiper. Mathematica developer conference, Boston, MA, USA, June 1992. URL <http://library.wolfram.com/infocenter/Conferences/4687/>.

Wang Sang Koon, Martin W. Lo, Jerrold E. Marsden, and Shane D. Ross. Dynamical systems, the three-body problem and space mission design. In B. Fiedler, K. Groger, and J. Sprekels, editors, *International Conference on Differential Equations, Berlin, 1999*, pages 1167–1181, Berlin, 1999. World Scientific.

W.S. Koon, M.W. Lo, J.E. Marsden, and S.D. Ross. Low energy transfer to the

- Moon. *Celestial Mechanics and Dynamical Astronomy*, 81(1-2):63–73, 2001. URL www.gutenberg.org/cache/epub/11/pg11.html.
- M. Kraus. LiveGraphics 3D webpage, 2007. URL <http://wwwvis.informatik.uni-stuttgart.de/~kraus/LiveGraphics3D/index.html>.
- G.A. Kyroudis and B.A. Conway. Advantages of tether release of satellites from elliptic orbits. *Journal of Guidance, Control, and Dynamics*, 11(5):441–448, 1988.
- Simone Lennert and Matthew P. Cartmell. Analysis and design of a friction brake for momentum exchange propulsion tethers. *Acta Astronautica*, 59(8-11):923 – 930, 2006. ISSN 0094-5765. doi: 10.1016/j.actaastro.2005.07.042. Selected Proceedings of the Fifth IAA International Conference on Low Cost Planetary Missions.
- Martin W. Lo and Shane D. Ross. The Lunar L1 gateway: Portal to the stars and beyond. In *AIAA Space 2001 Conference*, Albuquerque, New Mexico, August 28-30 2001.
- E.C. Lorenzini. Error-tolerant technique for catching a spacecraft with a spinning tether. *Journal of Vibration and Control*, 10(10):1473 – 1491, 2004. ISSN 1077-5463. doi: 10.1177/1077546304042062.
- E.C. Lorenzini, M.L. Cosmo, M. Kaiser, M.E. Bingham, D.J. Vonderwell, and L. Johnson. Mission analysis of spinning systems for transfers from low orbits to geostationary. *Journal of Spacecraft and Rockets*, 37(2):165–172, 2000. URL <http://www.aiaa.org/content.cfm?pageid=406&gID=3562>.
- C.R. McInnes and M. Cartmell. *Dynamics of propellantless propulsion systems*. Elsevier, 2006. URL <http://eprints.cdlr.strath.ac.uk/6507/>. ISBN 0-12-373562-9.
- D. McKenzie, M. Cartmell, G. Radice, and M. Vasile. Space webs final report 05-4109a. Ariadna study 05-4109a, University of Glasgow and ESA

ACT, 2006. URL <http://www.esa.int/gsp/ACT/doc/ARI/ARIStudyReport/ACT-RPT-MAD-ARI-05-4109b-SpaceWebs-Glasgow.pdf>.

D.J. McKenzie and M.P. Cartmell. On the performance of a motorized tether using a ballistic launch method. *55th International Astronautical Congress, Vancouver, Canada*, (IAC-04-IAA-3.8.2.10), Oct. 4-8 2004.

W.I. McLaughlin. Walter Hohmann's roads in space. *Space Mission Architecture*, 2000. URL http://www.lpl.arizona.edu/undergrad/classes/fall2007/Hubbard_195a-10/Hohmann_bio.pdf.

J.K. Miller and E.A. Belbruno. A method for the construction of a Lunar transfer trajectory using ballistic capture. *Spaceflight Mechanics: Advances in the Astronautical Sciences, AAS 91-100*, 75(1):97–109, 1991.

A.K. Misra and V.J. Modi. Three-dimensional dynamics and control of tether-connected n-body systems. *Acta Astronautica*, 26(2):77 – 84, 1992. ISSN 0094-5765. doi: 10.1016/0094-5765(92)90048-N.

Y. Miyazaki and Y. Iwai. Dynamics model of solar sail membrane. In *ISAS 14th Workshop on Astrodynamics and Flight Mechanics*, 2004. URL http://www.hayabusa.isas.jaxa.jp/kawalab/astro/2004contents_e.html.

V.J. Modi and A.K. Misra. On the deployment dynamics of tether connected two-body systems. *Acta Astronautica*, 6(9):1183–1197, September 1979. doi: 10.1016/0094-5765(79)90064-X.

V.J. Modi, Geng Chang-Fu, A.K. Misra, and Da Ming Xu. On the control of the space shuttle based tethered systems. *Acta Astronautica*, 9(6-7):437–443, 1982. doi: 10.1016/0094-5765(82)90074-1.

V.J. Modi, P.K. Lakshmanan, and A.K. Misra. On the control of tethered satellite systems. *Acta Astronautica*, 26(6):411–423, June 1992. doi: 10.1016/0094-5765(92)90070-Y.

V.J. Modi, S. Bachmann, and A.K. Misra. Dynamics and control of a space station based tethered elevator system. *Acta Astronautica*, 29(6):429–449, June 1993. doi: 10.1016/0094-5765(93)90036-V.

H. Moravec. A nonsynchronous orbital skyhook. *The Journal of the Astronautical Sciences*, 25(4):307–322, 1977. URL <http://www.frc.ri.cmu.edu/~hpm/project.archive/1976.skyhook/papers/scasci.txt>.

T. Nakano, O. Mori, and J. Kawaguchi. Stability of spinning solar sail-craft containing a huge membrane. *AIAA Guidance, Navigation, and Control Conference and Exhibit*, 2005. AIAA-2005-6182.

S. Nakasuka, T. Aoki, I. Ikeda, Y. Tsuda, and Y. Kawakatsu. “furoshiki satellite” – a large membrane structure as a novel space system. *Acta Astronautica*, 48: 461–468, March 2001. doi: 10.1016/S0094-5765(01)00056-X.

A.H. Nayfeh and D.T. Mook. *Nonlinear Oscillations*. John Wiley and Sons, New York, 1979.

T. S. No and J. E. Cochran Jr. Dynamics and control of a tethered flight vehicle. *Journal of Guidance, Control, and Dynamics*, 18(1):66–72, 1995. URL <http://www.aiaa.org/content.cfm?pageid=318&volume=18&issue=1&pubid=23&paperid=56658>.

Zoe Parsons. Lunar perturbations of a supersynchronous GEO transfer orbit in the early orbit phase. Master’s thesis, Cranfield University, 2006. URL http://dspace.lib.cranfield.ac.uk:8080/bitstream/1826/1767/1/ZParsons_ThesisMSc.pdf.

M. Pascal, A. Djebli, and L. El Bakkali. Laws of deployment/retrieval in tether connected satellites systems. *Acta Astronautica*, 45(2):61–73, July 1999. doi: 10.1016/S0094-5765(99)00115-0.

M. Pascal, A. Djebli, and L. El Bakkali. A new deployment/retrieval scheme for a tethered satellite system, intermediate between the conventional scheme and the crawler scheme. *Journal of Applied Mathematics and Mechanics*, 65(4):689–696, 2001. doi: 10.1016/S0021-8928(01)00073-9.

Jerome Pearson. The orbital tower: A spacecraft launcher using the Earth's rotational energy. *Acta Astronautica*, 2(9-10):785 – 799, 1975. ISSN 0094-5765. doi: 10.1016/0094-5765(75)90021-1.

Linda Petzold. Automatic selection of methods for solving stiff and nonstiff systems of ordinary differential equations. *SIAM Journal on Scientific and Statistical Computing*, 4(1):136–148, 1983. doi: 10.1137/0904010.

Ary Pizarro-Chong and Arun K. Misra. Dynamics of multi-tethered satellite formations containing a parent body. *Acta Astronautica*, 63(11-12):1188 – 1202, 2008. ISSN 0094-5765. doi: 10.1016/j.actaastro.2008.06.021.

Dominic V. Rosato. *Rosato's Plastics Encyclopedia and Dictionary*. Hanser Publishers, Munich, January 1993.

Shane David Ross. *Cylindrical manifolds and tube dynamics in the restricted three-body problem*. Ph.D. thesis, California Institute of Technology, 7th April 2004. URL <http://etd.caltech.edu/etd/available/etd-05182004-154045/>.

K. Sorensen. Conceptual design and analysis of an MXER tether boost station. In *37th AIAA/ASME/SAE/ASEE Joint Propulsion Conference and Exhibit*, 2001. URL www.tethers.com/papers/AIAA_2001-3915_MXER.pdf.

K. Sorensen. Hyperbolic injection issues for MXER tethers. In *39th AIAA/ASME/-SAE/ASEE Joint Propulsion Conference*, 2003. URL http://www.tethers.com/papers/AIAA_2003-5221.pdf.

T.H. Sweetster. An estimate of the global minimum ΔV needed for the Earth-Moon transfer. In *Spaceflight mechanics 1991; Proceedings of the 1st AAS/AIAA Annual*

Spaceflight Mechanics Meeting, Houston, TX, Feb. 11-13, 1991. Pt. 1 (A93-17901 05-13), p. 111-120., pages 111–120, 1991. URL <http://adsabs.harvard.edu/abs/1991sfm..proc..111S>. AAS/AIAA Paper No. 91-101.

Victor G. Szebehely and Hans Mark. *Adventures in Celestial Mechanics*. Wiley VCH, 2nd edition edition, 2 1998. ISBN 9780471133179. URL <http://amazon.co.uk/o/ASIN/0471133175/>.

G. Tibert and M. Gärdsback. Space-webs. Technical report, KTH and ESA ACT, 2006. URL <http://www.esa.int/gsp/ACT/doc/ARI/ARIStudyReport/ACT-RPT-MAD-ARI-05-4109a-SpaceWebs-KTH.pdf>.

K.E. Tsiolkovski. Grezi o zemle i nene (day-dreams of Heaven and Earth). In *U.S.S.R. Academy of Sciences edition*, page 35, 1959. URL http://www.daviddarling.info/encyclopedia/S/space_elevator.html.

University of Glasgow Press Release. Students in a spin after ESA commission space-web. Online, 07 Apr 2009. URL http://www.gla.ac.uk/news/headline_115222_en.html.

J. Valverde and G.H.M. van der Heijden. Magnetically-induced buckling of a whirling conducting rod with applications to electrodynamic space tethers, 2008. URL <http://www.citebase.org/abstract?id=oai:arXiv.org:0810.3668>.

G.H.M. van der Heijden. Mode-locking in nonlinear rotordynamics. *Journal of Nonlinear Science*, 5(3):257–283, May 1995. doi: 10.1007/BF01212957.

Robert C. Weast. *CRC Handbook of Chemistry and Physics*. CRC Press, 66th edition, June 1985. ISBN 0849304652, page E-43.

Wikipedia. Space debris — Wikipedia, the free encyclopedia, September 2008. URL http://en.wikipedia.org/w/index.php?title=Space_debris&oldid=239761439. [Online; accessed 28-September-2008].

Paul Williams, Chris Blanksby, and Pavel Trivailo. Tethered planetary capture: Controlled maneuvers. *Acta Astronautica*, 53(4-10):681–708, 2003. doi: 10.1016/S0094-5765(03)80029-2.

Paul Williams, Chris Blanksby, Pavel Trivailo, and Hironori A. Fujii. In-plane payload capture using tethers. *Acta Astronautica*, In Press, Corrected Proof:–, 2005. doi: 10.1016/j.actaastro.2005.03.069. AA-57-772.

Wolfram. Mathematica NDSolve FAQ, 01 May 2007. URL <http://support.wolfram.com/mathematica/mathematics/numerics/ndsolveresources.en.html>. Accessed on 20th June 2007.

Brian Wong and Arun Misra. Planar dynamics of variable length multi-tethered spacecraft near collinear Lagrangian points. *Acta Astronautica*, 63(11-12):1178 – 1187, 2008. ISSN 0094-5765. doi: 10.1016/j.actaastro.2008.06.022.

Xu Xu, M. Wiercigroch, and M.P. Cartmell. Rotating orbits of a parametrically-excited pendulum. *Chaos, Solitons & Fractals*, 23(5):1537 – 1548, 2005. ISSN 0960-0779. doi: 10.1016/j.chaos.2004.06.053.

S.W. Ziegler. *The Rigid Body Dynamics of Tethers in Space*. Ph.D. thesis, Department of Mechanical Engineering, University of Glasgow, 2003.

S.W. Ziegler and M.P. Cartmell. Using motorized tethers for payload orbital transfer. *Journal of Spacecraft and Rockets*, 38(6):904–913, 2001.

Glossary

Notation Description

LEO	Low Earth Orbit
MEO	Medium Earth Orbit
MMET	Motorized Momentum Exchange Tether
MXER	Momentum eXchange/Electrodynamic Reboost
WSB	Weak Stability Boundary

Appendix A

Equations of motion with inclination

184

The equations of motion the MMET (stator arm not included) for the generalised co-ordinates $R, \theta, \iota, \psi, \alpha$ are:

R equation:

$$\frac{\mu M_{\text{total}}}{R^2} + \ddot{R}M_{\text{total}} - R \left(\cos^2(\iota)\dot{\theta}^2 + \dot{\iota}^2 \right) M_{\text{total}} = 0 \quad (\text{A.1})$$

θ equation:

$$R \cos(\iota) \left(2 \cos(\iota) \dot{R} \dot{\theta} + R \left(\cos(\iota) \ddot{\theta} - 2 \dot{\theta} \dot{\iota} \sin(\iota) \right) \right) M_{\text{Facility}} = 0 \quad (\text{A.2})$$

ι equation:

$$R^2 \cos(\iota) \sin(\iota) M_{\text{Facility}} \dot{\theta}^2 + R \left(2\dot{R}\dot{i} + R\ddot{i} \right) M_{\text{Facility}} = 0 \quad (\text{A.3})$$

ψ equation:

$$\begin{aligned} & \frac{1}{8} \left(2 \cos^2(\alpha) \sin(2\psi) i^2 + \left(4\dot{\alpha} \sin(\psi) - 2 \left(\cos(\psi) \dot{\psi} \sin(2\alpha) + \dot{\theta} \left(2 \cos(2\psi) \sin(\iota) \cos^2(\alpha) + \cos(\iota) \cos(\psi) \sin(2\alpha) \right) \right) i - \right. \right. \\ & \left. \left. \dot{\theta} \left(4 \cos(\psi) \dot{\alpha} \sin(\iota) + 2\dot{\psi} \sin(2\alpha) \sin(\psi) \sin(\iota) + \dot{\theta} \left(2 \cos^2(\alpha) \sin(2\psi) \sin^2(\iota) + \sin(2\alpha) \sin(2\iota) \sin(\psi) \right) \right) \right) \right. \\ & \left. (4M_{\text{payload}} + M_{\text{tether}}) L^2 + \frac{1}{192} \left(128\ddot{\psi} (3M_{\text{payload}} + M_{\text{tether}}) + \right. \right. \\ & \left. \left. 48 \left(2 \cos(\iota) \ddot{\theta} \cos^2(\alpha) + 2\ddot{\psi} \cos^2(\alpha) - \cos(\psi) \ddot{\theta} \sin(2\alpha) \sin(\iota) - 2\dot{\alpha} \left(\dot{\psi} \sin(2\alpha) + \dot{\theta} (\cos(\iota) \sin(2\alpha) + \cos(2\alpha) \cos(\psi) \sin(\iota)) \right) + \right. \right. \\ & \left. \left. i \sin(2\alpha) \sin(\psi) + \dot{\theta} \dot{\psi} \sin(2\alpha) \sin(\iota) \sin(\psi) + i \left(\cos(\psi) \dot{\psi} \sin(2\alpha) - \dot{\theta} \left(2 \sin(\iota) \cos^2(\alpha) + \cos(\iota) \cos(\psi) \sin(2\alpha) \right) + 2 \cos(2\alpha) \dot{\alpha} \sin(\psi) \right) \right) \right. \\ & \left. (4M_{\text{payload}} + M_{\text{tether}}) L^2 + R\mu \cos(\alpha) \sin(\psi) \left(\left(\frac{1}{(L^2 - 2R \cos(\alpha) \cos(\psi) L + R^2)^{3/2}} - \frac{1}{(L^2 + 2R \cos(\alpha) \cos(\psi) L + R^2)^{3/2}} \right) M_{\text{payload}} + \right. \right. \\ & \left. \left. 4 \left(\frac{1}{(L^2 - 4R \cos(\alpha) \cos(\psi) L + 4R^2)^{3/2}} - \frac{1}{(L^2 + 4R \cos(\alpha) \cos(\psi) L + 4R^2)^{3/2}} \right) M_{\text{tether}} \right) L \right. \\ & \left. = \cos \alpha \text{ Force}_{\text{payload}} L (1 - \text{Eclipse}) \quad (\text{A.4}) \right. \end{aligned}$$

α equation:

$$\begin{aligned}
& \frac{1}{32} \left(((6 \cos(2\iota) + \cos(2(\iota - \psi)) - 2 \cos(2\psi) + \cos(2(\iota + \psi)) + 2) \sin(2\alpha) + 8 \cos(2\alpha) \cos(\psi) \sin(2\iota)) \dot{\theta}^2 + \right. \\
& \quad 16 \dot{\psi} (\cos(\iota) \sin(2\alpha) + \cos(2\alpha) \cos(\psi) \sin(\iota)) \dot{\theta} - 8i^2 \sin(2\alpha) \sin^2(\psi) + 8\dot{\psi}^2 \sin(2\alpha) - \\
& \quad \left. 8i \left(2 \cos(2\alpha) \dot{\psi} \sin(\psi) + \dot{\theta} (2 \cos(2\alpha) \cos(\iota) \sin(\psi) - \sin(2\alpha) \sin(\iota) \sin(2\psi)) \right) \right) (4M_{\text{payload}} + M_{\text{tether}}) L^2 + \\
& \frac{1}{192} \left(128 \ddot{\alpha} (3M_{\text{payload}} + M_{\text{tether}}) + 96 \left(\ddot{\alpha} + \cos(\psi) \ddot{i} + \cos(\psi) \dot{\theta} \dot{\psi} \sin(\iota) + i \left(\cos(\iota) \dot{\theta} - \dot{\psi} \right) \sin(\psi) + \ddot{\theta} \sin(\iota) \sin(\psi) \right) (4M_{\text{payload}} + M_{\text{tether}}) \right) L^2 + \\
& R\mu \cos(\psi) \sin(\alpha) \left(\left(\frac{1}{(L^2 - 2R \cos(\alpha) \cos(\psi) L + R^2)^{3/2}} - \frac{1}{(L^2 + 2R \cos(\alpha) \cos(\psi) L + R^2)^{3/2}} \right) M_{\text{payload}} + \right. \\
& \quad \left. 4 \left(\frac{1}{(L^2 - 4R \cos(\alpha) \cos(\psi) L + 4R^2)^{3/2}} - \frac{1}{(L^2 + 4R \cos(\alpha) \cos(\psi) L + 4R^2)^{3/2}} \right) M_{\text{tether}} \right) L \\
& = -\text{Force}_{\text{payload}} L (1 - \text{Eclipse}) \quad (\text{A.5})
\end{aligned}$$

186

The equations use the following substitutions:

$$M_{\text{total}} = M_{\text{Facility}} + 2M_{\text{payload}} + 2M_{\text{tether}} \quad (\text{A.6})$$

and **Eclipse** is the binary function:

$$\text{Eclipse} = \begin{cases} 1 & \left\{ \begin{array}{l} R^2(1 - \cos^2(\iota) \cos^2(\theta)) \leq R_{\text{Earth}}^2 \left(1 + \frac{R \cos(\theta)}{R_{\text{Sun}}}\right)^2 \\ \text{AND} \\ \cos(\iota) \cos(\theta) > 0 \end{array} \right. \\ 0 & \text{otherwise} \end{cases} \quad (\text{A.7})$$

Note: the inclination generalised coordinate is ι the ninth letter of the Greek alphabet (iota). The first derivative is $\frac{\partial \iota}{\partial t} = i$ and the second derivative is $\frac{\partial^2 \iota}{\partial t^2} = \ddot{i}$.

Appendix B

Space-webs – additional graphics

B.1 Case 1 – CoM plots of stability while increasing web mass

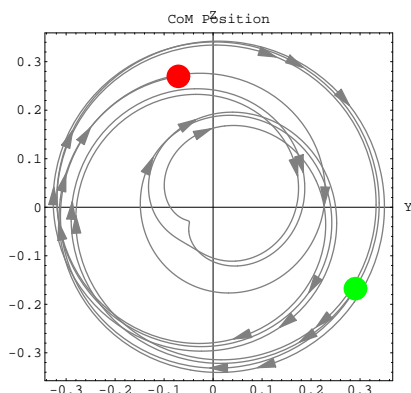


Figure B.1: $mWeb = 27\text{ kg}$

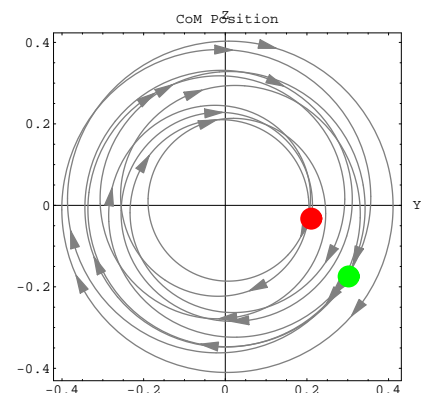


Figure B.2: $mWeb = 33.75\text{ kg}$

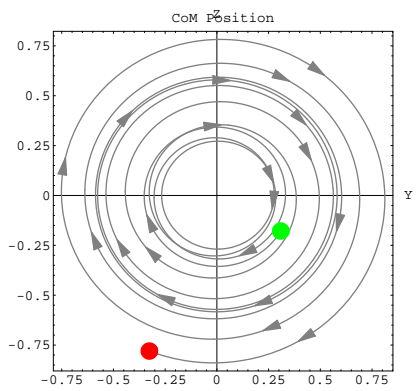


Figure B.3: $mWeb = 37.8 \text{ kg}$

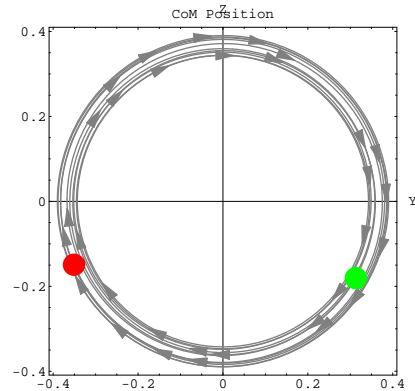


Figure B.4: $mWeb = 40.5 \text{ kg}$

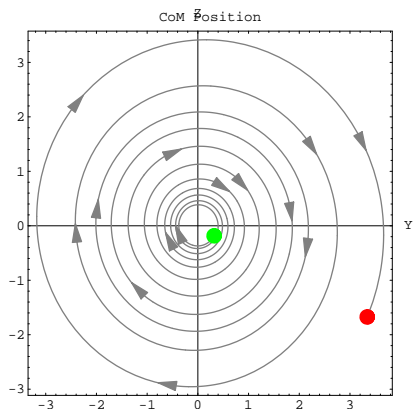


Figure B.5: $mWeb = 44.82 \text{ kg}$

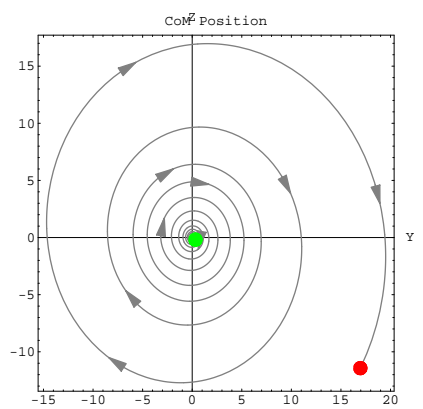


Figure B.6: $mWeb = 47.25 \text{ kg}$

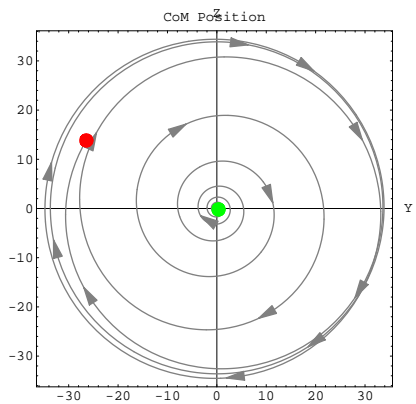


Figure B.7: $mWeb = 54 \text{ kg}$

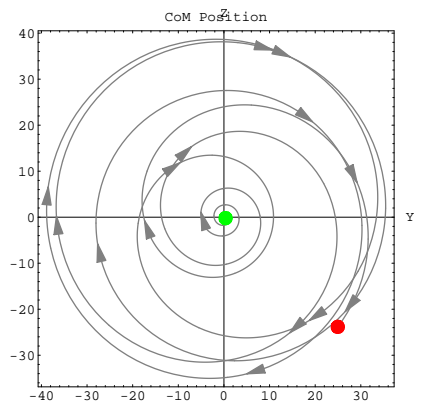


Figure B.8: $mWeb = 67.5 \text{ kg}$

B.2 Case 1 – CoM plots of stability while increasing robot mass

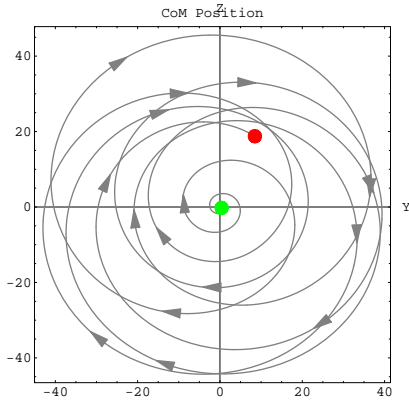


Figure B.9: $M_{robot} = 1 \text{ kg}$

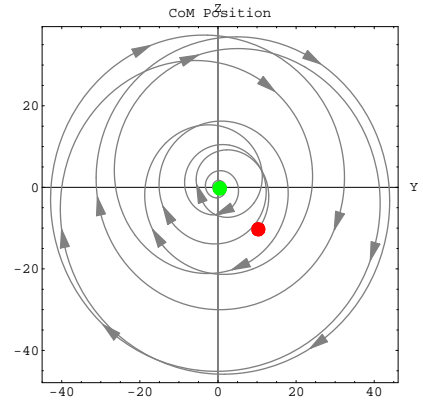


Figure B.10: $M_{robot} = 10 \text{ kg}$

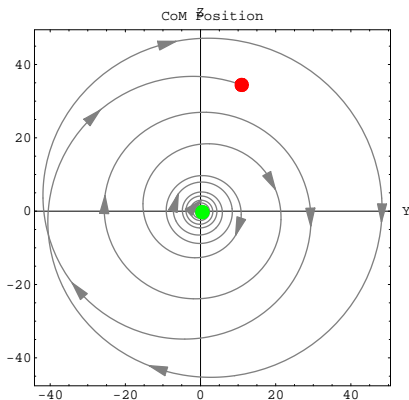


Figure B.11: $M_{robot} = 15 \text{ kg}$

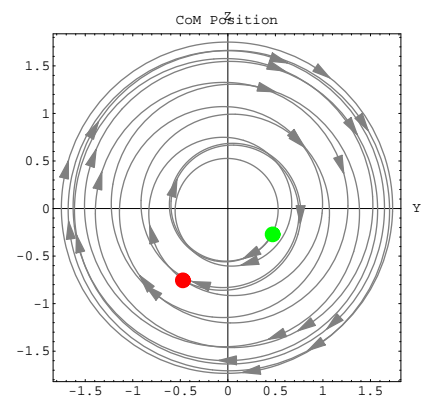


Figure B.12: $M_{robot} = 16 \text{ kg}$

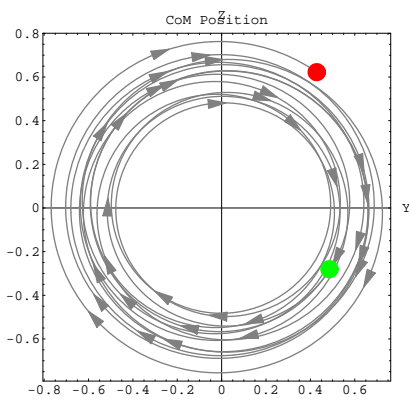


Figure B.13: $M_{robot} = 20 \text{ kg}$

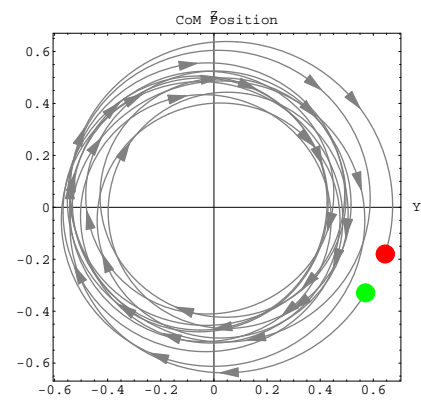


Figure B.14: $M_{robot} = 100 \text{ kg}$

B.3 CoM plots of stability while changing robot paths

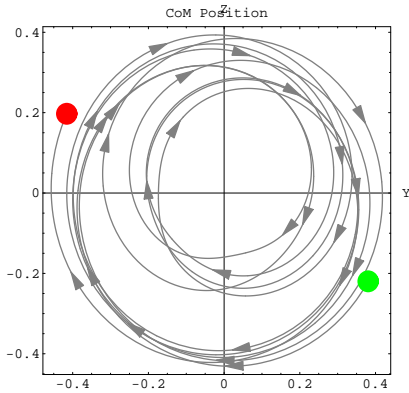


Figure B.15: Case 1

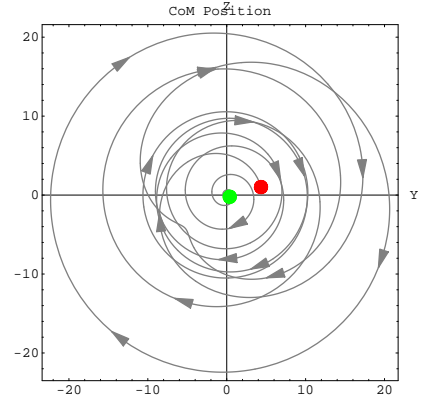


Figure B.16: Case 2

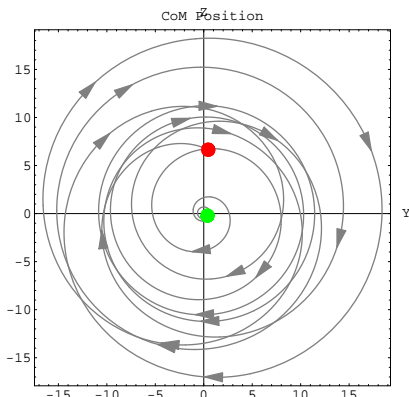


Figure B.17: Case 3

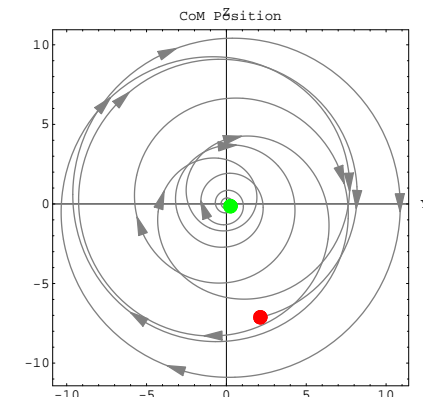


Figure B.18: Case 4

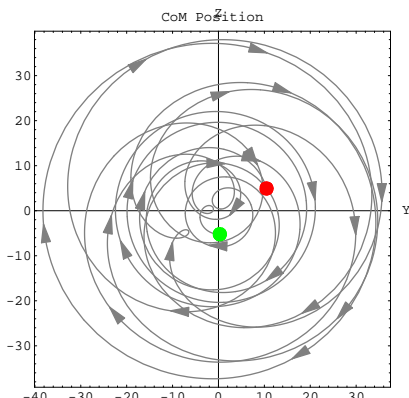


Figure B.19: Case 5

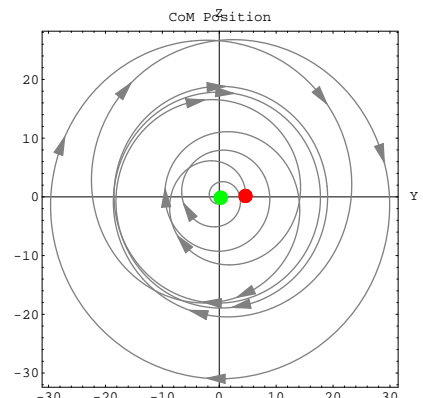


Figure B.20: Case 6

B.4 Case 1 – CoM plots of stability while decreasing robot velocity

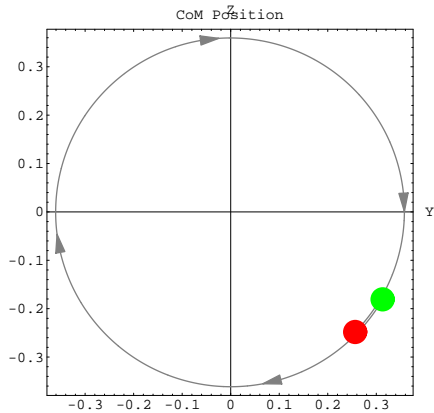


Figure B.21: $V_{robot} = 10.0 \text{ m/s}$

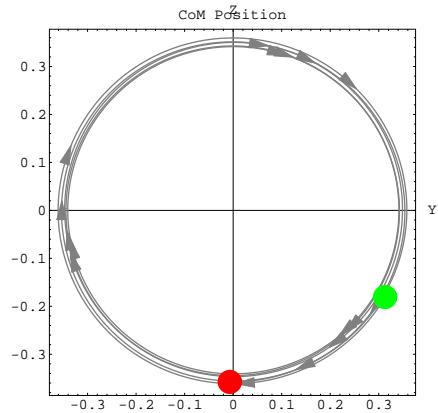


Figure B.22: $V_{robot} = 2.0 \text{ m/s}$

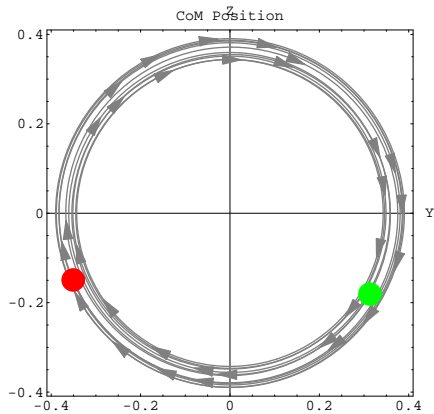


Figure B.23: $V_{robot} = 1.0 \text{ m/s}$

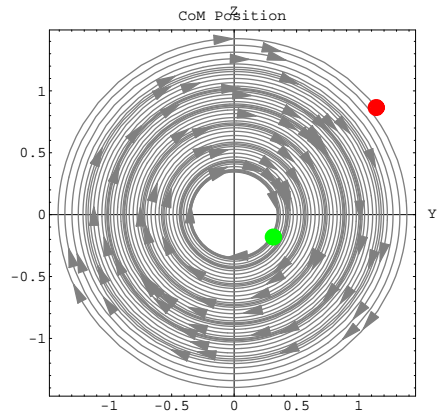


Figure B.24: $V_{robot} = 0.2 \text{ m/s}$

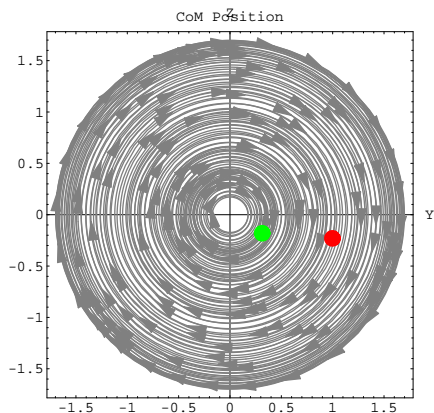


Figure B.25: $V_{robot} = 0.1 \text{ m/s}$

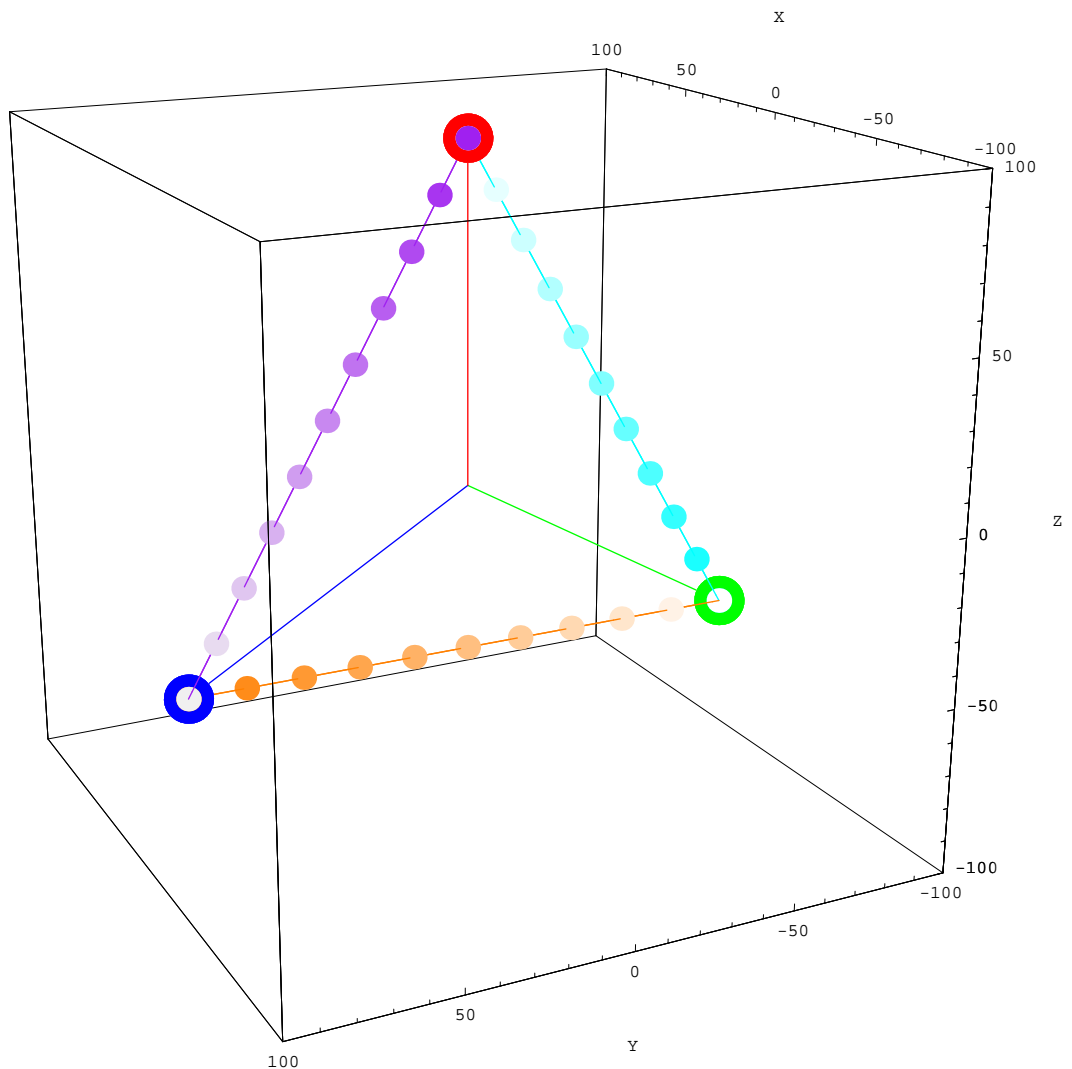


Figure B.26: Case 1 – 3 robots moving symmetrically round the web perimeter

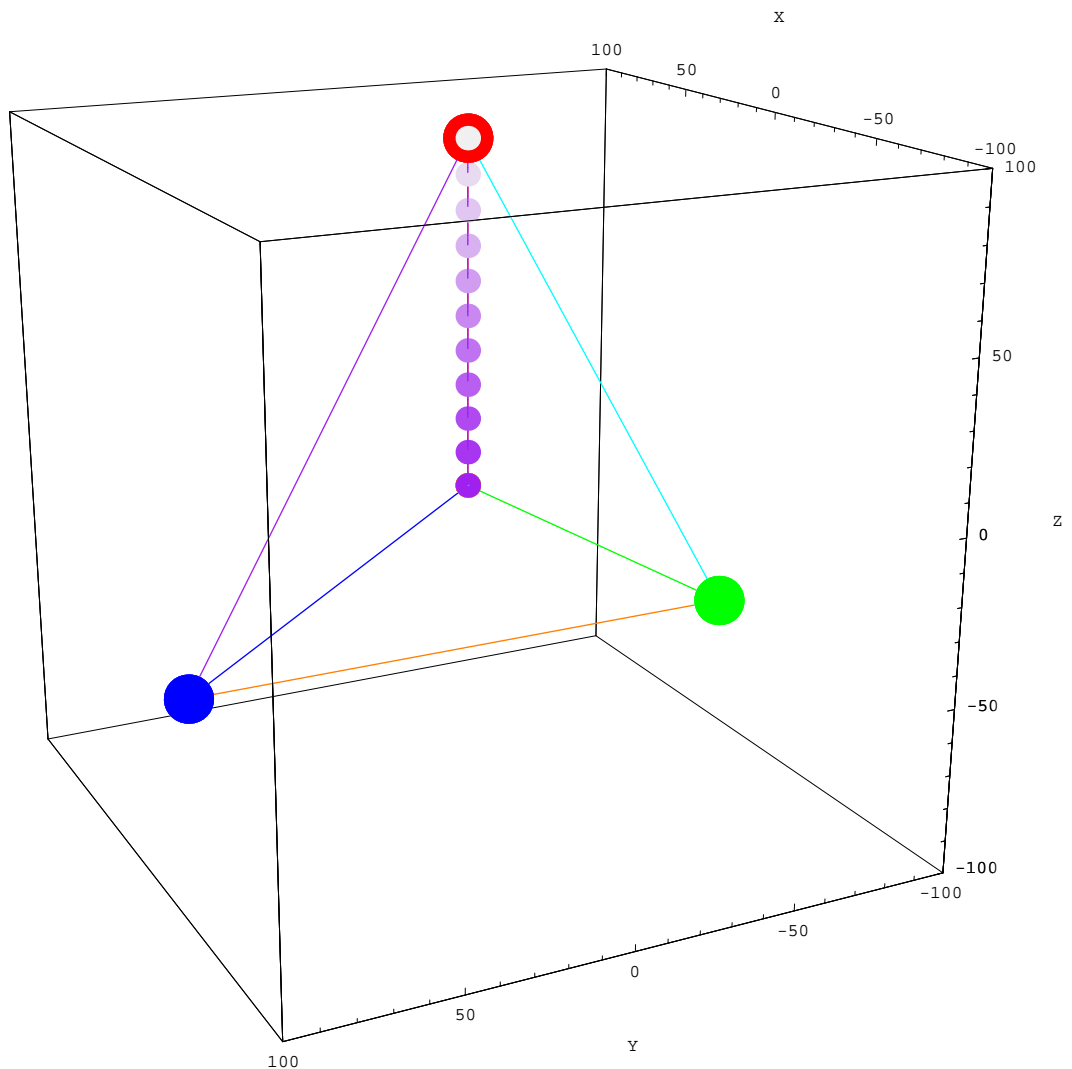


Figure B.27: Case 6 – 1 robot moving asymmetrically along first sub-span

Appendix C

Space-webs – additional data

Data generated during the first run phase – initially examining the dynamics of the space-web.

The units for the variables are as follows:

Mweb	Msat	MRobot	psi	psidot	k	CoM disp
kg	kg	kg	degrees	radians/s	N/m	m

The initial conditions of all other parameters are:

$$L = 100.0 \text{ m} ; M_{\text{facility}} = 100.0 \text{ kg} ; \text{eccent} = 0.0 ;$$

$$t_{\text{end}} = 100.0 \text{ s} ; R = 6.578 * 10^6 \text{ m} ; K = 122.69$$

K is the spring stiffness, given in Equation 6.15. This is derived from the Young's Modulus, $E = 3 * 10^{10}$ and the CSA of each strand of $4 * 10^{-6}$.

The webs are configured with 3 web sections (i.e. 2 divisions).

The angular displacements are given with one angle only: ψ . This may be converted to give the angles of the three sub-spans such that: $\{0 + \psi, 120^\circ, 240^\circ - \psi\}$.

The three angular rates are equal, and are quoted once in the following tables..

Data generated during the statistical investigation into stability (see Section 6.8).

run	A:Mweb.	B:Msat	C:Mrobot	D:psi	E:psidot	Max CoM
E01	27.	10	2	1	0.1	0.35
E02	33.75	10	2	1	0.1	0.41
E03	37.8	10	2	1	0.1	0.85
E04	40.5	10	2	1	0.1	0.39
E05	44.82	10	2	1	0.1	3.74
E06	47.25	10	2	1	0.1	20.44
E07	54.	10	2	1	0.1	34.82
E08	67.5	10	2	1	0.1	39.40
E09	135.	10	2	1	0.1	46.49
E10	270.	10	2	1	0.1	51.03

Table C.1: Influence of web mass on maximum CoM

run	symmetrical	A:Mweb	B:Msat	C:Mrobot	D:psi	E:psidot	Max CoM
Case 1	yes	40.5	10	10	1	0.1	0.46
Case 2	no	40.5	10	10	1	0.1	22.61
Case 3	no	40.5	10	10	1	0.1	18.52
Case 4	yes	40.5	10	10	1	0.1	10.95
Case 5	no	40.5	10	10	1	0.1	38.24
Case 6	no	40.5	10	10	1	0.1	30.99

Table C.2: Influence of symmetrical robot movement on maximum CoM

run	A:Mweb	B:Msat	C:Mrobot	D:psi	E:psidot	time	Robot speed	Max CoM
FG1	40.5	10	2	1	0.1	10	10.0	0.36
FG2	40.5	10	2	1	0.1	50	2.0	0.36
FG3	40.5	10	2	1	0.1	100	1.0	0.40
FG4	40.5	10	2	1	0.1	500	0.2	1.40
FG5	40.5	10	2	1	0.1	1000	0.1	1.70

Table C.3: Influence of simulation time (effectively robot speed across web) on maximum CoM

run	A:Mweb	B:Msat	C:Mrobot	D:psi	E:psidot	Max	CoM
Frobot01	135	10	0.1	1	0.1	45.09	
Frobot02	135	10	1	1	0.1	45.89	
Frobot03	135	10	5	1	0.1	46.66	
Frobot04	135	10	10	1	0.1	46.08	
Frobot05	135	10	12	1	0.1	50.53	
Frobot06	135	10	15	1	0.1	48.44	
Frobot07	135	10	16	1	0.1	1.75	
Frobot08	135	10	17	1	0.1	1.08	
Frobot09	135	10	18	1	0.1	0.86	
Frobot10	135	10	19	1	0.1	0.82	
Frobot11	135	10	20	1	0.1	0.77	
Frobot12	135	10	21	1	0.1	0.66	
Frobot13	135	10	50	1	0.1	0.67	
Frobot14	135	10	100	1	0.1	0.75	

Table C.4: Influence of robot mass on maximum CoM

run	A:Mweb	B:Msat	C:Mrobot	D:psi	E:psidot	F: CoM posn	predicted	Diff %
1	27	2	1	0.01	0.1	11.49	12.29	107%
2	270	2	1	0.01	0.1	49.41	46.71	95%
3	27	10	1	0.01	0.1	0.00	-2.70	-83118%
4	270	10	1	0.01	0.1	52.76	53.56	102%
5	27	2	10	0.01	0.1	28.09	25.39	90%
6	270	2	10	0.01	0.1	53.20	54.00	102%
7	27	10	10	0.01	0.1	0.00	0.80	19141%
8	270	10	10	0.01	0.1	55.75	53.05	95%
9	27	2	1	0.1	0.1	11.28	10.16	90%
10	270	2	1	0.1	0.1	49.83	47.37	95%
11	27	10	1	0.1	0.1	0.03	0.12	369%
12	270	10	1	0.1	0.1	52.79	51.67	98%
13	27	2	10	0.1	0.1	27.49	26.72	97%
14	270	2	10	0.1	0.1	52.99	51.65	97%
15	27	10	10	0.1	0.1	0.04	-0.05	-111%
16	270	10	10	0.1	0.1	55.61	54.83	99%
17	148.5	6	5.5	0.055	0.55	47.15	31.10	66%
18	148.5	6	5.5	0.055	0.55	47.15	31.10	66%
19	148.5	6	5.5	0.055	0.55	47.15	31.10	66%
20	148.5	6	5.5	0.055	0.55	47.15	31.10	66%
21	27	2	1	0.01	1	49.41	46.71	95%
22	270	2	1	0.01	1	49.86	50.66	102%
23	27	10	1	0.01	1	0.00	0.80	24649%
24	270	10	1	0.01	1	0.00	-2.70	-64127%
25	27	2	10	0.01	1	33.10	33.90	102%
26	270	2	10	0.01	1	49.41	46.71	95%
27	27	10	10	0.01	1	49.83	47.13	95%
28	270	10	10	0.01	1	55.77	56.57	101%
29	27	2	1	0.1	1	49.41	48.63	98%
30	270	2	1	0.1	1	49.82	48.69	98%
31	27	10	1	0.1	1	0.03	-1.09	-3346%
32	270	10	1	0.1	1	0.03	-0.74	-2287%
33	27	2	10	0.1	1	33.11	31.98	97%
34	270	2	10	0.1	1	49.41	48.63	98%
35	27	10	10	0.1	1	0.00	-0.77	-18329%
36	270	10	10	0.1	1	55.76	54.63	98%

Table C.5: Statistical investigation into stability

Term	Effect	Stdized Effect	SumSqr	% Contribtn
A-Mweb	-	27.21	7182.9	37.72
B-Msat	+	-16.57	2447.8	12.85
AE	+	-15.32	1869.6	9.82
BCE	-	14.34	1656.8	8.70
C-Mrobot	-	10.90	872.3	4.58
BC	-	9.93	666.4	3.50
BE	+	-8.69	686.3	3.60
AB	-	7.21	435.0	2.28
ACE	-	6.98	346.3	1.82
CE	-	5.04	232.9	1.22
AC	-	4.66	193.2	1.01
ABE	+	-3.76	118.3	0.62
ABC	-	3.75	118.6	0.62
BDE	+	-3.37	93.4	0.49
ADE	-	3.29	117.6	0.62
ABCDE	-	3.19	85.1	0.45
ACD	-	3.17	99.5	0.52
BCD	+	-3.15	102.7	0.54
CDE	+	-3.12	92.4	0.49
ABDE	-	3.12	81.5	0.43
CD	+	-3.09	110.1	0.58
D-psi	+	-3.08	79.6	0.42
BCDE	+	-3.08	83.7	0.44
ACDE	-	3.04	89.0	0.47
ABCD	-	3.02	61.5	0.32
DE	+	-3.00	75.6	0.40
ABD	-	2.97	74.0	0.39
AD	-	2.93	98.7	0.52
BD	+	-2.84	34.2	0.18
E-psidot	-	1.48	18.3	0.10
Lack of fit			9.6	0.05
Pure error			0.0	0.00

Table C.6: Results of the statistical investigation into stability

The ‘Effect’ term in column 2 is a reflection on the stabilising (+) or destabilising (-) effect of the term.

Appendix D

Material strengths

The information in Table D.1 is provided courtesy of the Island One Society at <http://www.islandone.org/LEOBiblio/SPBI1MA.HTM>, and is compiled from data from the following sources: [Brown, 1989, pp 14-18], [Rosato, 1993, p 638], [Weast, 1985, p E-43].

¹aramid fiber

²gel-spun polyethylene

³gel-spun polyethylene

⁴plastic fiber, Zylon is brand name of PBO

⁵theoretical data

Material	Property				
	tensile strength (P) [GPa]	Young's modulus (Y) [GPa]	density (ρ) [kg/m ³]	characteristic velocity $\sqrt{2P/\rho}$ [m/s]	speed of sound in thin rods $\sqrt{Y/\rho}$ [m/s]
steel	1-5	200	7900	503-1125	5032
aluminum alloys	0.1-0.7	72	2700	272-720	5270
titanium alloys	0.6-1.3	110	5000	490-721	4690
beryllium fiber	3.3	310	1870	1879	12870
boron fiber	3.5	400	2450	1690	12778
fused silica	73	-	-	2200	5760
pyrex glass	62	-	-	2320	5170
E-glass fiber	2.4	72.4	2540	1375	5339
S-glass fiber	4.5	85.5	2490	1901	5860
Kevlar 49 ¹	3.6	130	1440	2236	9502
Spectra 1000 fiber ²	3.0	170	970	2487	13239
Spectra 2000 fiber ³	3.51	-	970	2690	-
PBO (Zylon) ⁴	5.8	280-365	1560-1580	2710-2727	13397-15199
carbon fiber	1-6.5	250-830	1850	1040-2651	11600-21200
buckytube cable ⁵	150	630	1300	15191	22014

Table D.1: Properties of selected materials

Appendix E

Motor properties

Specification	
List Price:	\$910
Horsepower	4 hp
RPM	4150
mass	23 kg
Armature Volts	48 V
Torque	6.86 Nm
Full Load Current	72.0 A

Table E.1: Properties of GE Motor 5BC49JB1115

The information in Table E.1 is provided courtesy of the GE industrial products guide at:

www.geindustrial.com/cwc/marketing/Motors/catalog/CrossReference.pdf

and is compiled from data from the following additional source:

www.emotorstore.com/productdetail.asp?Q_brandID_E_1_A_catID_E_23_A_subCatID_E_354_A_productID_E_583_A_skuID_E_30698

The motor is a GE Industrial Motor, Product Number D379, Model Number 5BC49JB1115. This is a DC motor, used to power electric vehicles (commonly golf-carts). The specifications are used in Section 4.5.1 to gain an approximate mass, torque and rotational speed for an equivalent space-based motor. The torque is quoted as 81.0 oz-ft , and converted to Nm .